

(The original cover page is with Erin Reiche, ERL. This is the version for our group distribution.)

Analysis of Stoichiometry-Related Defects in Group III - Nitrides

Eicke R. Weber, UC Berkeley, CA94720

BEST AVAILABLE COPY

Final Report 2001 - 2003

AFOSR grant No.: F49620-01-1-0151

20041119 016

Table of Contents

Abstract	03
1. Introduction	04
2. Low temperature growth of GaAs and defect determination	05
2.1 In-situ Defect Determination: DRS	05
2.2 Overview: Reproducible LT-GaAs growth	08
2.3 Ultrahigh-doped epilayers and their native defects	10
2.4 Nitrogen Incorporation in LT-GaAs: Native Defects	12
3. C-Doped GaN Epilayers and their Native Defects	15
4. A new hydrogenic donor in electron-irradiated GaN	18
5. Low Frequency Noise Measurements for Defect Characterization	19
5.1 Noise measurement system: Setup, signal calibration and analysis	19
5.2 First results in III-V compounds	21
5.3 GOI-based devices	22
5.4 C-doped GaN	24
5.5 AlGaN / GaN HEMTs	24
6. Summary and Future work	27
7. Personnel	27
8. References	28
9. Publications	33
10. Figures	35
11. Attachment :	
Local band transitions in group III – nitrides: VEELS	69

REPORT DOCUMENTATION PAGE

AFRL-SR-AR-TR-04-

0575

Public reporting burden for this collection of information is estimated to average 1 hour per response, including gathering and maintaining the data needed, and completing and reviewing the collection of information. Send collection of information, including suggestions for reducing this burden, to Washington Headquarters Service, Davis Highway, Suite 1204, Arlington, VA 22202-4302, and to the Office of Management and Budget, Paper

1. AGENCY USE ONLY (Leave blank)		2. REPORT DATE	3. REPORT NUMBER
			01 Jan 2001 - 31 Dec 2003 FINAL
4. TITLE AND SUBTITLE Analysis of Stoichiometry-Related Defects in Group III - Nitrides			5. FUNDING NUMBERS 61102F 2305/BX
6. AUTHOR(S) Professor Weber			
7. PERFORMING ORGANIZATION NAME(S) AND ADDRESS(ES) UNIVERSITY OF CALIFORNIA BERKELEY 336 SPROUL HALL BERKELEY CA 94720			8. PERFORMING ORGANIZATION REPORT NUMBER
9. SPONSORING/MONITORING AGENCY NAME(S) AND ADDRESS(ES) AFOSR/NE 4015 WILSON BLVD SUITE 713 ARLINGTON VA 22203			10. SPONSORING/MONITORING AGENCY REPORT NUMBER F49620-01-1-0151
11. SUPPLEMENTARY NOTES			
12a. DISTRIBUTION AVAILABILITY STATEMENT DISTRIBUTION STATEMENT A: Unlimited			12b. DISTRIBUTION CODE
13. ABSTRACT (Maximum 200 words) Stoichiometry-related effects in various group III-nitrides and some GaAs-based materials were investigated. An essential part of this study were low-frequency (LF) noise analyses. The new LF-noise system, acquired with an AFOSR DURIP grant (no. F49620-01-1-0285), was set up and calibrated. LF-noise spectroscopy was then applied to GOI-based MESFET's (noise caused by excess arsenic-related defects) and AlGaIn/GaN HEMTs (channel noise related to an early 2D/3D growth transition for high Al- containing AlGaIn layers rather than a dislocation-related strain relaxation process). Both device types were also processed at UC Berkeley. Different nitride materials were evaluated for its potential of engineering non-stoichiometric epilayers. (intentional manipulation of native defect population) In carbon-doped GaN a new insight into the nature of the ubiquitous yellow luminescence (YL) was gained. The strong Yb. was found to be caused by > a dopant-related effect and to be independent of the concentration of gallium vacancies. Furthermore, co-doping with silicon greatly increased the Yb. which gives further evidence for a donor-acceptor complex as origin of the YL. These studies provide a first proof that a second mechanism for YL exists in GaN that is independent of the presence of Ga vacancies. Consequently, the trapping-detrapping of carriers at deep defects causing noise in carbon doped GaN device structures is dominated by doping-related defects rather than any native defects. A vacancy-related defect was found in post-irradiated GaN, the investigation of vacancy? incorporation upon various growth related conditions and its control requires further research.			
14. SUBJECT TERMS			15. NUMBER OF PAGES
			16. PRICE CODE
17. SECURITY CLASSIFICATION OF REPORT Unclassified	18. SECURITY CLASSIFICATION OF THIS PAGE Unclassified	19. SECURITY CLASSIFICATION OF ABSTRACT Unclassified	20. LIMITATION OF ABSTRACT UL

Abstract

Stoichiometry-related effects in various group III-nitrides and some GaAs-based materials were investigated. An essential part of this study were low-frequency (LF) noise analyses. The new LF-noise system, acquired with an AFOSR DURIP grant (no. F49620-01-1-0285), was set up and calibrated. LF-noise spectroscopy was then applied to GOI-based MESFETs (noise caused by excess arsenic-related defects) and AlGaIn/GaN HEMTs (channel noise related to an early 2D/3D growth transition for high Al-containing AlGaIn layers rather than a dislocation-related strain relaxation process). Both device types were also processed at UC Berkeley.

Different nitride materials were evaluated for its potential of engineering non-stoichiometric epilayers. (intentional manipulation of native defect population) In carbon-doped GaN a new insight into the nature of the ubiquitous yellow luminescence (YL) was gained. The strong YL was found to be caused by a dopant-related effect and to be independent of the concentration of gallium vacancies. Furthermore, co-doping with silicon greatly increased the YL which gives further evidence for a donor-acceptor complex as origin of the YL. These studies provide a first proof that a second mechanism for YL exists in GaN that is independent of the presence of Ga vacancies. Consequently, the trapping-detrapping of carriers at deep defects causing noise in carbon doped GaN device structures is dominated by doping-related defects rather than any *native* defects. A vacancy-related defect was found in post-irradiated GaN, the investigation of vacancy incorporation upon various growth related conditions and its control requires further research.

Additionally, new characterization methods were developed within this project. The effect of non-stoichiometry growth on the incorporation of dopants in GaAs was studied using a newly developed in-situ molecular beam epitaxy defect characterization tool. A first step to locally scan group III - nitrides for areas of large defect concentrations was made by applying for the first time valance electron energy loss spectroscopy (VEELS) to detect electron transitions involving defect bands in GaN and InN (see attachment). Combined defect characterization methods gave a multitude of information about the co-existence of various defect types in group III - nitrides. The various defect distributions and their interaction in the respective epilayers and devices will require additional studies.

1. Introduction

The development of nitride-based devices proceeded rapidly driven by prospective military and commercial applications such as low-noise/high-power electronics, solar-blind detectors and general lighting. However, even the influence of basic defects on the properties of these materials, commonly grown in epitaxial processes at low growth temperatures with respect to the group III - nitrides melting point, remains still unclear. The role of native defects, particularly vacancies, is not well understood and defect characterization methods to accurately quantify them are limited. For one species, the gallium vacancies (V_{Ga}), positron annihilation spectroscopy (PAS) was applied [1], the quantification of nitrogen vacancies (V_N), however, is not as straight forward. The growth of the group III - nitrides, on the other hand, occurs under conditions which promote the incorporation of native defects leading to non-stoichiometry effects. In the other III-V compound systems a non-stoichiometric growth is known to have significant effects on the materials (and device) properties. In this project a variety of different group III - nitride hetero-structures and devices were studied together with some GaAs-based materials and devices. Comparisons were made when possible.

Group III - nitride devices still lack sufficient reliability (yield) and, additionally, also show signs of aging effects. Both phenomena are likely correlated to homogeneities of the epilayers and/or incorporation of vacancies which may result in enhanced diffusion such as intermixing at hetero-interfaces resulting in interface roughening and inhomogeneous charge distribution, and dopant diffusion. Naturally, diffusion is enhanced at elevated device operation temperatures which may not only lead to decreased device efficiency but also to non-reproducible device performance and aging effects. While efforts are ongoing to reduce III-nitride device operation temperatures by utilizing novel substrates with superior thermal properties and/or providing effective heat sinks in modified packaging techniques it will be vital for a broad applicability of these devices to understand and eventually control the incorporation of native defects (vacancies) to suppress diffusion effects in group III - nitrides. Precise local material characterizations to determine the magnitude of the materials inhomogeneities are a first step to quantify those phenomena. Within this project novel characterization methods were applied which provide for a more detailed defect analysis and an opportunity to measure local defect distributions.

In a comparative background study to clarify the formation behavior of native defects in semiconductor III - V compounds, facilitated through presentations and discussions during the fourth International Workshop on Non-Stoichiometric III - V compounds (Oct. 2nd to 4th, 2004, in Asilomar, Pacific Grove, California), the following summary was obtained:

Stoichiometry-related defects vastly differ in the various III-V semiconductor compounds. In previous studies it was found that the As_{Ga} antisites are the dominant defects in LT-GaAs. [2] Those defects have been proposed to be energetically favorable in As-rich GaAs [3]. In GaN the dominant native defects are vacancies on both sublattices [4]. Their formation energy depends on the Fermi Level position but seems not to be influenced by growth stoichiometry in the growth temperature range studied so far. [4]. Nitrogen vacancies, V_N , are always energetically favorable in p-type GaN while in n-type GaN gallium vacancies, V_{Ga} , will prevail.

A formation energy of approx. 1.7eV was calculated for As_{Ga} defects in SI-GaAs versus approx. 2.2eV for V_{Ga} defects, the defects with the second lowest formation energy in SI-GaAs [3]. This corresponds quite well to the general observation of native defect concentrations in LT-GaAs with $[V_{Ga}] \approx 0.01 [As_{Ga}]$. However, the influence of the growth kinetics on defect incorporation will have to be taken into account as well because the MBE growth process for LT-GaAs is far away from thermal equilibrium conditions. The measured V_{Ga} concentration was found in LT-GaAs to be constant over a large range of p-dopant (Be) concentrations, whereas theory predicts that the equilibrium concentration of V_{Ga} triple acceptors should significantly decrease with increased p-type conduction. This is further evidence for the limited usefulness of thermal equilibrium arguments in LT growth.

In GaN, the calculated formation energies of native defects [4] differ only marginally in Ga-rich and As-rich material. Only the Fermi Level position determines under thermal equilibrium conditions which native defect will dominate. Therefore, the stoichiometry of GaN should be widely controlled by its concentration of various dopant impurities, such as oxygen, carbon or silicon. If the incorporation of these defects changes the conductivity of the materials, it should simultaneously affect the incorporation of native defects. The introduction of native defects due to implantation with iso-electronic atoms of the IIIrd or Vth columns is another way to change the stoichiometry. Irradiation was shown to introduce vacancies as well;

electron-irradiated GaN of high crystalline quality (possible supplier: Samsung) is therefore a promising material for LF- noise spectroscopy of native defects. In all cases, a native defect incorporation will partly reverse the Fermi Level effect as vacancies themselves are electrically active and will partly compensate the introduced chemical dopants, therewith shifting the Fermi Level towards their respective defect levels. Defect pairing and/or Fermi Level pinning at energy levels of extended defects further complicate the analysis.

In this study, the effect of different growth conditions on the stoichiometry – or concentration of native defects – of GaAs, dilute arsenide nitrides and GaN, mostly grown at low temperatures, was investigated. It was intended to obtain suitable materials with large and reproducible concentrations of native defects but otherwise high crystalline quality. With low-frequency noise spectroscopy a correlation of the generation-recombination ($1/f^2$) noise to the presence of native defects was attempted. Noise spectroscopy for GOI-based MESFETs, C-doped GaN resistors and AlGaIn/GaN HEMTs were obtained.

2. Low temperature growth of GaAs and defect determination

2.1 In-situ Defect Determination: DRS

In an effort to develop the use of common measurement systems for the evaluation of the defect population in MBE grown III-V epilayers we applied in-situ diffuse reflectance spectroscopy (DRS) to monitor both the substrate temperature transient and the epilayer absorption during low temperature (LT) GaAs molecular beam epitaxy. We have found a significant increase of the sub-bandgap absorption from LT-GaAs. The magnitude of absorption at 1.2eV correlates well with the concentration of arsenic antisite defects. The incorporation rate of arsenic antisites appears uniform despite a substrate temperature transient due to the effusion cell radiation heating. The influence of absorption spectra change on the accuracy of DRS temperature measurement is also discussed. This study shows that DRS can be used for both growth temperature measurement and real-time nonstoichiometry monitoring.

GaAs grown at low temperatures (LT-GaAs) by molecular beam epitaxy (MBE) has been very attractive for GaAs integrated circuit (IC) devices and ultrafast optoelectronics because it combines very high resistivity and ultrashort carrier lifetimes [5,6]. It has been well known that the large amount of excess arsenic atoms in the epilayer plays a critical role in determining the material properties [7-9]. These excess arsenic atoms are incorporated into the lattice mainly in the form of arsenic antisite (As_{Ga}) defects [7], whose concentration can be controlled by the substrate temperature and V/III beam equivalent pressure (BEP) [10,11]. The low temperature growth condition, however, results in the potential for large perturbations due to inaccurate temperature measurements and/or severe effusion cell radiation heating [12]. So it is important to be able to study the incorporation of arsenic antisite defects during growth in order to optimize the material performance for device applications. Furthermore, this relatively simple and non-evasive in-situ measurement may be transferable to other material systems if appropriate light sources (for the energy ranges of the respective defect levels) are available.

Generally, LT-GaAs is grown by MBE at temperatures of 200~400°C, much lower than the conventional GaAs MBE growth temperature (~600°C). Up to ~1.5% excess arsenic can be incorporated as arsenic antisites and the epilayer can still be single crystalline below the critical thickness [13]. Various methods have been used to study the defect incorporation during low temperature epitaxy. Using *in situ* reflectance difference spectroscopy (RDS), Apostolopoulos *et al.* [14] have shown that the amplitude of the linear electro-optical feature near E_1 and $E_1+\Delta_1$ transitions decreases linearly with the neutral As_{Ga} concentration. Gajewski *et al.* [15] revealed distinct signatures of the onset of polycrystalline or amorphous growth beyond the critical thickness using *in situ* spectroscopic ellipsometry (SE). While diffuse reflectance spectroscopy (DRS) is commonly used to measure and/or actively control the relatively low substrate temperature [12,16], we applied this method for the first time for an *in situ* spectroscopic study of As_{Ga} incorporation. Additional below bandgap absorption induced by As_{Ga} was measured and its magnitude correlated well with the As_{Ga} concentration. The influence of this additional absorption on the temperature measurement was also investigated.

DRS is a method to determine the substrate temperature in MBE growth with an accuracy of $\pm 1.5^\circ C$ [16]. In this technique, white light is passing through the wafer from the front side and scattered internally

by the unpolished/patterned backside surface. The non-specular diffuse light from the back surface is collected in front of the wafer and a spectroscopic analysis yields the wafer absorption as a function of photon energy. The characteristic "knee" position in DRS is correlated with the substrate bandgap and can be calibrated for high-precision temperature measurement. Because of the relative thick substrate (300~500 μm) that is traversed twice, the light intensity near the band edge is strongly attenuated. So, DRS is also very sensitive to the weak sub-bandgap absorption [17].

The LT-GaAs samples were grown on semi-insulating (SI) and n^+ (Si-doped, $n \sim 2 \times 10^{18}/\text{cm}^3$) GaAs (001) substrates using a Varian GEN II MBE system equipped with a Thermionics DRS-1000 system. The optical throughput of the DRS system was calibrated with a pyrolytic boron nitride (PBN) diffuser. The "Epi-ready" single-side polished wafers were used to facilitate the DRS measurement. One-quarter of 2" GaAs substrates were wire-bonded to a 3" molybdenum holder. The As_4/Ga beam equivalent pressure (BEP) ratio was fixed at ~ 20 and the growth rate was $\sim 1\mu\text{m}/\text{hour}$. After a 250nm buffer layer was grown at 580°C (the oxide desorption temperature) the substrate temperature was lowered to 200~300°C as measured with DRS. The total growth interruption was about 30 minutes with As_4 shutter open. During LT growth, a constant output power of the substrate heater was applied in order to investigate the effusion cell radiation heating effect. The substrate rotation was stopped to take DRS spectra at different growth times. In this study, the samples were all grown below the critical thickness [13]. The sample lattice constant was determined by the GaAs (004) high resolution X-ray diffraction (XRD) rocking curve. The thickness fringes and narrow peaks (with typical full width at half maximum $\sim 20^\circ$) observed in XRD show the samples have excellent single crystallinity.

Fig. 2.1 shows the typical behavior of the substrate temperature transient measured by DRS during low temperature epitaxy. The start substrate temperature (the nominal growth temperature) was 203°C and 248°C, respectively. The effect of the radiation heating from the Ga effusion cell ($\sim 1100^\circ\text{C}$) can be clearly seen. After the opening of the Ga shutter, the semi-insulating substrate temperature slowly increased by about 12°C within the first 10 minutes and up to a total of about 15°C at the end of the 30 (or 35) minute growth run. It is also noted that the temperature indicated by the thermocouple, which is located in the gap between the substrate and the heater, was almost constant and fluctuated only by $\sim 1^\circ\text{C}$ during this procedure. For SI-GaAs at low temperature, the integrated spectral emissivity for $\sim 1100^\circ\text{C}$ radiation from the Ga-cell is low because the free carrier absorption is negligible [18]. So the substrate temperature response is slow. For an n^+ GaAs substrate, which has large emissivity, the temperature change is much faster upon opening of the Ga cell shutter (Fig. 2.1).

The DRS spectra for the sample grown on SI-GaAs at 203°C are shown in Fig. 2.2a. The spectra were recorded every 5 minutes during growth. A strong decrease of the diffuse reflected light below the bandgap can be seen due to the absorption from the growing low temperature epilayer. The spectroscopic knees shifted to the low energy side as the substrate was heated by the Ga cell, as analyzed in Fig. 2.1. The spectra slopes near the knees become less steep as the LT layer becomes thicker. This is different from the bare GaAs wafer, which shows parallel shifts of the spectra near the knee and unchanged slope as the substrate temperature changes [17]. Following Weilmeier *et al.* [17], the diffuse reflectance is related to the sample absorption through

$$R_{diff} = \frac{(1 - r_f)^2 r_b e^{-2\alpha d}}{n^2 - e^{-2\alpha d} r_f r_b - (n^2 - 1)e^{-4\alpha d}} \quad (1)$$

where r_f and r_b are the specular reflectivity at the sample front side and the back surface reflectivity, respectively, α , the absorption coefficient, n , the sample refraction index and d , the sample thickness. In this experiment, we use $r_f=0.31$ and $r_b=0.25$ [17]. We have found that the bare substrate absorption calculated from DRS using Eq. (1) is comparable with the external transmission measurement. The apparent absorption spectra $\alpha(h\nu)$, normalized to the total sample thickness, were calculated from the DRS results (Fig. 2.2a) using Eq. (1) (see Fig. 2.2b). It is evident that there is a strong increase of the absorption with increasing layer thickness. It has been shown that in as-grown LT-GaAs, the arsenic antisite defect, As_{Ga} , has the characteristic EL2-like sub-bandgap absorption near $\sim 1.2\text{eV}$ [19-21]. So we attribute the observed excess absorption below the GaAs band edge to As_{Ga} induced absorption in LT-GaAs. The absorption is broadened due to the strong defect-phonon coupling and no distinct intracenter absorption can be seen, which is similar to the room temperature *ex situ* absorption measurement. It is also almost

temperature independent before merging into the large substrate band tail absorption for the temperature above 250°C (Fig. 2.2c).

To further study the As_{Ga} induced absorption, we also performed *in situ* annealing studies monitored by DRS and the results are shown in Fig. 2.2d. The samples were protected under As overpressure during annealing. We noted that the DRS spectra start to recover rapidly when the substrate temperature reaches 400°C, presumably due to As out diffusion and the formation of As precipitates [9]. Surprisingly, the spectra recovery is not 100% even after 30 minutes annealing at 600°C. This might be caused by changes of the sample optical property due to the existence of As precipitates.

These results demonstrate that DRS provides a way to *in situ* monitor the As_{Ga} incorporation, in addition to measure the substrate temperature. We can see from Fig. 2.3a that the change of the apparent absorption at 1.2eV is almost linear with the growth time although the substrate temperature had changed by more than 10°C. For the 250°C grown sample, the substrate temperature transient increased by more than 10°C during the first 10 minutes growth (Fig. 2.1) and the defect absorption measured at 1.2eV suffers the influence from the band tail absorption (Fig. 2.2c). So the linear fit was done without the consideration of the first 10 minutes growth. We can deduce the epilayer absorption from the slope of the curve in Fig. 2.3a by

$$\alpha = \alpha_0 + \alpha_{epi} \frac{r}{d} t \quad (2)$$

where α_0 is the absorption from the substrate with a thickness d (~325 μ m), α_{epi} is the LT epilayer absorption, and r , the growth rate. A good linear correlation is obtained between the epilayer absorption at 1.2eV and the arsenic antisite concentration, which was determined from the LT-GaAs (004) lattice mismatch measured externally at room temperature [20] (Fig. 2.3b). The arsenic antisite absorption at 1.2eV from room temperature near infrared absorption (NIRA) measurement is also plotted in Fig. 2.3b, using Martin's calibration [21] (solid line). It should be pointed out that the optical cross section for As_{Ga} absorption at 1.2eV photon energy deduced from Fig. 2.3b is $8.0 \times 10^{-17} \text{cm}^2$ at the growth temperature (200 ~ 250°C), which is only about 62% of Martin's room temperature calibration [21]. This might be due to the slightly larger refraction index of LT-GaAs [22], the uncertainty of the optical constants in Eq. (1) and the PBN calibration wafer, and the possible quenching of some of the As_{Ga} absorption by the strong illumination from the DRS light source [19]. The comparison of NIRA and DRS both measured at room temperature is shown in the inset of Fig. 3.3b. This result allows to conclude that the *in situ* 1.2eV absorption allows to measure the absolute As_{Ga} concentration once calibrated with *ex situ* NIRA measurement.

The exponential absorption edge of the crystalline semiconductor is known as Urbach edge, which describes the band tailing due to the thermal fluctuation induced disordering in the crystal lattice [23]. In Fig. 2.2 the change of the DRS slope near the spectroscopic knee corresponds to a change of the characteristic energy of the Urbach edge. By fitting the absorption spectra with an exponential function, we have noted that the Urbach energy also changes linearly with the growth time, starting from $8.5 \pm 0.5 \text{meV}$ for the bare substrate to $11.2 \pm 0.5 \text{meV}$ after 0.5 μ m LT-GaAs growth. The substrate temperature increase alone can not result in such a big Urbach energy change [23] and we believe it is related to native defect induced disorder. It should be noted that the true Urbach energy of LT-GaAs could be much larger than 11.2meV, since the contribution from the thick substrate absorption was not excluded. But it raises a serious question about the DRS temperature measurement. Though different algorithms to extract the epilayer-insensitive knee position were proposed [16,24], the large increase of the Urbach energy could shift the knee position and introduce a systematic temperature measurement error (over-estimation), according to Ref. 24. This effect might contribute to the slowly rising temperature transient seen after 10 minutes growth for both SI and n^+ substrates (Fig. 2.1). Therefore, caution must be applied when using the DRS temperature measurement for the active heater control. Further experiments are needed to evaluate the Urbach energy change induced error on the temperature measurement.

In summary, we have observed the increase of the below bandgap absorption using *in situ* DRS during LT-GaAs growth and attributed it to the incorporation of As_{Ga} defects. The linear correlation between the below band gap absorption and As_{Ga} concentration suggests that DRS can be useful for both temperature measurement and *in situ* nonstoichiometry control of LT-GaAs. This method could also be applied for

other material systems if the respective defect absorption energy is below band gap and a suitable light source is available.

2.2 Overview: Reproducible LT-GaAs growth

Several thin film growth parameters and their effects on the reliability of low temperature grown GaAs are discussed. For more than a decade GaAs, grown by Molecular Beam Epitaxy (MBE) at low temperatures, is used as a semi-insulating and/or radiation hardened buffer layer in high-speed electronic devices or in opto-electronic devices utilizing its ultrafast carrier trapping. However, some materials properties are still discussed controversially. It is our understanding that the diverse results originate to a large extent from differences in the control of the growth process.

The low temperature growth, which results in a largely non-stoichiometric single crystalline epilayer, sensitively depends on a variety of growth parameters such as growth temperature and beam flux ratios, but also on the growth rate, choice of substrate or arsenic molecule species and even on the degree of contamination present in the chamber. Epilayers, which are nominally grown at the same growth temperature using thermocouple readings, may contain up to one order of magnitude different As antisite defect concentrations. This can be caused by a difference in the thermal conductivity of the GaAs substrates. Be-doped LT-GaAs, grown with the same growth parameters, may show two orders of magnitude different carrier concentration, which may be due to a different contamination background. In this study an attempt is made to quantify these dependencies and determine the growth parameter regime for reproducible growth and annealing conditions.

When GaAs is grown at substrate temperatures below 400°C in Molecular Beam Epitaxy under arsenic-rich conditions, the resulting single crystalline epilayer is highly non-stoichiometric containing up to one percent more arsenic than gallium. The incorporation of excess arsenic leads to large concentrations of arsenic on the gallium sublattice, mostly in the form of the arsenic antisite (As_{Ga}) defect. Also present, but in concentrations up to two orders of magnitude lower than the As_{Ga} defects, are gallium vacancies (V_{Ga}). The As_{Ga} double donors are partly compensated by the triple acceptors V_{Ga} . These two defects determine the electronic properties of undoped low-temperature grown (LT-)GaAs epilayers. In particular, As_{Ga} defects pin the Fermi Level midgap, resulting in semi-insulating epilayers and the positively charged As_{Ga}^+ compensated by the V_{Ga} act as very effective electron traps, which is the cause of the ultrafast time response and the enhanced radiation hardness of this material.

In undoped LT-GaAs, the concentration of As_{Ga} defects can in first order be determined by measuring the positive lattice mismatch between the epilayer and its GaAs substrate [2]. Figure 2.4 shows the strong dependence between the As_{Ga} and the V_{Ga} concentrations including data from undoped and Be-doped LT-GaAs epilayers. Beryllium is a commonly used acceptor for MBE-grown GaAs. In LT-GaAs it is compensated by the native As_{Ga} defects, but with careful selection of deposition parameters can nevertheless be used for ultrahigh p-doping because the low temperature growth kinetics allow for a large incorporation of dopants far beyond the solubility limit of Be in GaAs. [25].

The onset of poly-crystallinity of LT-GaAs, the conductivity of the epilayer, its ultrafast time response and its thermal stability are sensitively dependent on a variety of growth parameters. Only two of them, the substrate temperature and the BEP ratio, were studied in detail. However, several dependencies, in part even for these growth parameters, have not yet been published. They are therefore summarized here. Details about the MBE growth can be found in [26].

The foremost considered growth parameters in low-temperature epitaxy are obviously the substrate or growth temperature and the beam flux ratios. For LT-GaAs, often the beam equivalent pressure ratio (BEP ratio) is measured which commonly has an accuracy of $\pm 10\%$. A steep increase in antisite incorporation with BEP ratio corresponding to only slightly As-rich conditions is observed [26] which complicates reproducible epilayer growth at these BEP ratios. Therefore, LT-GaAs epilayers are commonly grown at BEP ratios around 20 or higher. Because of the same large increase of antisite defects with growth temperature, defect incorporation is most difficult to control between 200 and 250°C.

However, even the determination of the growth temperature itself, which was in detail investigated, is still the origin of many misunderstandings among different research groups. It has been known for many years that thermocouple readings in an MBE system can be highly inaccurate. The growth on chemically

different substrates, such as in hetero-epitaxy, provided for cautious use of extrapolated thermocouple readings. However, these extrapolations are still used when growing LT-GaAs because its deposition on GaAs substrates seemed to be well understood.

Simultaneously with the development of LT-GaAs epilayers, different substrate temperature measurement techniques were invented, commonly based on the evaluation of a substrate absorption spectrum, which is sensitively dependent on the substrate temperature. One of these methods is the Diffuse Reflectance Spectroscopy (DRS, Thermionics NW Inc). This method, which is routinely used for MBE growth at UC Berkeley, allows for a measurement accuracy of about $\pm 2^\circ\text{C}$. We found that the optical absorption of antisite defects can be detected by DRS so that it can even be used to evaluate the defect concentration of neutral As_{Ga} during growth [27], which enables the grower to determine variations of defect incorporation during growth.

With the availability of DRS temperature measurements, actual substrate temperature differences can be measured for nominally the same thermocouple readings. Figure 2.5 shows an example: Large, systematic differences in DRS temperature readings for semi-insulating and n-conductive GaAs substrates were observed for the same respective thermocouple temperature reading and otherwise similar growth conditions. Both substrate types were used in LT-GaAs research areas and the results were often compared utilizing thermocouple readings. At low growth temperatures around 200°C the differences in actual temperature (DRS) can be as large as 80°C with the semi-insulating substrate generally exhibiting significantly lower actual substrate temperatures or its epilayer exhibiting more than one order of magnitude different defect incorporation than the epilayer grown on n-conductive substrate. This example demonstrates that accurate substrate temperature measurement is vital for LT-GaAs research.

Besides an accurate growth temperature measurement and a sufficiently high beam flux or beam equivalent pressure (BEP) ratio, also the growth rate is an important parameter, which should not be neglected when comparing LT-GaAs epilayer properties. The incorporation of native point defects is illustrated in Figure 2.6 using the corresponding lattice mismatch in samples grown at different growth rates.

The defect incorporation is generally found to increase with increasing growth rate, which is consistent with the low-temperature growth being limited by the diffusion of gallium adatoms. A low growth rate corresponds to more time for a Ga adatom to move on the growth surface till finally being incorporated on a Ga sublattice place. Therefore, less native point defects are present for low growth rates. At high growth rates, the incorporation of native point defects, As_{Ga} and V_{Ga} , reaches a saturation level, which is dependent on the BEP ratio and the growth temperature.

Similar to the BEP ratio and the growth temperature, the native defect incorporation with growth rate also has a parameter range where the defect incorporation is very sensitive to small growth parameter fluctuations, and another parameter range in which defect incorporation saturates. Growth rates below $1 \mu\text{m/hr}$ will lead to less reproducible epilayer properties than higher growth rates.

The above examples demonstrate that low-temperature growth is extremely challenging for very low growth temperatures, low BEP ratios and low growth rates. While low growth temperatures are also known to compromise the crystalline quality of the epilayers due to enhanced defect incorporation, low BEP ratios and growth rates will result in decreased defect incorporation. The choice of higher BEP ratios and growth rates for reproducible LT-GaAs growth is therefore not as straightforward, but might be necessary for an optimized, defect-engineered material.

Another aspect of complicated low-temperature growth is the enhanced incorporation of all defects, including contamination elements. Carbon doping of LT-GaAs, utilizing a gaseous CBr_4 source, is known to have the undesirable side effect of large incorporation of Br atoms or molecules at growth temperatures below 250°C [28]. The presence of large concentrations of Br changes the incorporation of native defects, which strongly impedes defect engineering for designing epilayers with specific electronic properties.

A phenomena that remains unexplained to date, which coincides with an increased contamination (C, N, O, H) in the MBE system, was observed in Be-doped LT-GaAs. Figure 2.7 shows the paramagnetic part of MCDA spectra, obtained by subtracting the diamagnetic absorption signal. Details of this method can be found in [29]. Additionally to the known energy peak around 0.9eV , correlating with the positive As_{Ga}^+

defect concentration, a second peak around 1.2eV was found which does not correlate with the neutral As_{Ga}^0 , a diamagnetic defect. This unknown defect is strongly dependent on the growth temperature but in first order independent of the Be-doping. When it was present in LT-GaAs epilayers, an up to two orders of magnitude increased free hole concentration was observed. Defect engineering of doped LT-GaAs was found to be largely aggravated. The identification of this defect is in progress. Hydrogen is an unlikely candidate to explain this behavior as its effect on the p-doping would be to passivate the acceptors which would result in lower dopant activation. This is in contrast to the observed materials properties. C_{As} will increase the p-doping as it is an acceptor in GaAs. Also, if C_{As} would be present in large concentrations, it could form a donor-acceptor complex with the native As_{Ga} . If enough carbon is found in the respective epilayers to describe the observed materials properties, electron paramagnetic resonance may be used to discover a changed symmetry of a possible antisite defect complex.

Summarizing, the conditions for a reproducible LT-GaAs growth were discussed in detail. It is recommended to grow at moderate temperatures ($\approx 250^\circ\text{C}$ and higher) as well as with higher BEP ratios and growth rates (BEP ≈ 20 / growth rate $\approx 1\mu\text{m/hr}$). Accurate substrate temperature measurements are a necessity. Fast carrier response times can still be accomplished at these higher growth temperatures when utilizing Be doping. However, residual contaminants may impact the conductivity of doped epilayers as well as the concentration of native point defects. Defect engineering will only be successful if all growth parameters mentioned above are taken into account.

2.3 Ultrahigh-doped epilayers and their native defects

Low-temperature thin film growth is commonly defined with respect to the materials melting point. Only deposition temperatures below approximately half of the melting temperature (measured in Kelvin) are considered to be low. Generally, low-temperature growth introduces native point defects, strained crystals and, above a certain critical thickness, extended defects and multi-crystalline growth. In this respect, low-temperature MBE grown GaAs is a unique material because its onset of poly-crystallinity occurs at astonishingly low temperatures. Even at 30% of the melting temperature epilayers can still be grown several of micrometers thick without an increase in dislocation density or multi-crystalline growth. However, this material contains a large amount of native point defects and therewith allows for detailed investigations of stoichiometry-related effects.

In this chapter we describe our studies of ultrahigh doping in LT-GaAs epilayers. It was our goal to develop a materials system with enhanced p-doping which can be incorporated into a device structure, e.g. an AlGaAs/GaAs HBT. The limited incorporation of beryllium at common growth temperatures (about 250°C) was largely exceeded and despite a significant compensation effect due to the native defects we achieved a record free hole concentration. We expect that some of our results can be transferred to other III-V compounds, also nitrides.

Non-stoichiometric GaAs is produced in Molecular Beam Epitaxy at temperatures around 250°C . Research on LT-GaAs was mainly focused on two electronic properties, its ultrafast time response and semi-insulating behavior. The supersaturation of native point defects, mainly As antisites (As_{Ga}), which cause these special properties, increases the lattice constant of LT-GaAs, resulting in a tetragonal distortion of the lattice below a critical thickness in the order of a few micrometer (pseudomorphic growth). The incorporation of excess As depends on various growth parameters and its reproducibility was studied in great detail. It was found that undoped epilayers can be characterized by their lattice mismatch to the substrate, a measure of the dominant (neutral) As_{Ga} defect concentration [20]. The corresponding concentration of incorporated native acceptors, namely gallium vacancies (V_{Ga}), can be estimated with $[V_{Ga}] \approx 0.01 [As_{Ga}]$ [30]. These acceptors partly compensate the As_{Ga} donors. The small concentration of ionized As_{Ga}^+ act as fast electron traps resulting in ultrashort time response while the Fermi Level is pinned at the approximately midgap As_{Ga}^0/As_{Ga}^+ defect level leading to semi-insulating behavior. LT-GaAs epilayers show different behavior upon annealing dependent on their initial defect concentration and doping level [31,32].

Be-doping of LT-GaAs can result in conductive or insulating layers dependent on the relative concentrations of native deep level defects and Be acceptors. Ultrahigh concentrations of Be, which are Be doping levels of $10^{20}/\text{cm}^3$ or higher, can be incorporated into the epilayers and result in free hole concentrations of up to $7 \times 10^{20}/\text{cm}^3$ [33,34]. If the Be doping exceeds roughly twice the concentration of

native As_{Ga} defects the epilayer becomes gradually less thermally stable under overgrowth conditions (600°C, 30min.). Such annealing results in largely reduced free hole concentrations due to Be diffusing out of the epilayers and/or Be clustering. For a prospective use in a device structure with an embedded LT-GaAs:Be layer n-conductive LT-GaAs layers have been developed. Overgrowth at low temperatures can prevent the epilayers deterioration due to beryllium out-diffusion. The development of n-conductive LT-GaAs therefore enables larger applicability of conductive LT-GaAs.

Arsenic-rich GaAs layers were grown by Molecular Beam Epitaxy (MBE) using the diffuse reflectance spectroscopy (DRS) for temperature control. A beam equivalent pressure (BEP) ratio of 20 was applied. The epilayers are between 0.4µm and 1.0µm thick and were grown at growth rates of 1.0 µm/hr for Be-doped LT-GaAs and 0.5 µm/hr to 0.25 µm/hr for Si-doped LT-GaAs. The reduced growth rate for LT-GaAs:Si was chosen to protect the Si Knudsen cell against overheating. However, preliminary studies showed that a reduced growth rate also leads to a reduction in the native defect concentration. For a growth of 0.5 µm/hr an approximate reduction of 20% As_{Ga} was estimated. Sample series were grown by varying the growth temperature and the doping concentrations. The current study includes as-grown samples only. Some Be and Si concentrations were measured by SIMS, the others were interpolated from the Knudsen cell temperatures. As_{Ga} defect concentrations were obtained by near-infrared absorption (NIRA: $[As_{Ga}^0]$) and magnetic circular dichroism of absorption (MCDA: $[As_{Ga}^+]$). The lattice mismatch parallel to the growth direction ($\Delta c/c$) was measured by x-ray diffraction (XRD) using the (004) reflection. Carrier concentrations were determined by Electrochemical Capacitance Voltage (ECV) profiling or using Hall effect measurements in Van der Pauw geometry.

The lattice mismatch of LT-GaAs:Be is known to decrease with increasing doping level due to the size difference between the Be dopant atom and the Ga host atom [32]. Doping LT-GaAs with silicon is not expected to change the lattice constant at all for the doping levels used in this study. However, a reduction of the lattice mismatch $\Delta c/c$ in LT-GaAs is observed for higher Si doping concentrations as can be seen in Fig. 2.8. The reduction occurs at different doping levels for the chosen growth temperatures and at higher [Si] for the epilayer with higher native defect concentration. The decrease in $\Delta c/c$ is caused by a reduction of neutral As_{Ga} . This behavior has been found in bulk Si-doped GaAs for $[Si] > 10^{17}/cm^3$ [35]. Due to a change in the defect formation energy with the Fermi Level approaching the conduction band energy the As_{Ga} concentration is expected to be reduced while the V_{Ga} concentration increases. A similar effect can explain the reduction of $\Delta c/c$ in LT-GaAs:Si. However, as the V_{Ga} triple acceptors, which are deep level defects, compensate the Si donors in non-stoichiometric GaAs the Si concentration in the epilayers needs to be higher than three times the V_{Ga} concentration in order to achieve a significant change in the Fermi Level energy. Consequently, such an effect will have to occur at larger Si doping levels for lower growth temperatures (larger native defect concentrations) which is consistent with the data shown in Fig. 2.8.

Figure 2.9a gives the free electron concentration in LT-GaAs:Si for different Si doping levels. The solid line corresponds to fully activated dopants ($[Si] = [n]$). As can be seen the epilayers are heavily compensated. This effect may be caused by several different mechanisms: a) a compensation due to the native acceptors, the V_{Ga} , b) the incorporation of silicon on the arsenic sublattice resulting in auto-compensation as silicon is amphoteric, c) the formation of Si-pairs or even larger Si-clusters. Despite of the large compensation, ultrahigh free electron concentrations are also achieved in LT-GaAs:Si. Fig. 2.9b gives the situation for ultrahigh doped LT-GaAs:Be for comparison. Ultrahigh hole concentrations as reported earlier [34] were reproduced with the epilayers grown between 210°C and 250°C. Also in LT-GaAs:Be part of the dopants are compensated, likely due to the presence of native defects. In all samples the incorporated Be is thermally more stable than in normally grown GaAs:Be. This confirms that the dopant is still incorporated on substitutional sites as interstitial Be is known to be a fast diffuser [36]. Furthermore, neither structural defects nor (Be) clusters were found by TEM in the samples with Be doping levels given in Fig. 2.9b. Only at even higher Be concentrations a formation of structural defects was observed [37]. Therefore, it is assumed that the compensation of Be is due to the presence of As_{Ga} double donors throughout the shown Be doping regime.

For ultrahigh conductive LT-GaAs:Be epilayers the As_{Ga} concentration present in these layers cannot be determined by NIRA (As_{Ga}^0) or MCD (As_{Ga}^+) because the defects must be double positively charged as the As_{Ga} defect is a double donor. We estimated the upper limit of As_{Ga}^{++} possibly present in the epilayers through the difference between the Be doping concentration and the free hole concentration [p]:

$$[As_{Ga}^{++}] \leq 0.5 \times ([Be] - [p])$$

The results are shown in Fig. 2.10 for high Be doping. An increase of the estimated As_{Ga} density is observed which is consistent with the expected defect behavior in GaAs for Fermi Level energies close to the valence band. However, for very high Be doping concentrations the As_{Ga} density seems to decrease again with a simultaneously observed de-stabilization of the Be atoms upon annealing. These results indicate that the As_{Ga} defects indeed stabilize the Be dopants if the native defects are present in concentrations higher than or comparable to the Be concentration. A less compensated epilayer, which translates to a smaller amount of As_{Ga}^{++} , will then be less thermally stable as observed [34]. Achieving highest free hole concentrations therefore compromises the stability of the Be in the non-stoichiometric epilayer. In order to utilize ultrahigh doped epilayers a non-stoichiometric device structure containing several LT-epilayers has to be developed or less conductive LT-GaAs:Be has to be used which is stable upon overgrowth.

In Si-doped LT-GaAs the doping should lead to fewer ionized As_{Ga} defects as the silicon compensates the V_{Ga} , the deep level acceptors in As-rich GaAs. Indeed, we observe only small or no signals from the paramagnetic As_{Ga}^+ defects in MCD for LT-GaAs:Si. The NIRA signals are constant for low Si-doping concentrations and then gradually disappear with higher Si doping levels (Fig. 2.11a) as we expected from the x-ray diffraction results (disappearing lattice mismatch, Fig. 2.8). Neutral As_{Ga}^0 concentrations are summarized in Fig. 2.11b for a growth temperature of 250°C. The decrease in the As_{Ga} concentration matches with the decreasing lattice mismatch. Simultaneously, an increase in the V_{Ga} concentration is expected which would result in larger Si doping compensation. It still has to be determined to which extent a prospective increase of the V_{Ga} density can describe the large electrical compensation in LT-GaAs:Si. It is likely that also other compensation mechanisms play a role.

Summarizing, conductive LT-GaAs:Be and LT-GaAs:Si with doping levels of up to $8 \times 10^{20}/cm^3$ were grown and their defect behavior studied. In both materials, free carrier concentrations of $10^{20}/cm^3$ are well exceeded and a change in native defect concentration is observed for these very high doping levels. The change of the native defect densities can be ascribed to Fermi Level effects in GaAs showing an increase of the As_{Ga} density in Be-doped LT-GaAs and a decrease in Si-doped LT-GaAs. The V_{Ga} density is expected to change in the respective opposite direction. LT-GaAs:Be shows an increased thermal stability even in the conductive doping regime which is correlated with the presence of large concentrations of As_{Ga} defects which stabilize the dopant atoms. In the highest doping regime, the thermal stability of LT-GaAs:Be breaks down with a simultaneous decrease of $[As_{Ga}]$ [33,34]. Using this ultrahigh conductive material as an intermediate layer in a device structure, for example as base layer in an AlGaAs/GaAs HBT, despite of thermal instabilities therefore requires a low-temperature overgrowth. As a first step in the development of a new device with active LT-grown epilayers ultrahigh conductive LT-GaAs:Si was developed.

The lattice-matched LT-GaAs:Si does not contain As_{Ga} defects in concentrations above $10^{18}/cm^3$. However, V_{Ga} defects may be present in large concentrations which may affect the diffusion behavior in this material. Enhanced interdiffusion of heterostructures may occur and / or increased dopant diffusion. Other Si-related defects like Si on an As-sublattice, Si pairs or clusters may also be present in these epilayers.

LT-GaAs:Be and LT-GaAs:Si can easily be reproduced and grown without structural defects. However, the thermal stability of the Si-doped LT-GaAs and its behavior in a device structure with a p-n junction still has to be investigated. Also, a reduced carrier concentration and / or reduced carrier mobility due to alloying of non-stoichiometric III-V materials may occur in a heterostructure device. Overall, the possibility of achieving ultrahigh conductive epilayers due to low-temperature growth by applying extreme high doping levels is very promising and may find several applications in the near future.

2.4 Nitrogen Incorporation in LT-GaAs: Native Defects

The effect of small amounts (1%-8%) of nitrogen in LT-GaAs was investigated. The addition of nitrogen into conventional III-V compound semiconductors, e.g. GaAs or GaP and their alloys, even in the percentage range, lowers the host material bandgap (E_g) significantly because of the large bandgap bowing parameter. This has been attributed to the strong interaction between the conduction band (CB) edge states and the localized, resonant nitrogen states inside the CB, which causes band anti-crossing and reduces E_g by pushing the CB edge downward [38]. Band anti-crossing also leads to a large CB offset, which can improve the temperature performance of a long-wavelength laser. Although both the 1.3 μm edge emitting laser and the vertical cavity surface emitting laser (VCSEL) have been demonstrated with (In)GaAsN [39],

some fundamental material issues have not yet been solved. Nitrogen incorporation induces defects which degrade the alloy optical qualities. This is not yet clearly understood [40,41]. Phase separation and strain relaxation seems to limit nitrogen incorporation because of the low nitrogen solubility in GaAs. These effects are technologically and scientifically important. The former limits device applications while the latter helps to understand the basic physical principles underlying the growth of new alloys. We investigated the possibility to grow GaAsN by low temperature molecular beam epitaxy (LT MBE) (<400°C). The kinetic restrictions at low temperature could increase nitrogen incorporation into GaAs without phase separation or lattice relaxation. Our goals are to increase the nitrogen incorporation and to identify the defects possibly incorporated during growth.

Samples were grown on semi-insulating GaAs (100) substrates using a Varian GEN II MBE system equipped with a DC constricted nitrogen plasma source. The growth of high quality InGaAsN layers has been demonstrated using the DC plasma source, which provides an active nitrogen plasma with low ion density and low ion energy [42]. After a 0.2µm GaAs buffer layer was grown at 580°C, the substrate temperature was lowered to the desired GaAsN growth temperature T_g (200~460°C), determined by diffuse reflectance spectroscopy. The As₄/Ga beam equivalent pressure was kept at ~20. The structural and optical properties were determined using high resolution X-ray diffraction (XRD) and room temperature photoluminescence (PL), respectively. Near infrared absorption (NIRA) and magnetic circular dichroism of absorption (MCDA) measurements were performed at low temperature (1.8K) to identify point defects incorporated during the low temperature growth.

Fig. 2.12 shows the XRD rocking curves near GaAs (004) for GaAsN layers grown at different temperatures, but with the same N plasma conditions (N₂ flow rate $F = 4$ sccm, discharge current $I = 8$ mA) and growth rate ($g = 1$ µm/hr). The lattice mismatch, which is proportional to the peak separation, is nearly constant when changing T_g from 580°C to 300°C, with a maximum lattice mismatch near 400°C. The asymmetrical rocking curve scans near GaAs(224) indicate a negligible amount of in-plane lattice mismatch in these samples, which confirms the pseudomorphic growth. The nitrogen content is estimated to be almost constant at ~0.9% from the lattice mismatch [42].

This indicates that the active nitrogen species, either atomic nitrogen or excited nitrogen molecules, has a temperature independent sticking coefficient. Thus, the nitrogen incorporation is diffusion or supply limited. It is also noted that the XRD peak width of the GaAsN layers (at ~0.15° in Fig. 2.12) decreases with the growth temperature. The thickness fringes additionally observed show the high structural quality of these layers despite the low temperature growth.

Either increasing the plasma discharge current or nitrogen flow rate, or decreasing the growth rate can increase the nitrogen supply. The resulting XRD curves are shown in Fig. 2.13 for $T_g=300$ °C. Low temperature growth is necessary to preserve the sample surface morphology for a wide range of growth conditions. It is evident that the nitrogen incorporation increases with the nitrogen supply and the sample structural quality degrades at high nitrogen supply, as seen by the broadening of XRD peaks. The asymmetric rocking scan near GaAs(224) also indicates a full lattice relaxation in sample (d). All the samples have mirror-like, smooth surfaces, while the corresponding high temperature samples tend to have milky surfaces and no XRD peaks from the epilayer are detected. The normal θ -2 θ scan shows no sign of a GaN phase. Taking into account the lattice relaxation, the highest nitrogen content incorporated is estimated to be ~8% (Fig. 2.13d), almost twice as high as could be achieved at normal growth temperatures (>460°C) without phase separation or surface breakdown.

Fig. 2.14 shows room temperature photoluminescence measurements from samples grown with the same plasma conditions ($F=4.0$ sccm, $I= 8$ mA, 1 µm/hr) at various temperatures. A peak at 1.24eV is observed and attributed to band-to-band transitions red shifted from the GaAs bandgap by 0.18eV as a result of nitrogen incorporation. Although XRD indicates high structural quality (Fig. 2.12), the PL intensity drops significantly when lowering the growth temperature. The PL peak position and full width at half maximum (~50meV) remains unchanged, consistent with the constant nitrogen incorporation (Fig. 2.12). The reduced PL signal is probably due to the incorporation of defects during low temperature growth, which act as non-radiative recombination centers.

Fig. 2.15 shows the results of optical absorption spectroscopy at low temperature, which is used to investigate the incorporation of point defects in low temperature grown samples. As expected, the absorption edge is red shifted as the nitrogen contents increases (bottom plot). The details of the absorption below E_g are shown in the inset. An absorption shoulder can be clearly seen near 1.2eV (or 1.0eV) and it is

quenchable by white light illumination (dotted line), which are the characteristics of the arsenic antisite (As_{Ga}) intra-center absorption in GaAs [43]. The band-edge transition in GaAsN is dominant in the MCDA and no signal of As_{Ga}^+ can be detected. The As_{Ga} concentration, $[As_{Ga}]$, can be estimated to be in the range of $10^{19}/cm^3$ [43]. Compared with LT-GaAs grown under similar conditions but without nitrogen, $[As_{Ga}]$ is reduced by about 50%. The reduction is probably due to the nitrogen impingement and adsorption during growth, which may reduce As adsorption at the growing surface. This finding clarifies previous optical detected magnetic resonance results, which have been attributed to either As_{Ga} or Ga interstitial, as being probably due to As_{Ga} [40]. It is also interesting to note that the As_{Ga} concentration not only decreases, but the energy of the intracenter transition is also red shifted as the nitrogen content increases (Fig. 2.15). As_{Ga} can act as effective non-radiative recombination center and degrade PL dramatically. No other defects related to nitrogen are detected.

The nitrogen incorporation was found to depend on several growth parameters. The results allowed us to define a phenomenological growth parameter r to quantify the nitrogen supply:

$$r = \frac{F \cdot I}{g}$$

where F is the nitrogen flow rate in sccm, I is the plasma discharge current (mA), and g is the growth rate ($\mu m/hr$). In Fig. 2.16, the nitrogen content in the epilayer, grown at low temperature or at $460^\circ C$, is replotted as a function of the growth parameter, r . Two growth regimes can be found. When the nitrogen supply is low (small r), the growth is pseudomorphic for $300^\circ C$ and $460^\circ C$. The lattice strain, or, the equivalent N content, is proportional to r . When the N supply is high (large r), three dimensional faceting growth is obtained at $460^\circ C$, which is probably a result of phase separation. At low temperature ($<300^\circ C$), the growth is still nearly two-dimensional, as seen by the streaky reflection high energy electron diffraction pattern (RHEED), but the lattice is almost fully relaxed, which was measured by the asymmetric GaAs(224) XRD rocking curve. In addition, we noted that lattice relaxation occurs as soon as the nitrogen plasma is turned on, and not only after a certain critical thickness is exceeded. Simultaneously, the RHEED pattern changes from (1×1) to $(2 \times 1)/(2 \times 3)$. This is probably due to a change of the surface reconstruction when the surface nitrogen atom population increases. The highest $[N]$ obtained in this study is estimated to be 8%.

Summarizing, the low temperature growth of GaAsN using plasma assisted MBE suppresses the phase separation and higher $[N]$ can be achieved. However, the epilayers still exhibit lattice relaxation. The optical quality of the GaAsN layers grown at low temperatures is significantly degraded. As_{Ga} is identified by optical absorption and is probably the dominating defect incorporated. The As_{Ga} concentration is significantly decreased in LT-GaAsN if compared with LT-GaAs grown at similar growth conditions. Other defects, especially nitrogen related ones, were not observed.

3. C-Doped GaN Epilayers and their Native Defects

The investigation of stoichiometry-related defects in the III-nitrides is facilitated by materials which can be produced with different concentrations of specific defects. Such materials can be systematically studied, their defects characterized and their properties measured. Furthermore, the performance of devices which are processed from these materials can be correlated to the formerly characterized defects.

The incorporation of carbon in GaN was found to be accompanied by a strong increase of the yellow luminescence, a signal commonly associated with the presence of V_{Ga} . Therefore, carbon-doped GaN was expected to be a promising candidate to study the effect of V_{Ga} on low-frequency noise (LFN). Carbon-doped GaN layers grown by molecular-beam epitaxy are studied with photoluminescence and positron annihilation spectroscopy. Semi-insulating layers doped with $>10^{18} \text{ cm}^{-3}$ carbon show a strong luminescence band centered at $\sim 2.2 \text{ eV}$ (yellow luminescence). The absolute intensity of the 2.2 eV band is compared with the gallium vacancy concentration determined by positron annihilation spectroscopy. The results indicate that a high concentration of gallium vacancies is not necessary for yellow luminescence and that there is in fact a direct relationship between carbon and the 2.2 eV band. Markedly different deep-level ionization energies are found for the high-temperature quenching of the 2.2 eV photoluminescence in carbon-doped and reference samples. We propose that while the V_{Ga} model of Neugebauer and Van de Walle [44] explains the yellow luminescence in GaN of low carbon concentration, a different yellow luminescence mechanism is involved when the interstitial carbon concentration is comparable to or exceeds the gallium vacancy concentration.

Deep levels have a significant impact on the performance of semiconductor devices. An important deep-level phenomenon in GaN is the yellow luminescence (YL) band, the origin of which has been a subject of considerable debate. Impurities [45-47], native point defects [44,48], and dislocations [49] have all been investigated as possible sources of the YL. Ogino and Aoki proposed an early model for the mechanism based on their studies of carbon-doped GaN crystallites [45]. They proposed a radiative transition from a shallow donor to a C_N-V_{Ga} deep acceptor complex to be responsible for the YL. However, YL can be observed in GaN of relatively low carbon concentration. Also, C_N-V_{Ga} complexes are unlikely to form in n-GaN since both defects are negatively charged, as pointed out by Neugebauer and Van de Walle [44].

Based on defect formation energies obtained from first-principles calculations, Neugebauer and Van de Walle argued that while V_{Ga} is most likely the deep level responsible for YL, carbon is not involved in the mechanism [44]. The YL was attributed to a transition between a shallow donor (Si_{Ga} or O_N) and a deep acceptor V_{Ga} . The assignment of V_{Ga} as the deep level is supported by positron annihilation spectroscopy (PAS) results which found the YL intensity in n-type GaN to be correlated well with the V_{Ga} concentration [1]. Additionally, increased YL intensity has been observed after lattice damage by irradiation with energetic particles [50]. This observation is consistent with an intrinsic point defect mechanism.

Although there is much support for the shallow donor- V_{Ga} model, it cannot account for all of the experimental results. According to this model, the presence of carbon is only coincidental to YL. However, the large body of evidence linking the YL intensity with carbon concentration [45-47,51-55] seems unlikely to be a coincidence. Additionally, strong YL has been reported in semi-insulating (SI) GaN [54-56]. From defect formation energy arguments the V_{Ga} concentration should be negligibly small in SI GaN [44], an apparent contradiction given the strong YL observed. Resolving this issue is of technological importance for understanding the current collapse phenomenon in GaN field-effect transistors grown on SI GaN buffer layers. Current collapse has been attributed to carbon-related deep levels of similar ionization energy as the YL [57].

Most investigators assumed there is a single mechanism for the YL band. However, there are sample-specific differences in the temperature and excitation power dependencies of the YL [46]. If two or more mechanisms were responsible for YL, these discrepancies might be accounted for. Polyakov et al. [53] suggested that two defects may be involved in YL, one of them carbon-related. The present investigation provides additional evidence supporting this suggestion, and tentatively assigns the carbon-related mechanism to interstitial carbon-related defects.

A series of $\sim 1 \mu\text{m}$ thick GaN films doped using CCl_4 as a carbon source was grown by dc plasma-

assisted molecular-beam epitaxy (MBE). The MBE growth was performed at 750°C on semi-insulating ($\sim 10^9 \Omega\text{-cm}$) GaN templates grown on c-plane sapphire by metalorganic vapor phase epitaxy (MOVPE). Further details have been reported previously [55]. The dislocation density estimated by asymmetric x-ray rocking curves is in the mid 10^9 cm^{-2} . Table I summarizes the secondary ion mass spectroscopy impurity concentrations of relevant impurities.

Fig. 3.1 shows photoluminescence spectra at 12 K for a reference layer of free electron concentration $8 \times 10^{16} \text{ cm}^{-3}$ (dashed line) and a representative SI GaN:C film of resistivity $10^7 \Omega\text{-cm}$ (solid line). Luminescence was excited by a 325 nm laser with a power density of 20 W/cm^2 . The spectra were corrected for the wavelength-sensitivity dependence of the optical system. The two samples were measured under identical conditions to ensure an accurate comparison of the absolute luminescence intensities. Note that the data in Fig. 3.1 are presented with the *same* arbitrary units (not normalized).

Table I. Impurity levels in GaN:C and reference samples (cm^{-3})

Sample	[C]	[O]	[Si]	[Cl]	[H]
reference	6×10^{16}	4×10^{16}	2×10^{17}	$< 2 \times 10^{15}$	3×10^{17}
GaN:C	2×10^{18}	3×10^{17}	2×10^{16}	3×10^{15}	2×10^{17}

The most significant qualitative difference between the spectra is the appearance of a blue ($\sim 2.85 \text{ eV}$) emission band in GaN:C replacing the shallow donor-acceptor pair (DAP) emission (3.27 eV zero-phonon line) normally observed in n-type layers. Similar findings were reported in cathodoluminescence of carbon-contaminated MOVPE GaN [54]. Carbon doping also significantly reduces the total luminescence intensity. Despite its much lower overall luminescence efficiency, the GaN:C layer actually shows stronger *absolute* integrated YL intensity compared to the reference layer. This is clear evidence that carbon does in fact enhance YL. If the relationship were merely coincidental, the observed absolute YL intensity should be lower in the carbon-doped sample, not *higher*.

The next question is whether the deep level involved in YL in n-type GaN (presumably V_{Ga}) is also responsible for YL in SI GaN:C. This argument is refuted by the results of PAS (Fig. 3.2). Monoenergetic positrons were implanted at a depth up to $1 \mu\text{m}$ from the surface. The Doppler broadening of the 511 keV annihilation radiation was recorded using a Ge detector and a stabilized multichannel analyzer system. The shape of the 511 keV line was described using the low and high annihilation momentum parameters S and W [58]. When positrons annihilate at vacancies, the S-parameter increases and the W-parameter decreases, because of the smaller fraction of annihilation with high-momentum core electrons.

In Fig. 3.2 the data for SI GaN:C coincide with the S parameter for GaN without positron trapping at vacancies (measured in a p-type GaN:Mg standard sample). Thus, the V_{Ga} concentration in the carbon-doped films is below the detection limit ($< 10^{16} \text{ cm}^{-3}$) [59]. In contrast, the n-type reference film shows an increased S-parameter indicating that about 70% of the implanted positrons annihilate at vacancies. The vacancies were identified as V_{Ga} by studying the linearity of a plot of the S parameter vs. the W parameter, as described in ref. 1. From the S parameter, the V_{Ga} concentration in the MBE layer without carbon doping was estimated to be in the low 10^{17} cm^{-3} range.

Referring back to Fig. 3.1, the V_{Ga} concentration of the GaN:C layer is more than 10 times lower than that of the reference film, yet the former layer shows a higher absolute integrated YL intensity. The most likely explanation is that shallow donor- V_{Ga} recombination is not the only mechanism for YL in GaN, and a carbon-related mechanism also exists. In other words, a transition involving carbon deep levels happens to have approximately the same luminescence energy as the V_{Ga} transition believed to cause YL in n-GaN.

Concerning the microscopic nature of the proposed carbon deep level involved, the recent first-principle calculations of Wright [59] indicate that interstitial carbon-related defects have levels suitable to produce YL. For example, the carbon split interstitial is predicted to introduce levels approximately 1.6 and 2.3 eV above the valence band maximum, and the levels calculated for the complex ($C_{\text{I}}\text{-}C_{\text{N}}$) involving a channel interstitial are of similar energy. Interstitials are thermodynamically unfavorable in n-GaN, but might be incorporated kinetically in significant concentrations. For example, if carbon pairs are adsorbed at the growth surface and there is a large kinetic barrier for pair dissociation, thermodynamically unfavorable

defects such as the (C_I-C_N) channel interstitial complex may be "frozen-in" to the material.

This suggestion is supported by the work of Ishibashi et al. [52] who actually proposed interstitial carbon as the defect responsible for YL based on their experimental results. These authors compared carbon-contaminated MOVPE-GaN grown using triethylgallium (TEG) and trimethylgallium (TMG) precursors, and observed stronger YL in films grown with TEG. As TEG contains carbon-carbon bonds whereas TMG does not, a higher concentration of interstitial carbon complexes might be expected with the TEG precursor, in agreement with the higher YL intensity.

We carried out high-temperature photoluminescence measurements (Fig. 3.3) to test the hypothesis that a carbon-related deep level (rather than V_{Ga}) is related to YL in GaN:C. The integrated YL intensity values were determined by single-Gaussian curve fits. The temperature shift of the band-edge peak was used to confirm the thermocouple readings and the value obtained for dE_g/dT was 6×10^{-4} eV/K, in agreement with the results of Young and Brillson [60].

In Fig. 3.3, pronounced quenching of the luminescence intensity begins above 500 K. The quenching of the YL is caused by thermal ionization of carriers trapped on the deep levels responsible. At higher temperatures the data lie on straight lines as expected. Very different ionization energies are found for GaN:C ((1040 ± 60) meV) and the MBE reference sample ((650 ± 30) meV).

The energy of 650 meV for the reference sample differs from the 800-850 meV value for V_{Ga} determined by optical deep-level transient spectroscopy (DLTS) and related techniques [61,62]. However, different results are expected for steady-state (luminescence) and transient measurements if the deep-level capture cross-section is a function of temperature. An Arrhenius plot from DLTS has the slope $(\Delta H_V + E_b)$, where ΔH_V is the defect enthalpy with respect to the valence band and E_b is the activation energy of the capture cross-section [63]. It can be shown from detailed balance equations [64] that the activation energy obtained from luminescence quenching is closer to the true value for ΔH_V . An additional contribution to the difference in ionization energies might come from the reduction in the energy gap for higher-temperature measurements. The YL band redshifts noticeably with temperature, but to a lesser extent than the band edge peak. Additional absorption measurements are needed to discern the temperature dependence of the V_{Ga} level relative to the valence band maximum.

The defect activation energy of 1040 meV observed in SI GaN:C is larger than previously reported by Ogino and Aoki, who obtained an ionization energy of (860 ± 40) meV for the YL quenching in GaN:C [45]. However their crystals were n-type, had significant Si and O as well as C contamination, and thus likely contained significant concentrations of V_{Ga} . The ionization energy of 860 meV (between the 650 meV and 1040 meV limits of this work) could indicate that both carbon deep levels and V_{Ga} were involved in the YL mechanism for the samples of Ogino and Aoki.

Reshchikov and Korotkov [65] also studied thermal quenching of the YL in several nominally undoped n-type MOVPE-GaN layers. They found a range of ionization energies from 755 to 888 meV. Since MOVPE-GaN usually contains carbon contamination (up to the mid 10^{17} cm⁻³), a possible explanation for the observed variation might be differences in the concentrations of V_{Ga} and carbon defects participating in the YL in different samples. That is, V_{Ga} tended to dominate the YL in films with lower ionization energies whereas carbon had a significant influence in films with higher ionization energies.

The highest resistivity (10^7 Ω -cm) was found for [C] in the low 10^{18} cm⁻³ range (Fig. 3.4). The resistivity decreased for heavier doping. The temperature dependence of the resistivity suggests the conduction is governed by a grain-boundary controlled transport (GBCT) model. It appears that carbon acceptors only partially compensate the residual donors, and potential barriers formed at structural defects (dislocations and grain boundaries) might play a key role in the semi-insulating behavior.

Photoluminescence showed donor-bound and free exciton peaks (not acceptor-bound), indicating that the majority of C_N acceptors exist in the form of nearest neighbor donor-acceptor pair defects. The emission energy of an experimentally observed blue (2.9 eV) defect band associated with carbon closely matched the theoretically predicted energy of a $C_{Ga}-C_N$ donor-acceptor pair luminescence transition. Thus the $C_{Ga}-C_N$ pair (formed on the growth surface) is most likely the acceptor-deactivating defect.

The luminescence analysis combined with application of the GBCT model showed that the net donor concentration is actually higher in heavily C-doped films, and the decreased resistivity is completely unrelated to p-type conduction. Formation of electrically inactive pair defects on the growth surface is statistically more likely for higher doping levels, so the concentration of uncompensated residual donors

should indeed be higher in films with [C] in the 10^{19} cm^{-3} range compared with [C] in the 10^{18} cm^{-3} range.

In conclusion, the high absolute YL intensities observed in GaN:C films of low V_{Ga} concentration (as determined by PAS) indicate that there is indeed a causal relationship between carbon and YL. Markedly different ionization energies were found for thermal quenching of the YL in SI GaN:C and n-type reference layers. These findings support the hypothesis that interstitial carbon-related defects cause YL in GaN:C, while V_{Ga} is responsible for YL in GaN of low carbon concentration. The thermal ionization energy of V_{Ga} at 650K is near 650 meV, and that of the carbon-related deep level at 550K is near 1040 meV. The dominant YL defect can be identified from the thermal quenching of the photoluminescence at elevated temperatures. The lower resistivity in more heavily C-doped GaN can be well explained. Because of the rather large concentration of doping-related defects and a simultaneously suppressed native defect concentration it is unlikely that noise measurements in C-doped GaN will reveal a V_{Ga} -related generation-recombination signal. (see also chapt. 5.4.)

4. A new hydrogenic donor in electron-irradiated GaN

For many years, the hydrogenic donor level formed by the nitrogen vacancy (V_{N}) was thought to account for the n-type conductivity of unintentionally doped GaN [66]. However, this was ruled out by first-principles calculations that revealed isolated V_{N} to have a high formation energy in n-type GaN [67]. Hydrostatic pressure experiments showing the shallow oxygen donor level to get deep and comparison of carrier concentration and oxygen contamination levels gave strong support for oxygen to be the dominant shallow donor in 'undoped' n-GaN [68]. Subsequently, the question of the theoretically predicted shallow V_{N} donor level was never solved. We investigated the effect of 0.42-MeV electron irradiation on the excitonic luminescence of high-quality GaN grown at Samsung. Details for this investigation will be reported for the AFOSR project (MURI), Grant No. F49620-99-1-0289. The low-energy irradiation generates damage exclusively in the N-sublattice. Using high-resolution time-resolved photoluminescence (TR-PL), new bound-exciton lines from a hydrogenic donor with a binding energy of 25 meV are found after irradiation (Fig. 4.1). V_{N} is suggested to be the most likely origin of this new hydrogenic donor. The bound-exciton localization energy and lifetime were discussed in conjunction with the values observed for O_{N} and Si_{Ga} in the same sample. In addition, a metastable behavior related with the damage-induced defects was observed and tentatively explained in the framework of non-radiative defect complexes involving N_i .

The Samsung GaN which has a low as-grown defect density is after electron irradiation a promising candidate to study low-frequency noise of a native defect in GaN. It is our first choice of a material which might reveal a V_{N} -related generation-recombination noise signal.

5. Low Frequency Noise Measurements for Defect Characterization

Low-frequency electrical noise measurements can be a useful tool for the characterization of point defects in semiconductor materials and devices. As device dimensions decrease, the noise introduced by trapping-detrapping of carriers at deep defects becomes increasingly important. The advantages of the technique include the possibility of measuring fully processed device structures and the direct relevance of the measured noise levels to device performance. It is often the goal to reduce the noise level, which is only possible by the correct identification of noise sources. However, difficulties arise in the interpretation of often-indistinct noise spectrum features. Recent work on the analysis of low frequency noise in GaAs-on-insulator structures will be reviewed. The identification of an arsenic-antisite-related low-frequency noise component in GOI MESFETs with an oxidized AlAs layer will be shown in chapter 5.3. A first evaluation of C-doped GaN is described in chapter 5.4. A series of AlGaN/GaN HEMTs, with varying aluminum content and processed at UC Berkeley, was investigated as well. Results are summarized in chapt. 5.5.

5.1 Noise measurement system: Setup, signal calibration and analysis

Figure 5.1 shows the low frequency measurement setup that was acquired with support through an AFOSR DURIP grant (F49620-01-1-0285). The configuration is as supplied by Celestry Design Technologies (CDT). The system uses an HP4145 Semiconductor Parameter Analyzer to supply a constant bias voltage (or bias current). Noise is removed from the input using simple RC filters. Following the filter resistor is another selectable resistor, R_d . This is the load resistor that is used to generate the noise signal. The value of the load resistor is automatically selected based on the measured device conductance. The device under test (DUT) is mounted in a dark box or vibration -isolated variable temperature (-65 °C - 200 °C) probe station. The terminals marked G/B and Bulk are not used in this experiment so they may be ignored. The noise signal is picked up at the D/C terminal and the ac component is delivered to either a voltage preamplifier or a current preamplifier through a dc blocking capacitor. Typically the voltage amplifier was used because of the low device output resistance. The amplifiers are powered by large rechargeable lead-acid batteries to minimize the excess input noise. The preamplifier output is fed into a voltage amplifier with a gain of 25, giving a total amplification factor of 500x. The final output signal is fed to a HP 67730 Dynamic Signal Analyzer. All equipment and communication is controlled by computer and allows the direct calculation of the DUT noise power, including correction for the thermal shot noise contributed by the load and filter resistors. The typical noise floor is 10^{-24} - 10^{-23} A²/Hz through the whole range from 1 Hz to 102.4 kHz.

Figure 5.2 shows selected spectra taken on a diode fabricated from heavily irradiated ($2 \cdot 10^{14}$ cm⁻² dose of 55 MeV protons) silicon. This material is known to contain concentrations of the silicon divacancy on the order of 10^{14} cm⁻³, and the concentration of residual shallow donors is known to be on the order of 10^{12} cm⁻³. This serves as an excellent example of determining the defect energy in a material dominated by a single deep level. The silicon divacancy is well known to have a energy level at $E_c - 0.43$ eV. To emphasize the presence of a peak in the data, the usual spectrum of current noise per bandwidth (in A²/Hz) is multiplied by the frequency and divided by the dc forward bias current. The peak position clearly shifts to the right at higher measurement temperatures. This results from more rapid carrier detrapping as the temperature increases. By fitting a Lorentzian spectrum (solid line), a corner frequency can be determined. The inset shows the variation in the corner frequency with temperature giving an activation energy of 0.43 eV, exactly matching the known value. Measurements at a range of currents have shown that the corner frequency has a very slight shift with increasing current, suggesting it will be possible to extract information regarding hole capture rates and field-enhanced emission. The determination of the total concentration of silicon divacancies is complicated in this sample because the sample structure involves a p-i-n diode instead of a simple resistor. This means that there will be electron concentration gradients through the intrinsic layer. The magnitude of the trap noise depends on the local electron concentration, so the total trap noise is a summation of the total noise emitted at each point in the sample volume. In a uniform resistor, this problem will not be encountered.

The field of noise measurements is quite mature and is the subject of a large amount of literature. Most of these works focus on either device noise performance from the engineering end, or noise sources and models from the physics and mathematical end. A comparatively small amount of literature has dealt

with the measurement of point defects and their properties from low frequency noise measurements (LFNM). As device sizes are reduced, however, the noise due to traps takes on increased importance. At the same time measurements of traps in these ultra-small structures by standard techniques like deep level transient spectroscopy (DLTS) and its variants becomes more difficult. In view of these trends, the use of LFNM for defect analysis is reviewed. The application of LFNM to a particular structure (GaAs-on-insulator (GOI) MESFETs) for which DLTS is difficult is demonstrated in chapter 5.3.

The low frequency noise present in common semiconductor devices can be divided into three types: white, $1/f$, and generation-recombination (g-r) noise. These noise types will be briefly introduced to explain their role in LFNM. Details regarding derivations and more complex systems can be found e.g. in [69,70].

White noise has a uniform distribution of noise power across the frequency band of interest. By integrating the noise power spectrum, it is clear that white noise cannot extend with constant power to infinite frequency, but must instead have a roll-off beginning at some corner frequency. For shot noise and thermal noise, the two primary sources of white noise, this corner frequency lies in the gigahertz range, well above the standard 0.1-1 MHz upper bound to low frequency noise measurements. It must be noted that shallow traps can cause generation-recombination noise (discussed below) with a corner frequency above 1 MHz, giving the appearance of white noise in the low frequency range. High-quality precision resistors serve as excellent sources of white noise that can be used to calibrate noise measurement systems. The relevant current noise power S_I generated is related to resistance R , the temperature T , and current I :

$$\text{thermal noise : } S_I = 4kTR \quad (5.1)$$

$$\text{shot noise : } S_I = 2qI \quad (5.2)$$

where k is Boltzmann's constant. The temperature- and current-dependence of the observed noise allows a simple determination of the dominant noise source.

Flicker noise, or $1/f$ noise, is often a major component of low frequency noise and may obscure the generation-recombination noise spectrum of interest. As the name implies the $1/f$ noise power is inversely proportional to the frequency. There are numerous proposed sources of $1/f$ noise [71], but the structure-less nature of the spectrum often makes it difficult to identify the mechanism responsible. In devices, likely sources of $1/f$ noise are surfaces and interfaces where a band of states may exist. The overlapping generation-recombination spectra from these states, which have a wide range of different time constants, appear like a featureless $1/f$ spectrum. Therefore, devices with well-controlled surfaces bounding the current path (e.g. gated devices) have the best chance for showing noise due to bulk traps.

Generation-recombination noise is the noise type that will be emphasized in this paper as it is of the most interest to materials science. It is important to note that the term generation-recombination does not imply the usual sense of band-to-band processes. Instead, the recombination process indicated is the capture of a carrier from a band and conversely generation is the emission of a carrier from a trap back into that band. For simplicity, only mono-polar devices will be considered. When both electrons and holes play a significant role in the device operation, noise analysis is greatly complicated because processes like electron-hole recombination through trap levels must be analyzed, and the electron and hole concentrations in bipolar devices often vary by orders of magnitude over small dimensions. In the mono-polar case and neglecting any fluctuation in the mobility, a resistor has a fluctuating resistance depending only on the fluctuation in the carrier concentration. Considering a single set of traps, in an n-type semiconductor, the carrier concentration fluctuation depends on the exchange of electrons between the conduction band and the trap level. The differential equation describing the concentration of electrons in the conduction band n comprises a term representing the capture of electrons into traps and a term representing their re-emission:

$$\frac{dn}{dt} = -v_{th}\sigma(N_T - n_T)n + Ae^{-E_A/kT}n_T \quad (5.3)$$

where v_{th} is the thermal velocity, σ is the capture cross section, N_T is the total trap density, n_T is the filled trap density, A is a prefactor term representing an escape attempt rate (s^{-1}) and E_A is the activation energy for removing the electron from the trap. In equilibrium, $dn/dt=0$. This equality only applies over a time average; electrons are continually exchanged between the conduction band and the trap states. The capture and emission processes establish two time scales - a capture time constant τ_c and an emission time constant τ_e :

$$1/\tau_c = v_{th}\sigma(N_T - n_T) \quad (5.4)$$

$$1/\tau_e = Ae^{-E_A/kT} \quad (5.5)$$

To solve Equation (5.1) a single time constant is introduced: $1/\tau = 1/\tau_c + 1/\tau_e$. The solution for the carrier concentration as function of time is a simple exponential. To obtain the power spectrum the Fourier transform is taken. The determination of the magnitude of the spectrum accounts for the noise contribution of each individual trap. The derivation is somewhat complex requiring the evaluation of the expectation value of the standard deviation of the filled trap density. In the interest of space the result for the current noise power spectral density S_I will be taken from [72]:

$$\frac{S_I}{I^2} = \frac{2\tau}{n^2V} \frac{n_T(N_T - n_T)}{N_T} \frac{1}{1 + (2\pi f\tau)^2} \quad (5.6)$$

where V is the volume of the device. Two important observations can be made with this equation. First, the smaller the device volume, the larger the g-r noise power for a given current I . Therefore, reduced device sizes give more sensitive g-r noise measurements. Second, the noise is a maximum when the traps are half full; when the trap energy is far from the Fermi level the g-r noise is reduced.

In devices such as MESFETs the channel is relatively highly doped so that the Fermi level is near the conduction band. Then almost all traps are filled ($N_T \sim n_T$), and the capture time constant τ_c is very long. Therefore the emission time constant τ_e determines τ and a standard Arrhenius plot allows the determination of E_A in analogy to DLTS. Similarly, the y-intercept of the Arrhenius plot allows to estimate the capture cross section because the constant A in (5.3) is related to σ through the principle of detailed balance.

The basic experimental apparatus for measuring low frequency noise is relatively simple. The device to be measured is mounted in an electro-magnetically shielded environment, such as a metal-enclosed probe station with a single, low resistance ground path. The sample temperature is maintained using a thermoelectric chuck. Care must be taken to allow the temperature to stabilize before measurement because relative motion of the probes and the sample during measurement due to different thermal expansions as the temperature changes can result in spurious noise signals. Bias is supplied to the device using an RC lowpass filter ($RC = 10$ s) applied to the outputs of an HP4145 Parameter Analyzer. For the noise signal to be measured (e.g., the drain current noise of a MESFET), a load resistor is placed between the device terminal of interest and the bias supply. The signal at the device terminal is fed into a JFET preamplifier with the dc component removed using a blocking capacitor so that only the noise signal remains. The preamplifier is battery powered. The amplified noise signal is fed to a dynamic signal analyzer (HP 35670A), which returns the power spectrum of the noise signal. Using a computer with control software (BTA (now Celestry, Inc.) *NoisePro*), the device noise power is determined accounting for the load resistor value and the amplifier response.

5.2 First results in III-V compounds

Drain current noise measurements were performed on irradiated GOI MESFETs to study the radiation hardness of this device structure. The irradiation was a 55 MeV proton dose of $5.4 \cdot 10^{12} \text{ cm}^{-2}$. The device structure was a layer of $0.2 \mu\text{m}$ GaAs with a silicon concentration of 10^{17} cm^{-3} , deposited above a 50 nm AlAs oxidation layer. The ohmic contact was optimized using an InAs contact layer and self-aligned gate processing to reduce parasitic series resistances. The gate width and length were 300 and $3.5 \mu\text{m}$, respectively. Figure 5.3 shows the noise spectrum obtained at 4 measurement temperatures. The noise intensity has been multiplied by the measurement frequency to turn the $1/f$ background into a constant baseline. At each temperature a single well-defined Lorentzian is apparent, as shown by the best fit lines. These fits are used to determine the peak frequency, which corresponds to a carrier trapping-detrapping time constant. Figure 5.4 plots this time constant in an Arrhenius fashion to yield an activation energy of 0.79 eV. This time constant agrees well with the energy of the midgap (0/+) arsenic antisite level. The presence of arsenic antisites was expected as a result of the proton irradiation. This experiment

demonstrates well the ability of noise measurements to identify deep levels in GaAs and allows to conclude that the As_{Ga} defect is a dominant noise source in irradiated GaAs.

Figure 5.5 shows the first measurement of the low frequency noise in a LT-GaAs resistor. The film was 1.5 microns thick, grown at 250 °C with doping of $5 \times 10^{18} \text{ cm}^{-3}$ beryllium. Under these conditions the Fermi level should lie near midgap and there should be few doubly charged antisites. There is $1/f$ behavior at high frequencies. This translates into the flat background. At low frequencies, a steep increase in the noise is seen. This could be the onset of the low noise from the midgap antisite level. This measurement was taken at 150 °C, so the relatively slow response of these traps matches such a deep level. However, it was impossible to extract an activation energy because the peak did not shift to high enough frequencies at 200 °C to observe a well defined corner frequency. At lower temperatures, only a $1/f$ background is seen. Measurements on p-type LT-GaAs should show a peak at lower temperatures because the energy difference between the valence band and the antisite double donor level is smaller.

5.3 GOI-based devices

Lateral selective wet-oxidation of buried high aluminum content $\text{Al}_x\text{Ga}_{1-x}\text{As}$ layers has seen widespread application in electrical and optical devices. The oxidized layer is used to provide current confinement and a low refractive index layer in Bragg mirror stacks for vertical-cavity surface emitting lasers [73,474], and to serve as a current confining layer in heterojunction bipolar transistors [75]. Another use of this oxidation technique is to form an insulating buffer layer underneath the active channel of metal-semiconductor field effect transistors (MESFETs) [76], so-called GaAs-On-Insulator (GOI) MESFETs. Recently, a use of an oxidized AlAs buffer layer as a compliant substrate for III-nitride growth was discussed within this project. A major concern is that the oxidation procedure can cause defect injection into adjacent layers or at its interfaces. In particular, carrying out the oxidation longer than needed to achieve full lateral oxidation of the AlGaAs layer (over-oxidation) is found to have deleterious effects on device performance [77]. Many characterization techniques have been applied to study the oxide microstructure and the GaAs/oxide interface structure, for example transmission electron microscopy (TEM) [78]. It has been shown by time-resolved photoluminescence that the interface recombination rate was greatly increased after oxidation [79]. The interface recombination velocity was estimated using the light-beam induced current technique [80]. To date, no direct comparison between the parameters of the oxidation and the formation of specific recombination centers has been reported.

GOI MESFETs were designed and fabricated by applying lateral oxidation to a conventional GaAs FET design. The device structure was grown by MBE on a (100) semi-insulating GaAs substrate and consists of a 75-nm AlAs oxidation layer followed by a 250-nm GaAs channel. The channel was doped with $2 \times 10^{17} \text{ cm}^{-3}$ silicon. The structure was capped with a 5-nm $\text{Al}_{0.3}\text{Ga}_{0.7}\text{As}$ gate recess etch-stop layer and a highly doped ($n > 10^{18} \text{ cm}^{-3}$) graded InAs/GaAs digital alloy in order to reduce the contact resistance. No oxidation barrier layers were employed between the oxidation layer and the channel. Devices with gate widths, w_G , of 40, 100, and 300 μm were processed on the same wafer. All devices studied here have a gate length of 3.5 microns. After the mesa etch, the AlAs layer was laterally wet oxidized at 430°C in an atmosphere defined by bubbling 500 sccm nitrogen through water at 90°C. The oxidation was carried out for 80 minutes with the goal of just completely oxidizing the widest (300 μm) device. Consequently, the 40 μm gate width devices were heavily over-oxidized.

The total noise-power spectrum can be broken down into the following sum:

$$S_I(f) = C + A/f + \sum_i L_i / \left(1 + (f/f_{c,i})^2\right). \quad (5.7)$$

Here, $f_{c,i}$ and L_i are the Lorentzian g-r noise corner frequency and amplitude for the i^{th} trap level. C and A indicate the amplitude of white and $1/f$ noise components. Since $1/f$ noise is usually a major component of the observed noise spectrum, the spectral power density is plotted here as $S_I(f) \times f$ vs. f to reveal g-r noise as peaks. The amplitude L of the Lorentzian component can be expressed as [81]:

$$L \propto I^2 \tau D / n^2 V \quad (5.8)$$

where D is the density of the trap levels, τ , equal to $1/2\pi f_c$, is the characteristic time constant, n is the carrier density, and V is the sampled volume. For traps located more than a few kT (k is Boltzmann's

constant) below the Fermi level, the characteristic time constant is determined by the emission rate of the traps.

Several noise power spectra revealing a clear Lorentzian noise component under various experimental conditions are shown in Fig. 5.6. The applied drain voltage was chosen in the ohmic, linear region of the MESFET device characteristics in order to ensure a resistor-like behavior with nearly uniform semiconductor cross-sectional area under the gate. Fig. 5.6(c) shows that at 375K the signal was only observable in the 40 μm and 100 μm gate widths, that is, only when over-oxidation had taken place.

In-depth analysis of the corresponding trap was achieved by least-squares fits of Eq. (5.7) to the experimental data (solid lines in Fig. 5.6). In Fig. 5.6(a), the corner frequency increases as the thermal emission rate increases with temperature. The time constant τ times T^2 is plotted in Fig. 5.7 to extract the energy level of the trap using the expression $\tau = c T^2 \exp(E_A/kT)$, where c is a constant, and E_A is the activation energy. While the Lorentzian noise signature featured in Fig. 5.6 is due to a g-r level at $E_c-0.69$ eV, additional levels at $E_c-0.47$ and $E_c-0.32$ eV were observed under different gate bias conditions in a typical 100 μm gate-width device, as indicated in Fig. 5.7. The trap energies were found to be independent of the applied drain voltage. The level at $E_c-0.47$ eV appeared only at larger gate biases while the level at $E_c-0.32$ eV appeared at gate biases below the threshold voltage. $E_c-0.47$ eV may be related to a surface conduction processes [82]. The predominating near mid-gap trap at $E_c-0.69$ eV was detected under all gate biases.

The depth distribution of the $E_c-0.69$ defect was probed by analyzing the gate-voltage dependence of the Lorentzian-noise signal magnitude, Fig. 5.6(b). A normalization motivated by Eqn. (5.8) was applied in order to separate out the trap concentration: the spectral density was normalized with the square of the current and multiplied by the active volume. Here, the active volume is assumed to be the undepleted channel thickness, which was obtained from capacitance-voltage measurements. Fig. 5.8 shows that, based on this normalization, the average trap concentration is found to increase with reverse gate bias. This is expected if the trap observed is not uniformly distributed but instead increases in concentration towards the oxide interface. It is noted here that there are large uncertainties in the assignment of numerical values to the density of traps in the MESFET structure because the noise power depends on the square of the current density, which varies significantly within the device structure. Moreover, it was assumed that the main g-r noise mechanism is due to the trapping/de-trapping in the MESFET channel. However, charge fluctuations in the space charge region causing fluctuations of the conducting channel thickness will lead to equivalent noise spectra [83]. It is therefore hard to distinguish between these mechanisms, but the conclusion that the mid-gap trap is more concentrated close to the interface holds in either case. In addition, it is still possible to state that the density of the mid-gap trap is higher in the 40- μm than the 100- μm wide devices compared in Fig. 5.8. This is consistent with the above finding that the signal is undetectable in the 300 μm device. These observations qualitatively support the assignment of the trap to an oxidation-induced defect injected from the interface. Further, the results imply that the introduction of the mid-gap state depends on the over-oxidation time rather than the total oxidation time. That means that the trap is introduced efficiently only after the entire layer has been oxidized, providing an important clue regarding its microscopic origin.

The observed near mid-gap level is tentatively identified by way of the similar values of the energy level and the cross section as the level EB4 (also referred to as E4); the emission characteristics of this electron trap are shown in Fig. 5.7 by the dashed line and fit the g-r noise data well. The trap was first observed in 1 MeV electron-irradiated GaAs [84]. EB4 has also been observed in non-irradiated GaAs, e.g. in GaAs grown by molecular-beam epitaxy (MBE) at low temperature (380-400°C) [85,86]. EB4 is generally assumed to be due to a complex of the arsenic-antisite (As_{Ga}) and another defect that is not an intentional n-type doping impurity. Electron paramagnetic resonance studies of the arsenic-antisite arsenic-vacancy ($\text{As}_{\text{Ga}}-\text{V}_{\text{As}}$) complex have speculated that EB4 could arise from an electronic transition of $\text{As}_{\text{Ga}}-\text{V}_{\text{As}}$ [87]. This assignment would be in agreement with calculations of the thermal emission rate of such a complex [88].

During lateral wet-oxidation of AlAs As-rich conditions are realized in the neighboring GaAs, as evidenced by TEM [78] observations of arsenic precipitates in the vicinity of the oxide interface. A possible cause could be found in the *oxidation of GaAs* after the AlAs is consumed. Defects related to As_i , V_{Ga} , As_{Ga} , and complexes thereof, would be expected to dominate under such conditions. An assignment of the EB4 level to $\text{As}_{\text{Ga}}-\text{V}_{\text{As}}$, which could possibly result from the conversion $\text{V}_{\text{Ga}} \leftrightarrow \text{As}_{\text{Ga}}-\text{V}_{\text{As}}$ predicted by the amphoteric defect model [89], would provide a possible mechanism for the introduction of EB4 in GOI MESFETs.

In conclusion, low-frequency generation-recombination noise has been studied in GOI MESFETs for different over-oxidation conditions. Three clear defect levels were found, and one ($E_c-0.69$ eV) was identified with a previously reported As_{Ga} -related defect (EB4). This defect appeared after the AlAs layer has been fully oxidized. The spatial distribution was shown to increase towards the oxide interface, suggesting that this defect is introduced into the channel as a result of the oxidation process.

5.4 Carbon-doped GaN

In MBE grown p-doped GaN epilayers a distinct yellow luminescence signal was found which increased with the carbon doping. Because the yellow luminescence was believed to be always associated with native defects, namely gallium vacancies, V_{Ga} , some growth runs were done with varying doping concentrations, accompanied by positron annihilation spectroscopy (PAS) to determine the concentration of V_{Ga} . Also, a few tests with carbon-doped GaN, co-doped with silicon, were initiated. Astonishingly, these wafers were n-conductive. The carbon, commonly an acceptor in GaN, could not compensate the silicon donors. The PAS analysis showed that the materials yellow luminescence did not correlate with the concentration of gallium vacancies. The formation of gallium vacancies was largely suppressed with increasing carbon doping (for details see chapt. 3). Noise measurements in combination with temperature dependent noise spectroscopy was applied to determine the activation energy of the dominant noise trap in this material.

The results show a generation-recombination noise which is independent of the applied bias. The temperature dependent spectroscopy in Figure 5.9 gives the signature of a deep level which is located at 0.6 eV below the conduction band (result of the activation energy plotted in Figure 5.10). This defect is only observed in silicon co-doped films and might be due to a complex containing Si. The noise signal in only carbon-doped GaN did not show a clear generation-recombination part, or the temperature dependent noise could not be correlated to one activation energy. Thus, only in silicon co-doped samples a *dominant* defect causing g-r noise could be found. However, additional defect characterization is necessary to unambiguously identify this defect.

5.5 AlGaN / GaN HEMTs

A strong polarization facilitates the electron transfer from $Al_xGa_{1-x}N$ layer to the triangular quantum well at $Al_xGa_{1-x}N$ / GaN interface and brings in a high sheet charge density even without intentional doping in the $Al_xGa_{1-x}N$ layer [90]. Theoretically, the higher the Al content, x , is, the higher the induced spontaneous and piezoelectric polarization. However, the increasing percentage of Al in the $Al_xGa_{1-x}N$ layer causes relaxation [91] and decreasing 2DEG mobility due to long-range scattering (alloy disorder scattering or interface roughness) [92] and will start to tradeoff the advantage of high Al content in $Al_xGa_{1-x}N$. Therefore an optimum Al composition is crucial for a HEMT performance. In Fig. 5.11 an optimum Al composition region for high induced sheet concentration was predicted by Ambacher et. al. [91] to be around 30% -35% without epitaxial layer relaxation. It is therefore of special interest to investigate the AlGaN/GaN HEMT in this Al composition range.

MOCVD grown HEMT structures were provided by Emcore Corporation. The structures consist of 1.5 μm unintentionally doped GaN grown on sapphire, followed by ~ 25 nm of $Al_xGa_{1-x}N$. The Al composition, x , was varied between 28% and 35% to assess the impact of Al composition on 2DEG transport properties and the device performance. The HEMTs were fabricated by a 4-step process: dry-etch mesa isolation, ohmic contact metallization, ohmic contact annealing, and gate metallization. Briefly stated, the mesa isolation was performed by argon ion-milling. Ti/Al/Ni/Au ohmic metallization was deposited by e-beam evaporation and patterned by lift-off. A contact resistance of $5 \times 10^{-5} \Omega\text{-cm}^2$ was achieved after 900 °C annealing for 20 seconds. A Schottky gate metallization of Ni/Au was deposited by e-beam evaporation. An array of gate lengths of 2, 3.5, 5 μm and gate widths of 50, 100, and 150 μm was patterned. Shown in Fig. 5.12 is the schematic of the device structure.

First, a baseline capacitance-voltage measurement was performed on rectangular capacitors with a Schottky contact area of 21000 μm^2 . The capacitors were fabricated simultaneously with HEMTs. An HP

4277 LCR meter was used to sweep the gate bias from -8 V to 0 V. Fig. 5.13 shows the typical $C-V$ and $G-V$ curves of the AlGa_N/Ga_N structure at 1 MHz. As the charge in the channel is due to the polarization in the AlGa_N layer and tightly bound to the interface, the AlGa_N barrier thickness can be estimated by taking the capacitance at gate bias of 0 V and using a permittivity of $\epsilon_{\text{AlGa}_N(x)} = 0.3x + 10.4$ [91]. The thickness was calculated to 220 , 239 , 257 , and 288 Å, respectively, with decreasing Al compositions of 35% , 32% , 30.2% and 28% . The values are slightly thicker, yet very close to the x-ray results from the wafer supplier, which are 206 , 221 , 230 , and 267 Å, respectively. (The samples with 34% and 29% had a layer thickness of 242 and 230 Å according to the wafer supplier, they aren't included in this study.) Fig. 5.14 shows the extracted carrier concentration profile. The data shows a high carrier concentration at the AlGa_N/Ga_N heterointerface, and low buffer doping. Even though the charge in the channel is a result of polarization in AlGa_N, the peak density is not a function of the Al composition. On the contrary, the peak concentration appears to be nearly constant for the Al composition range between 28% and 35% .

Common-source DC characteristics of the fabricated HEMTs are determined by use of Cascade probe station and HP 4145B Semiconductor Parameter Analyzer. Typical transfer characteristics and drain current-voltage characteristics of an Al_xGa_{1-x}N/Ga_N HEMT are shown in Fig. 5.15 and Fig. 5.16. The Al composition, x , of the particular device is 28% . The gate width and length are 100 μm and 2 μm respectively. The maximum saturation current is about 400 mA/mm and the peak transconductance is about 110 mS/mm. The threshold voltage as determined by a linear fit on the I_d-V_g curve is about -4.2 V. Shown in Fig. 5.17 is its gate leakage current, demonstrating that in the Al_{0.28}Ga_N/Ga_N HEMT structure where the AlGa_N is the thickest (267 Å estimated by $C-V$ measurement), the isolation of the gate is satisfactory. In fact, the gate current at pinch-off ($V_{ds} = 6$ V, $V_g = -6$ V) is at least 4 orders of magnitude smaller than drain current. While the structure with the thinnest AlGa_N layer (Al= 35%) exhibits the highest gate leakage current, it is still about 2 orders of magnitude smaller than drain current. In other words, the main leakage current source is not due to gate leakage.

The Al composition dependence of DC characteristics cannot only be explained by the amount of polarization. Shown in Fig. 5.18 is the saturation drain current as a function of Al composition. The saturation current was measured under drain bias of 6 V and gate bias of 0 V. 2 μm gate length devices with different gate widths of 50 , 100 , and 150 μm were measured and the average current density and its error bar are shown. Even though the variation within each wafer is significant, a decreasing trend with increasing Al composition is still apparent. Moreover, a similar decrease of transconductance and an increase of gate leakage current with Al composition are also observed. As proposed by Keller et. al. [93], the resulting increase in strain with increasing Al content in the barrier may lead to increased roughness and reduced electron mobility at the interface. This hypothesis can describe the decreasing drain saturation current with increasing polarization.

The drain current low-frequency noise is measured in the frequency range from 1 Hz to 100 kHz at a small value of the drain-source bias (0.5 V, in the linear region of HEMT operation). The sample noise spectra S_{I_d}/I_d^2 of Al_{0.28}Ga_{0.72}N/Ga_N HEMT is presented in Fig. 5.19. The bottom curve is the relative spectral noise density of drain current fluctuations. It has the form of $1/f^r$ with r close to unity. The top curve is the bottom curve multiplied by frequency. The revealed peaks are typical for the generation-recombination (G-R) noise from local levels.

There are many different noise sources in the AlGa_N/Ga_N HEMT that may contribute to the overall $1/f$ noise. Assuming the noise sources are not correlated and considering contact noise, channel noise, and surface noise at source-gate and gate-drain region, as the dominant noise sources, the total spectral noise density has been formulated as followed [94]:

$$\frac{S_{I_d}}{I_d^2} = \frac{S_{R_{ch}}}{R_{ch}^2} \frac{R_{ch}^2}{(R_{ch} + R_s + R_c)^2} + \frac{S_{R_s}}{R_s^2} \frac{R_s^2}{(R_{ch} + R_s + R_c)^2} + \frac{S_{R_c}}{R_c^2} \frac{R_c^2}{(R_{ch} + R_s + R_c)^2} \quad (5.9)$$

Here, $S_{R_{ch}}$, S_{R_s} , and S_{R_c} are the power spectral density of channel resistance, R_{ch} , surface resistance R_s , and contact resistance R_c . At the same drain voltage, only the resistance and the power spectral density of the channel is a function of gate voltage, or a function of the drain current [94]:

$$S_{R_{ch}} = \frac{\alpha_{ch} R_{ch}^2}{N_{ch} f} \propto R_{ch}^3 \propto I_d^{-3} \quad (5.10)$$

In Eqn. (5.10), α_{ch} is the Hooges parameter of channel noise, f is the frequency and N_{ch} , which is inversely proportional to R_{ch} , is the number of carriers in the channel.

To discriminate the noise spectral density contribution between series resistance noise and channel resistance noise, one can examine the drain current dependence of the relative noise spectral density, S_{Id}/I_d . Here three extreme cases are indicated as following:

- (I) when the noise is dominated by noise sources residing in the channel and $R_c + R_s \gg R_{ch}$, Eq. (1) predicts:

$$\frac{S_{Id}}{I_d^2} \rightarrow \frac{S_{R_{ch}}}{R_{ch}^2} \frac{R_{ch}^2}{(R_c + R_s)^2} \propto R_{ch}^3 \propto I_d^{-3}$$

- (II) when the noise is dominated by noise sources residing in the channel and $R_c + R_s \ll R_{ch}$, Eq. (1) predicts:

$$\frac{S_{Id}}{I_d^2} \rightarrow \frac{S_{R_{ch}}}{R_{ch}^2} \frac{R_{ch}^2}{(R_{ch})^2} \propto R_{ch}^1 \propto I_d^{-1}$$

- (III) when the noise is dominated by noise sources in the contact and surface regions, and $R_c + R_s \gg R_{ch}$, Eq. (1) predicts:

$$\frac{S_{Id}}{I_d^2} \rightarrow \frac{S_{R_s}}{R_s^2} \frac{R_s^2}{(R_s + R_c)^2} + \frac{S_{R_c}}{R_c^2} \frac{R_c^2}{(R_s + R_c)^2} \propto R_{ch}^0 \propto I_d^0$$

As shown in Fig. 5.20 at high drain current (or small applied gate bias), the relative noise spectral density of different Al composition AlGaIn/GaN HEMT structures all exhibit a drain current dependence of power -3 . This dependence agrees with the above prediction of case (I), where the low-frequency noise is dominated by noise sources in the channel. To better understand the channel noise creation in AlGaIn/GaN HEMT structures with different Al composition in the AlGaIn barrier layers, the measured noise in the high drain current is used to extract the Hooge's parameter, $\alpha = S_I(f)N/fI^2$. Interestingly, in the Al composition range between 28% and 35%, the extracted Hooge's parameters show no clear dependence on the Al composition. Instead, Hooge's parameter of the channel rises with the AlGaIn barrier thickness as shown in Fig. 5.21. This tendency is supported by earlier investigations [95]. It was observed that within the AlGaIn/GaN system an onset to 3D growth occurred at very low thickness values which leads to a structural degradation with increasing thickness. However, the sample data obtained so far is limited and from only one material source. Future investigations using various material supplier and/or processing techniques for the AlGaIn/GaN HEMTs and also applying transmission electron microscopy may clarify whether a surface diffusion limiting process dominates over an onset of misfit dislocation formation in the presently investigated epilayers. Additionally, the role of the native defects which are assumed to be located in the AlGaIn layer [96] need to be investigated in more detail.

Another open question arises from the G-R noise investigation of the AlGaIn/GaN HEMT structure. Shown in Fig. 5.22 is the noise spectra multiplied by frequency to better reveal the G-R noise signal. As presented in the temperature interval between 300 K to 350 K, one G-R noise peak with an activation energy around 0.22 eV is observed in all AlGaIn/GaN HEMT structures with different Al compositions, from 28% to 35%. Moreover, the responsible trap exhibits field dependent noise amplitude. Fig. 5.23 shows the G-R noise amplitude as a function of applied gate bias. With increasing field, the G-R noise signal is more profound. This may indicate a variable trap distribution. A detailed model is needed to locate the origin of the responsible trap. Summarized, with low-frequency noise spectroscopy a variety of defects can be investigated which cause noise in the respective devices. The correlation of specific defect types with device performance is demonstrated in part but needs additional work. Especially, LF-noise spectroscopy at different device areas combined with local defect characterization (see for example

attachment part) is a promising approach for future defect characterization modified to enhance device performance.

6. Summary and Future work

This research project combined investigations on stoichiometry related defects in various group III – nitride materials with some on GaAs-based epilayers. New characterization tools were developed to facilitate the quantification of native defect populations. Device structures (MESFET and HEMT) were processed and tested, their performance correlated to defects or defect-related strain relaxation processes. Some common misconceptions on the nature of optical responses were detected and corrected. Controlled native defect incorporation can be achieved by electron irradiation. Native defect population control due to growth process modifications is rather challenging and needs further research.

In future, local defect characterization methods such as VEELS combined with variable bias low noise spectroscopy will provide detailed information on the dominant defects in group III – nitride devices and their local distribution. It is desirable to evaluate epitaxially grown materials and processed devices from different sources to compare a variety of different growth conditions and/or processing techniques. As vacancies in group III – nitrides are likely a cause of the materials property fluctuation, resulting in lack of device reliability (yield) and also aging effects due to enhanced diffusion, especially if devices are operated at elevated temperatures, it is vital to understand and eventually control the incorporation of those defects due to varied growth conditions and/or processing techniques.

In order to facilitate this goal it is desirable to correlate the defect population present in the III-nitride epilayers with specific, easy to measure, material properties such as conductivity or average surface roughness and/or with the performance of the respective device. Such an interdependence will not just provide the key for improved material quality but may also provide a simplified approach to identify and quantify dominant defects making future tedious and time consuming characterization methods unnecessary for the evaluation of a III-nitride based device (structure). Also, growth methods need to be developed which will improve the III-nitride material production via MBE growth. Such methods include the use of chemical surfactants, novel buffer layers or photo-assisted MBE growth. The process of AlGaIn/GaN HEMT structures will then allow for device performance tests which may be correlated to a quantified enhanced materials quality. As an ultimate goal, MBE growth of non-polar III-nitrides may be used in combination with the above described techniques to evaluate the materials applicability for a III-nitride HBT. Along with the control of native (point) defects a general reduction of extended defects needs to be achieved. It is assumed that the above described modified growth techniques will also influence the formation of extended defects, those prospective benefits will therefore also have to be investigated.

7. Personnel

Eicke.R. Weber, P.I.

Petra Specht, assistant research engineer	MBE & TEM, coordination
Robert Armitage (Ph.D. 2002)	MBE of GaN
Ri-an Zhao (Ph.D. 2002)	MBE and DRS study, Hall effect
Michael J. Cich (Ph.D. 2001)	noise measurements
Susie Tzeng, graduate student	noise measurements
Qing (Emily)Yang, graduate student	PL of C-doped GaN
Xiaoyu Xu, graduate student	TEM
Joerg Gebauer, visiting scholar, Germany	S-PAS (in Germany), MCD/NIRA
Collaborating scientist:	
Kimmo Saarinen, Helsinki, Finland	Positron Annihilation Spectroscopy of GaN:C

Five graduate students participated in the above described project, working closely together with two postdoctoral researchers and the project's PI. One Ph.D. thesis, "Growth and Defect Characterization of Low Temperature Molecular Beam Epitaxy GaAs" by Ri-An Zhao, was supported by this research grant, another one (S. Tzeng on noise analysis and noise spectroscopy in III-V compound devices) is in preparation.

The LF-Noise measurement system was obtained with a AFOSR DURIP grant, no. F49620-01-1-0285

8. References

1. K. Saarinen, T. Laine, S. Kuisma, J. Nissilä, P. Hautojärvi, L. Dobrzynski, J.M. Baranowski, K. Pakula, R. Stepniewski, M. Wojdak, A. Wyszomolek, T. Suski, M. Leszczynski, I. Grzegory, and S. Porowski, *Phys. Rev. Lett.* **79**, 3030 (1997)
2. X. Liu, A. Prasad, J. Nishio, E.R. Weber, Z. Liliental-Weber, W. Walukiewicz, *Appl. Phys. Lett.* **67**, 279 (1995)
3. S. B. Zhang and J. E. Northrup, Chemical potential dependence of defect formation energies in GaAs: application to Ga self-diffusion., *Phys. Rev. Lett.* **67**, 2339 (1991)
4. C.G. Van de Walle, J.E. Northrup, J. Neugebauer, in: *Physik Mikrostrukturierter Halbleiter 27*, eds. P. Specht, T.R. Weatherford, P. Kiesel, S. Malzer, Asilomar, Pacific Grove, CA, 2002, p. 11
5. F. W. Smith, A. R. Calawa, C. L. Chen, M. J. Manfra, and L. J. Mahoney, "New MBE buffer used to eliminate backgating in GaAs MESFETs", *IEEE Electron Device Lett.* **9**, 77 (1988).
6. Z. Liliental-Weber, H. J. Cheng, S. Gupta, J. Whitaker, K. Nichols, and F. W. Smith, "Structure and carrier lifetime in LT-GaAs", *J. Electron. Mater.* **22**, 1465 (1993).
7. M. Kaminska, Z. Liliental-Weber, E. R. Weber, T. George, J. B. Kortright, F. W. Smith, B. Y. Tsaur, and A. R. Calawa, "Structural properties of As-rich GaAs grown by molecular beam epitaxy at low temperatures", *Appl. Phys. Lett.* **54**, 1881 (1989).
8. D. C. Look, D. C. Walters, M. O. Manasreh, J. R. Sizelove, C. E. Stutz, and K. R. Evans, "Anomalous Hall effect results in low-temperature molecular-beam-epitaxial GaAs: hopping in a dense EL2-like band", *Phys. Rev. B* **42**, 3578 (1990).
9. A. C. Warren, J. M. Woodall, J. L. Freeouf, D. Grischkowsky, D. T. McInturff, M. R. Melloch, and N. Otsuka, "Arsenic precipitates and the semi-insulating properties of GaAs buffer layers grown by low-temperature molecular beam epitaxy", *Appl. Phys. Lett.* **57**, 1331 (1990)
10. M. Luysberg, H. Sohn, A. Prasad, P. Specht, Z. Liliental-Weber, E. R. Weber, J. Gebauer, and R. Krause-Rehberg, "Effects of the growth temperature and As/Ga flux ratio on the incorporation of excess As into low-temperature grown GaAs", *J. Appl. Phys.* **83**, 561 (1998)
11. A. Suda and N. Otsuka, "Arsenic flux dependence of incorporation of excess arsenic in molecular beam epitaxy of GaAs at low temperature", *Appl. Phys. Lett.* **73**, 1529 (1998)
12. P. Thompson, Y. Li, J. J. Zhou, D. L. Sato, L. Flanders, and H. P. Lee, "Diffuse reflectance spectroscopy measurement of substrate temperature and temperature transient during molecular beam epitaxy and implications of low-temperature III-V epitaxy", *Appl. Phys. Lett.* **70**, 1606 (1997)
13. Z. Liliental-Weber, W. Swider, K. M. Yu, J. B. Kortright, F. W. Smith, and A. R. Calawa, "Breakdown of crystallinity in low temperature grown GaAs layers", *Appl. Phys. Lett.* **58**, 2153 (1991).
14. G. Apostolopoulos, J. Herfort, W. Ulrici, L. Däweritz, and K. H. Ploog, "In situ reflectance-difference spectroscopy of GaAs grown at low temperatures", *Phys. Rev. B* **60**, R5145 (1999).
15. D. A. Gajewski, J. E. Guyer, and J. G. Pellegrino, "Real-time measurements of the pseudoelectric function of low-temperature-grown GaAs", *Appl. Phys. Lett.* **77**, 540 (2000).
16. T. P. Pearsall, S. R. Saban, J. Booth, B. T. Beard, Jr., and S. R. Johnson, "Precision of noninvasive temperature measurement by diffuse reflectance spectroscopy", *Rev. Sci. Instrum.* **66**, 4977 (1995).
17. M. K. Weilmeier, K. M. Colbow, T. Tiedje, T. van Buuren, and L. Xu, "A new optical temperature measurement technique for semiconductor substrates in molecular beam epitaxy", *Can. J. Phys.* **69**, 422 (1991).
18. A.S. Jordan, "Determination of the total emittance of n-type GaAs with application to Czochralski growth", *J. Appl. Phys.* **51**, 2216 (1980).

19. X. Liu, A. Prasad, W. M. Chen, A. Kurpiewski, A. Stoschek, Z. Liliental-Weber and E. R. Weber, "Mechanism responsible for the semi-insulating properties of low-temperature grown GaAs", *Appl. Phys. Lett.* **65**, 3002 (1994).
20. X. Liu, A. Prasad, J. Nishio, E. R. Weber, Z. Liliental-Weber and W. Walukiewicz, "Native point defects in low-temperature grown GaAs", *Appl. Phys. Lett.* **67**, 279 (1995).
21. G. M. Martin, "Optical assessment of the main electron trap in bulk semi-insulating GaAs", *Appl. Phys. Lett.* **39**, 747 (1981).
22. S. U. Dankowski, P. Kiesel, B. Knüpfer, M. Kneissl, G. H. Döhler, U. D. Keil, D. R. Dykaar, and R. F. Kopf, "Annealing induced refractive index and absorption changes of low-temperature grown GaAs", *Appl. Phys. Lett.* **65**, 3269 (1994).
23. S. R. Johnson, and T. Tiedje, "Temperature dependence of the Urbach edge in GaAs", *J. Appl. Phys.* **78**, 5609 (1995).
24. S. R. Johnson, C. Lavoie, M. Nissen, and T. Tiedje, US Patent No.5,388,909 (1995).
25. P. Specht, R.C. Lutz, R. Zhao, E.R. Weber, in: *Physik Mikrostrukturierter Halbleiter 6*, eds.: T. Marek, S. Malzer, P. Kiesel, Erlangen-Nuernberg 1998, p.15
26. M. Luysberg, H. Sohn, A. Prasad, P. Specht, Z. Liliental-Weber, E.R. Weber, J. Gebauer, R. Krause-Rehberg, *J. Appl. Phys.* **83**, 561 (1998)
27. R. Zhao, M.J. Cich, P. Specht, E.R. Weber, *Appl. Phys. Lett.* **80**, 2060 (2002)
28. W.K. Liu, D.I. Lubyshev, P. Specht, R. Zhao, E.R. Weber, J. Gebauer, A.J. SpringThorpe, R.W. Straeter, S. Vijarnwannaluk, W. Songprakob, R. Zallen, *J. Vac. Sci. Technol.* **B18**, 1594 (2000)
29. K.H. Wietzke, F.K. Koschnick, K. Krambock, *Appl. Phys. Lett.* **71**, 2133 (1997)
30. J. Gebauer, R. Zhao, P. Specht, E.R. Weber, F. Börner, F. Redmann, R. Krause-Rehberg, "Does Beryllium doping suppress the formation of Ga-vacancies in non-stoichiometric GaAs layers grown at low temperatures?", *Appl. Phys. Lett.* **79**, 4313 (2001)
31. J. Gebauer, F. Börner, R. Krause-Rehberg, P. Specht, E.R. Weber, "Vacancies in low-temperature-grown GaAs: Observations by positron annihilation", in: IEEE conference on semiconducting and insulating materials SIMC-X, Berkeley CA, June 1998, eds. Z. Liliental-Weber & C. Miner, (1999), p.118
32. P. Specht, R.C. Lutz, R. Zhao, E.R. Weber, "Growth and Characterization of p-doped LT-GaAs", in: *Physik Mikrostrukturierter Halbleiter 6*, eds.: T. Marek, S. Malzer, P. Kiesel, Erlangen-Nürnberg 1998, p.15
33. P. Specht, M.J. Cich, H. Sohn, E.R. Weber, "P-conductive LT-GaAs: The alternative for device applications?", in: *Physik Mikrostrukturierter Halbleiter 10*, eds.: P. Kiesel, S. Malzer, T. Marek, Erlangen-Nürnberg, 1999, p. 7
34. P. Specht, M.J. Cich, R. Zhao, J. Gebauer, M. Luysberg, E.R. Weber, "Incorporation and thermal stability of defects in highly p-conductive con-stoichiometric GaAs:Be", *Physica B* **308-310**, 808 (2001)
35. J. Lagowski, H.C. Gatos, J.M. Parsey, K. Wada, M. Kaminska, W. Walukiewicz, "Origin of the 0.82-eV electron trap in GaAs and its annihilation by shallow donors", *Appl. Phys. Lett.* **40**, 342 (1982)
36. N. Atique, E.S. Harmon, J.C.P. Chang, J.M. Woodall, M.R. Melloch, N. Otsuka, "Electrical and structural properties of Be- and Si-doped low-temperature grown GaAs", *J. Appl. Phys.* **77**, 1471 (1995)
37. M. Luysberg, P. Specht, E.R. Weber, "Influence of Be Doping on the Structural Properties of Low-Temperature grown GaAs", in: 2000 Int. Semicond. and Insulating Mat. Conference, SIMC-XI, eds.: C. Jagadish, N.J. Welham, IEEE Publ. 2001, p.81
38. W. Shan, W. Walukiewicz, J. W. Ager, III, E. E. Haller, J. F. Geisz, D. J. Friedman, J. M. Olson, and S. R. Kurtz, "Band anticrossing in GaInNAs alloys", *Phys. Rev. Lett* **82**, 1221 (1999)

39. A. Yu Egorov, D. Bernklau, D. Livshits, V. Ustinov, Zh I. Alferov, and H. Riechert, "High power CW operation of InGaAsN lasers at 1.3 μm ", *Electron Lett. (UK)* **35**, 1643 (1999); A. W. Jackson, R. L. Naone, L. M. Chirovsky, S. A. Feld, D. Galt, M. J. Dalberth, J. M. Smith, I. R. Thompson, M. D. Lange, and D. W. Kisker, "1.3- μm InGaAsN VCSELs for telecom and datacom applications", *Proc. of the SPIE*, **4533**, 12 (2001)
40. N. Q. Thinh, I. A. Buyanova, P. N. Hai, W. M. Chen, H. P. Xin, C. W. Tu, "Signature of an intrinsic point defect in $\text{GaN}_{1-x}\text{As}_x$ ", *Phys. Rev. B* **63**, 033203 (2001)
41. M. A. Pinault, E. Tournie, "Influence of alloy stability on the photoluminescence properties of GaAsN / GaAs quantum wells grown by molecular beam epitaxy", *Appl. Phys. Lett.* **79**, 3404 (2001)
42. A. E. Zhukov, R. Zhao, P. Specht, V. M. Ustinov, A. Anders, E. R. Weber, "MBE growth of (In)GaAsN on GaAs using a constricted DC plasma source", *Semiconductor Sci. and Tech.* **16**, 413 (2001)
43. X. Liu, A. Prasad, J. Nishio, E. R. Weber, Z. Liliental-Weber, and W. Walukiewicz, "Native point defects in low-temperature-grown GaAs", *Appl. Phys. Lett.* **67**, 279 (1995)
44. J. Neugebauer and C. Van de Walle, *Appl. Phys. Lett.* **69**, 503 (1996)
45. T. Ogino and M. Aoki, *Jpn. J. Appl. Phys.* **19**, 2395 (1980)
46. R. Zhang and T.F. Kuech, *Appl. Phys. Lett.* **72**, 611 (1998)
47. S.O. Kucheyev, M. Toth, M.R. Phillips, J.S. Williams, C. Jagadish, and G. Li, *J. Appl. Phys.* **91**, 5867 (2002)
48. D.M. Hofmann, D. Kovalev, G. Steude, B.K. Meyer, A. Hoffmann, L. Eckey, R. Heitz, T. Detchprom, H. Amano, and I. Akasaki, *Phys. Rev. B* **52**, 16702 (1995)
49. X. Lin, P.W. Bohn, and J.J. Coleman, *Appl. Phys. Lett.* **74**, 4049 (1999)
50. K. Kuriyama, H. Kondo, and M. Okada, *Solid State Communications* **119**, 559 (2001)
51. R. Niebuhr, K. Bachem, K. Dombrowski, M. Maier, W. Pletschen, and U. Kaufmann, *J. Electronic Materials* **24**, 1531 (1995)
52. A. Ishibashi, H. Takeishi, M. Mannoh, Y. Yabuuchi, and Y. Ban, *J. Electronic Materials* **25**, 799 (1996)
53. A.Y. Polyakov, M. Shin, J.A. Freitas, M. Skowronski, D.W. Greve, and R.G. Wilson, *J. Appl. Phys.* **80**, 6349 (1996)
54. C.H. Seager, A.F. Wright, J. Yu, and W. Götz, to appear in *J. Appl. Phys.* vol. **92** (2002)
55. R. Armitage, Q. Yang, H. Feick, Y. Park, and E.R. Weber, *Proc. Mat. Res. Soc. Symp.* **719**, F 1.2 (2002)
56. H. Tang, J.B. Webb, J.A. Bardwell, S. Raymond, J. Salzman, and C. Uzan-Saguy, *Appl. Phys. Lett.* **78**, 757 (2001)
57. P.B. Klein, S.C. Binari, K. Ikossi, A.E. Wickenden, D.D. Koleske, and R.L. Henry, *Appl. Phys. Lett.* **79**, 3529 (2001)
58. K. Saarinen, P. Hautojärvi, and C. Corbel, in *Identification of Defects in Semiconductors*, ed. M. Stavola (Academic Press, New York, 1998)
59. A.F. Wright, *J. Appl. Phys.* **92**, 2575 (2002)
60. A.P. Young and L.J. Brillson, *Appl. Phys. Lett.* **77**, 699 (2000)
61. A.Y. Polyakov, N.B. Smirnov, A.S. Usikov, A.V. Govorkov, B.V. Pushniy, *Solid State Electron.* **42**, 1959 (1998)
62. P. Muret, A. Philippe, E. Monroy, B. Beaumont, F. Omnes, P. Gibart, *J. Appl. Phys.* **91**, 2998 (2002)

63. D.K. Schroder, in: *Semiconductor Material and Device Characterization*, (John Wiley & Sons, New York, 1998), p. 316
64. C.T. Sah, L. Forbes, L.L. Rosier, A.F. Tasch, *Solid-State Electron.* **13**, 759 (1970)
65. M.A. Reshchikov, R.Y. Korotkov, *Phys. Rev. B* **64**, 115205 (2001)
66. H. P. Maruska and J. J. Tietjen, *Appl. Phys. Lett.* **15**, 327 (1969)
67. J. Neugebauer and C. G. Van de Walle, *Phys. Rev. B* **50**, 8067 (1994)
68. C. Wetzel, T. Suski, J.W. Ager III, E.R. Weber, E.E. Haller, S. Fischer, B.K. Meyer, R.J. Molnar, and P. Perlin, Pressure Induced Deep Gap State of Oxygen in GaN, *Phys. Rev. Lett.* **78**, 3923 (1997)
69. A. van der Ziel, *Noise in Solid State Devices and Circuits*, Wiley, 1986
70. A. Ambrozy, *Electronic Noise*, McGraw-Hill, 1982
71. P.H. Handel, "Quantum Approach to 1-F Noise", *Phys. Rev. A* **22**, 745 (1980)
72. J.A. Copeland, "Semiconductor Impurity Analysis from Low-Frequency Noise Spectra", *IEEE Trans. Electron Devices* **ED-18**, 50 (1971)
73. K.D. Choquette K. L. Lear, R. P. Schneider, Jr., K. M. Geib, J. J. Figiel, and R. Hull, Fabrication and performance of selectively oxidized vertical-cavity lasers. *IEEE Photonics Technology Lett.* **7** 1237 (1995)
74. J.J. Wierer P. W. Evans, N. Holonyak, Jr., and D. A. Kellogg, Lateral electron current operation of vertical cavity surface emitting lasers with buried tunnel contact hole sources. *Appl. Phys. Lett.* **71** 3468 (1997)
75. A. Massengale M. C. Larson, C. Dai, and J. S. Harris, Jr., Collector-up AlGaAs/GaAs heterojunction bipolar transistors using oxidised AIAs for current confinement. *Electronics Lett.* **32** 399 (1996)
76. P.A. Parikh, P.M. Chavarkar, U.K. Mishra, GaAs MESFET's on a truly insulating buffer layer: demonstration of the GaAs on insulator technology. *IEEE Electron Device Lett.* **18** 111 (1997)
77. C. Zheng R. Coffie, D. Buttari, J. Champlain, and U. K. Mishra, Oxidation control of GaAs pHEMTs for high efficiency applications. *Ieee Electron Device Letters* **23** 380 (2002)
78. Z. Liliental-Weber M. Li, G. S. Li, C. Chang-Hasnain, and E. R. Weber, Transmission electron microscopy of Al-rich III-V oxides. in *Proceedings of the 9th Conference on Semiconducting and Insulating Materials (SIMC'9)* (Cat. No.96CH35881) Proceedings of Semiconducting and Semi-Insulating Materials Conference. 1996. Toulouse, France: IEEE
79. J.A. Kash B. Pezeshki, F. Agahi, and N. A. Bojarczuk, Recombination in GaAs at the AIAs oxide-GaAs interface. *Appl. Phys. Lett.* **67** 2022 (1995)
80. H. Gebretsakik K. Zhang, K. Kamath, X. Zhang, and P. Bhattacharya, Recombination characteristics of minority carriers near the Al_xO_y/GaAs interface using the light beam induced current technique. *Appl. Phys. Lett.* **71** 3865 (1997)
81. J.A. Copeland, Semiconductor Impurity Analysis from Low-Frequency Noise Spectra. *IEEE Transactions on Electron Devices* **ED18** 50 (1971)
82. V.R. Balakrishnan, V. Kumr, S. Ghosh, Experimental evidence of surface conduction contributing to transconductance dispersion in GaAs MESFET's. *Ieee Transactions on Electron Devices* **44** 1060 (1997)
83. P. Lauritzen, Low-Frequency Generation Noise in Junction Field Effect Transistors. *Solid-State Electronics* **8** 41 (1965)
84. D.V. Lang, R.A. Logan, L.C. Kimerling, Identification of Defect State Associated with a Gallium Vacancy in Gaas and Alxgal-Xas. *Phys. Rev. B* **15** 4874 (1977)

85. R.A. Stall C. E. C. Wood, P. D. Kirchner, and L. F. Eastman, Growth-Parameter Dependence of Deep Levels in Molecular-Beam-Epitaxial GaAs. *Electronics Lett.* **16** 171 (1980)
86. D.C. Look Z. Q. Fang, H. Yamamoto, J. R. Sizelove, M. G. Mier, and C. E. Stutz, Deep Traps in Molecular-Beam-Epitaxial GaAs Grown at Low- Temperatures. *J. Appl. Phys.* **76** 1029 (1994)
87. H.J. VonBardeleben, J.C. Bourgoin, A. Miret, , Identification of the Arsenic-Antisite-Arsenic-Vacancy Complex in Electron-Irradiated GaAs. *Phys. Rev. B* **34** 1360 (1986)
88. S. Markram-Ebeid, P. Boher, M. Lannoo, Interactions between Bombardment-Induced Defects in GaAs. *Appl. Phys. Lett.* **50** 270 (1987)
89. N. Ky, F.K. Reinhart, Amphoteric native defect reactions in Si-doped GaAs. *J. Appl. Phys.* **83** 718 (1998)
90. L. Hsu, W. Walukiewicz, Effect of polarization fields on transport properties in AlGaIn/GaN heterostructures. *J. Appl. Phys.* **89**, 1783 (2001)
91. O. Ambacher B. Foutz, J. Smart, J. R. Shealy, N. G. Weimann, K. Chu, M. Murphy, A. J. Sierakowski, W. J. Schaff, L. F. Eastman, R. Dimitrov, A. Mitchell, M. Stutzmann, Two dimensional electron gases induced by spontaneous and piezoelectric polarization in undoped and doped AlGaIn/GaN heterostructures. *J. Appl. Phys.* **87**, 334 (2000)
92. L. Hsu, W. Walukiewicz, Transport-to-quantum lifetime ratios in AlGaIn/GaN heterostructures. *Appl. Phys. Lett.* **80** 2508 (2002)
93. S. Keller G. Parish, P. T. Fini, S. Heikman, C. H. Chen, N. Zhang, S. P. DenBaars, U. K. Mishra, and Y. F. Wu, Metalorganic chemical vapor deposition of high mobility AlGaIn/GaN heterostructures. *J. Appl. Phys.* **86**, 5850 (1999)
94. J.M. Peransin P. Vignaud, D. Rigaud, and L. K. J. Vandamme, 1/F Noise in Modfets at Low Drain Bias. *IEEE Trans. On Elect. Dev.* **37** 2250 (1990)
95. S.T. Bradley, A.P. Young, L.J. Brillson, M.J. Murphy, W.J. Schaff, L.F. Eastman, "Influence of AlGaIn Deep Level Defects on AlGaIn/GaN 2-DEG Carrier Confinement", *IEEE Trans. Elec. Dev.* **48**, 412 (2001)
96. C. Kisielowski, "Strain in GaN Thin Films and Heterostructures", Chapt. 7 in: *Semiconductors and Semimetals* **57**, p. 275, eds.: J.I. Pankove and T.D. Moustakas, Academic Press, 1999

9. Publications

1. **Recombination Related to Two-Dimensional Electron Gas of $\text{Al}_x\text{Ga}_{1-x}\text{N}/\text{GaN}$ Single Heterostructures Studied with Picosecond Time-Resolved Photoluminescence,**
Q. Yang, R. Armitage, E.R. Weber, R. Birkhahn, D. Gotthold, S. Guo, B. Albert, MRS Symp. Proc. **798**, Y10.47 (2004)
2. **Determination of dislocation core structure to better than 0.1 Å,**
X. Xu, S.P. Beckman, P. Specht, E.R. Weber, D.C. Chrzan, R.P. Erni, I. Arslan, N. Browning, A. Bielloch, C. Kisielowski, submitted to Phys. Rev. Lett. (2004)
3. **Observation of a new hydrogenic donor in the luminescence of electron-irradiated GaN,**
Q. Yang, H. Feick, E.R. Weber, Appl. Phys. Lett. **82**, 3002 (2003)
4. **Contributions from gallium vacancies and carbon-related defects to the "yellow luminescence" in GaN,**
R. Armitage, W. Hong, Q. Yang, H. Feick, J. Gebauer, E.R. Weber, S. Hautakangas, K. Saarinen, Appl. Phys. Lett. **82**, 3457 (2003)
5. **The effect of residual lens aberrations on the determination of column positions around partial dislocations in GaAs,**
X. Xu, S.P. Beckman, P. Specht, D.C. Chrzan, E.R. Weber, C. Kisielowski, Microscopy and Microanalysis **9**, 498 (2003)
6. **Generation-recombination low-frequency noise signatures in GaAs metal-semiconductor field-effect transistors on laterally oxidized AlAs,**
S. Y. Tzeng, M. J. Cich, R. Zhao, H. Feick, and E. R. Weber, Appl. Phys. Lett. **82**, 1063 (2003)
7. **Ab initio prediction of the structure of glide set dislocation cores in GaAs,**
S.P. Beckman, X. Xu, P. Specht, E.R. Weber, C. Kisielowski, D.C. Chrzan, Journal of Physics: Condensed Matter **14**, 1 (2002)
8. **Nitrogen Incorporation in GaAsN Grown at Low Temperature by Molecular Beam Epitaxy,**
R. Zhao, J. Gebauer, P. Specht, H. Feick, E.R. Weber, in: Physik Mikrostrukturierter Halbleiter Vol. **27**, eds.: P. Specht et al., 4th Symposium on Non-Stoichiometric III-V Compounds, Asilomar, October 2002, p. 25
9. **A Standard Low Temperature GaAs Growth: Prerequisite for Defect Engineering,**
P. Specht, R. Zhao, J. Gebauer, E.R. Weber, in: Physik Mikrostrukturierter Halbleiter Vol. **27**, eds.: P. Specht et al., 4th Symposium on Non-Stoichiometric III-V Compounds, Asilomar, October 2002, p. 31
10. **Low Frequency Noise Characterization of Point Defects in Semiconductors,**
M.J. Cich, S.Y. Tzeng, E.R. Weber, in: Physik Mikrostrukturierter Halbleiter Vol. **27**, eds.: P. Specht et al., 4th Symposium on Non-Stoichiometric III-V Compounds, Asilomar, October 2002, p. 79
11. **Comparison of Proton Irradiation Effects on the Luminescence Lifetime of HVPE and MBE GaN,**
Q. Yang, H. Feick, R. Armitage, E.R. Weber, in: Physik Mikrostrukturierter Halbleiter Vol. **27**, eds.: P. Specht et al., 4th Symposium on Non-Stoichiometric III-V Compounds, Asilomar, October 2002, p. 93
12. **Influence of Carbon Doping on the Optical and Electrical Properties of MBE-GaN Grown on MOVPE-GaN / Sapphire Templates,**
R. Armitage, Q. Yang, H. Feick, S.Y. Tzeng, J. Gebauer, E.R. Weber, in: Physik Mikrostrukturierter Halbleiter Vol. **27**, eds.: P. Specht et al., 4th Symposium on Non-Stoichiometric III-V Compounds, Asilomar, October 2002, p. 119
13. **Growth and Defect Characterization of Low Temperature Molecular Beam Epitaxy GaAs,**
Ri-An Zhao, dissertation for the degree of Doctor of Philosophy in Engineering – Materials Science and Engineering in the Graduate Division of the University of California at Berkeley, 2002
14. **Direct compositional analysis of AlGaAs/GaAs heterostructures by the reciprocal space segmentation of high-resolution micrographs,**
K. Tillmann, M. Luysberg, P. Specht, and E. R. Weber, Ultramicroscopy **93**, 123 (2002)

15. **Mechanisms of interdiffusion and thermal stability upon annealing of AlAs/GaAs:Be quantum wells grown under low temperature conditions**
K. Tillmann, M. Luysberg, A. Fattah, P. Specht, and E. R. Weber, Proceedings of Royal Microscopical Society. *Microscopy of Semiconducting Materials XII*, edited by A. G. H. Cullis, J.L. (IOP Publishing, Bristol, UK, Oxford, UK, 2001), p. 101
16. **In situ diffuse reflectance spectroscopy investigation of low-temperature-grown GaAs,**
Ri-an Zhao, Michael J. Cich, Petra Specht, and Eicke R. Weber, *Appl. Phys. Lett.* **80**, 2060 (2002)
17. **Influence of gas transport on the oxidation rate of aluminum arsenide,**
M.J. Cich, R. Zhao, E.H. Anderson, E.R. Weber, *J. Appl. Phys.* **91**, 121 (2002)
18. **MESFETs fabricated on Be-doped low temperature grown GaAs buffer layers,**
T.R. Weatherford, P. Specht, A.A. Parker, E.R. Weber, in: *Physik Mikrostrukturierter Halbleiter 23*, eds.: S. Malzer, T. Marek, P. Kiesel, 3rd Symp. on Non-stoichiometric III-V Compounds, Erlangen, 2001, p. 13
19. **Low temperature MBE grown GaAs gettering of AlAs oxidation induced defects,**
M.J. Cich, R. Zhao, S. Tzeng, P. Specht, E.R. Weber, in: *Physik Mikrostrukturierter Halbleiter 23*, eds.: S. Malzer, T. Marek, P. Kiesel, 3rd Symp. on Non-stoichiometric III-V Compounds, Erlangen, 2001, p. 43
20. **Conductive non-stoichiometric III-V compounds: properties and prospective applications,**
P. Specht, M.J. Cich, R. Zhao, J. Gebauer, E.R. Weber, in: *Physik Mikrostrukturierter Halbleiter 23*, eds.: S. Malzer, T. Marek, P. Kiesel, 3rd Symp. on Non-stoichiometric III-V Compounds, Erlangen, 2001, p. 73
21. **Beryllium dopant induced stabilization against intermixing and precipitation upon annealing of LT-AlAs/GaAs:Be multiple quantum wells,**
K. Tillmann, M. Luysberg, P. Specht, M.J. Cich, E.R. Weber, in: *Physik Mikrostrukturierter Halbleiter 23*, eds.: S. Malzer, T. Marek, P. Kiesel, 3rd Symp. on Non-stoichiometric III-V Compounds, Erlangen, 2001, p. 79
22. **Does Beryllium doping suppress the formation of Ga-vacancies in non-stoichiometric GaAs layers grown at low temperatures?,**
J. Gebauer, R. Zhao, P. Specht, E.R. Weber, F. Redmann, F. Boerner, R. Krause-Rehberg, *Appl. Phys. Lett.* **79**, 4313 (2001)
23. **Incorporation and Thermal Stability of defects in highly p-conductive non-stoichiometric GaAs:Be,**
P. Specht, M.J. Cich, R. Zhao, J. Gebauer, M. Luysberg, E.R. Weber, *Physica B* **308-310**, 808 (2001)
24. **Native point defects in non-stoichiometric GaAs doped with beryllium,**
J. Gebauer, R. Zhao, P. Specht, F. Redmann, F. Boerner, R. Krause-Rehberg, E.R. Weber, *Physica B* **308-310**, 812 (2001)
25. **Defect Engineering in MBE grown GaAs-based Materials,**
P. Specht, M.J. Cich, R. Zhao, N.D. Jaeger, J. Gebauer, F. Boerner, R. Krause-Rehberg, M. Luysberg, E.R. Weber, in: 2000 Int. Semiconducting and Insulating Materials Conference, SIMC-XI, eds.: C. Jagadish, N.J. Welham, IEEE Publ. 2001, p. 73
26. **Influence of Be Doping on the Structural Properties of Low-Temperature grown GaAs,**
M. Luysberg, P. Specht, E.R. Weber, in: 2000 Int. Semiconducting and Insulating Materials Conference, SIMC-XI, eds.: C. Jagadish, N.J. Welham, IEEE Publ. 2001, p. 81
27. **Separation of Electron and Hole Dynamics in Low-Temperature grown GaAs,**
M. Haiml, U. Siegner, F. Morier-Genoud, J. Gebauer, P. Specht, E.R. Weber, U. Keller, in: 2000 Int. Semiconducting and Insulating Materials Conference, SIMC-XI, eds.: C. Jagadish, N.J. Welham, IEEE Publ. 2001, p. 97

10. Figures

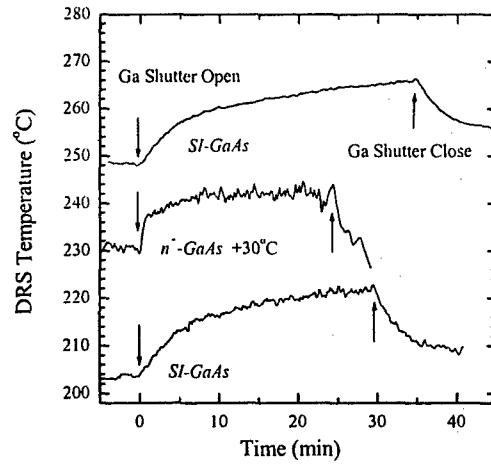


Fig. 2.1: The typical substrate temperature transients recorded by DRS during $\sim 0.5\mu\text{m}$ LT-GaAs growth. Note the n^+ GaAs temperature trace was shifted by 30°C for clarity.

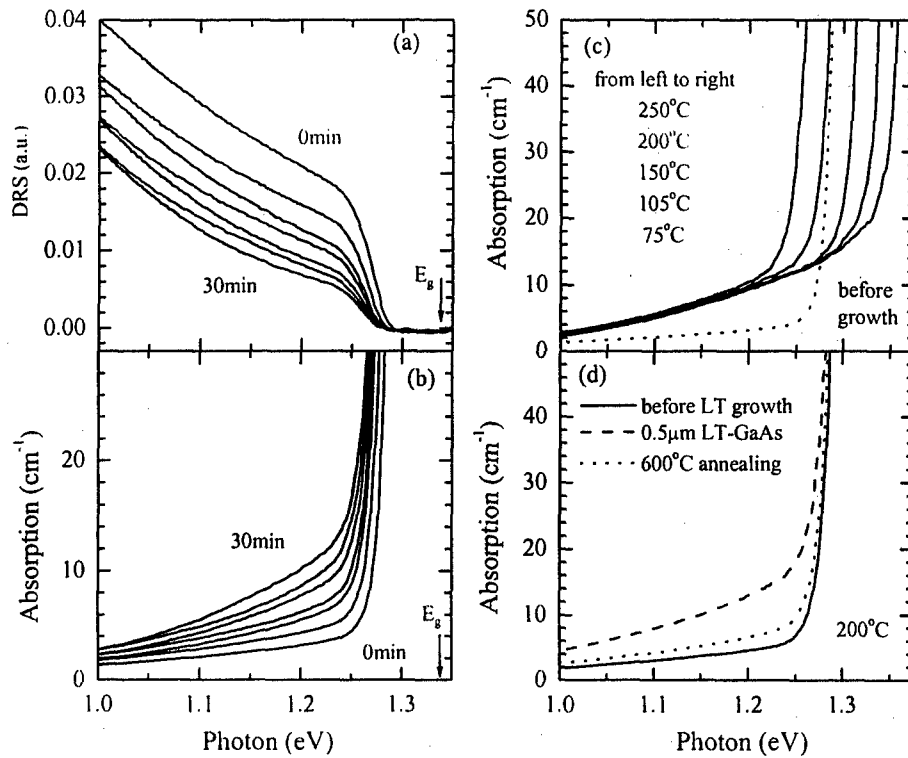


Fig. 2.2: The *in situ* DRS spectra (a) and the calculated apparent absorption spectra (b) of LT-GaAs. The spectra were measured for every 5 minutes during growth. (c) absorption at different temperature, and (d) the annealing behavior.

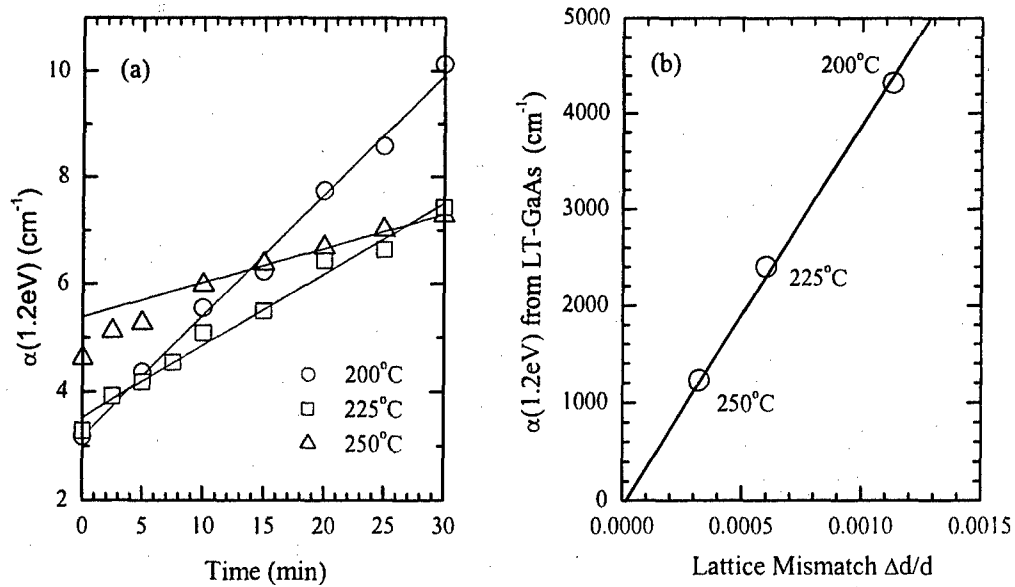


Fig. 2.3: The change of the apparent absorption at 1.2eV during growth (a), and the correlation between the extracted epilayer 1.2eV absorption and the lattice mismatch (b). The solid lines are the linear fits to the experimental data.

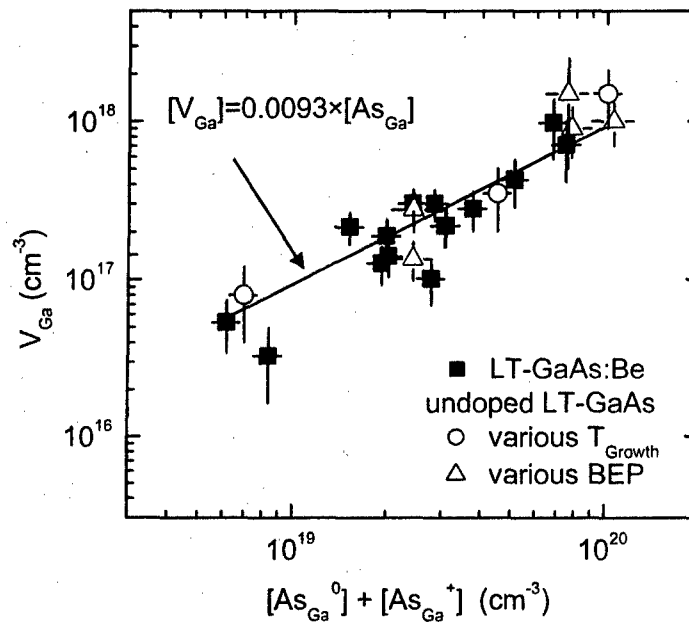


Fig 2.4: "Universal" correlation between As_{Ga} and V_{Ga} defects in LT-GaAs

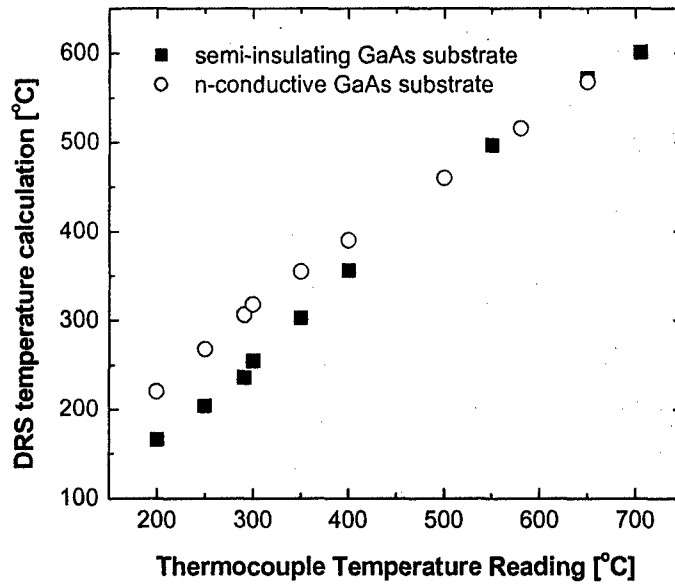


Fig.2.5: Actual DRS temperature readings for n-GaAs and SI-GaAs substrates. Note the large deviation at low growth temperatures, for the same thermocouple readings up to 80°C different DRS readings were observed.

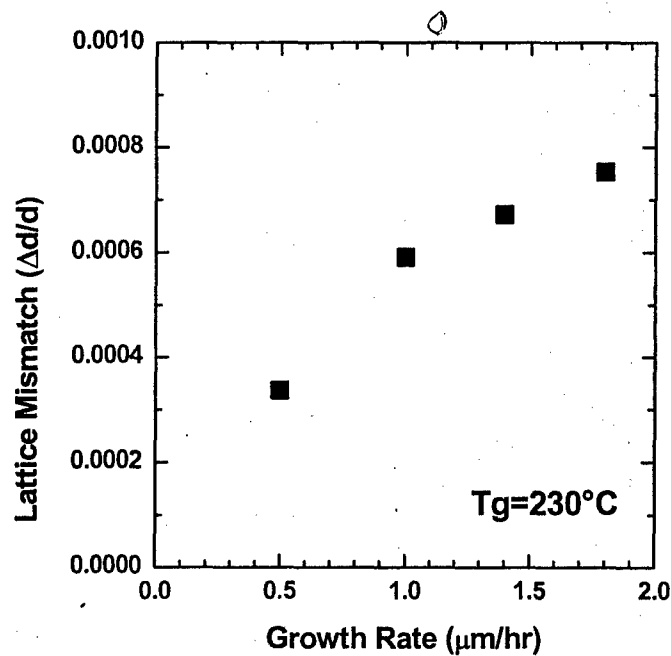


Fig.2.6: Change in As_{Ga} defect concentration (or lattice mismatch $\Delta d/d$) with different growth rates. Epilayers were grown at 230°C with BEP ratio = 20

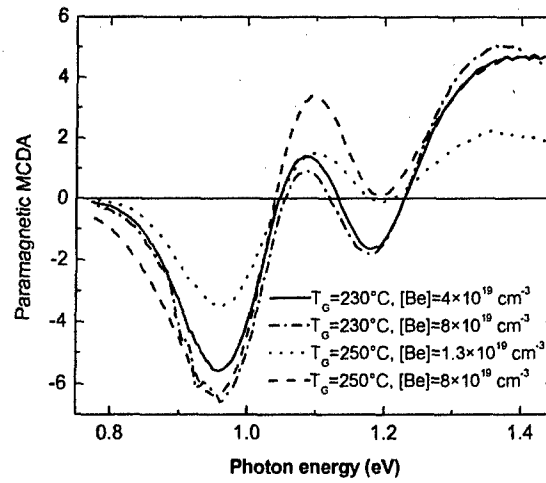


Fig. 2.7: Unknown defect in the paramagnetic part of the MCDA spectra of various LT-GaAs:Be epilayers. (BEP ratio = 20; growth rate: 1 $\mu\text{m/hr}$)

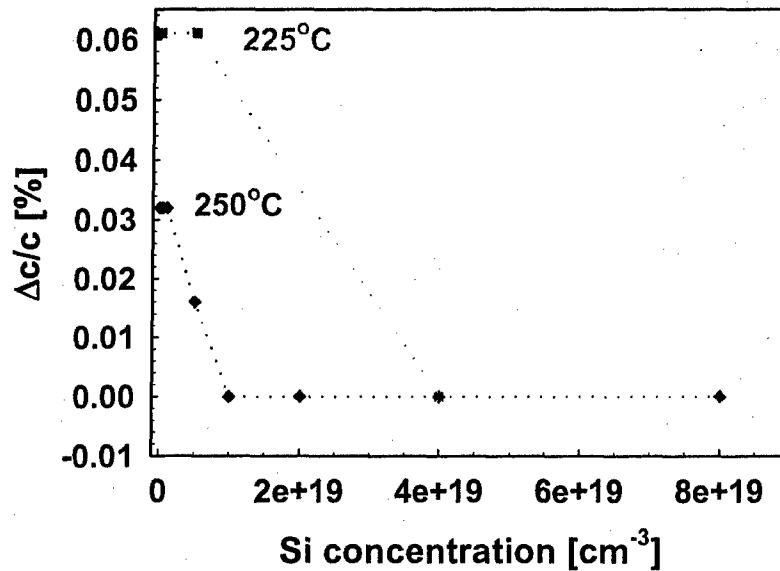


Fig. 2.8: Lattice mismatch in Si-doped LT-GaAs with increased doping concentration

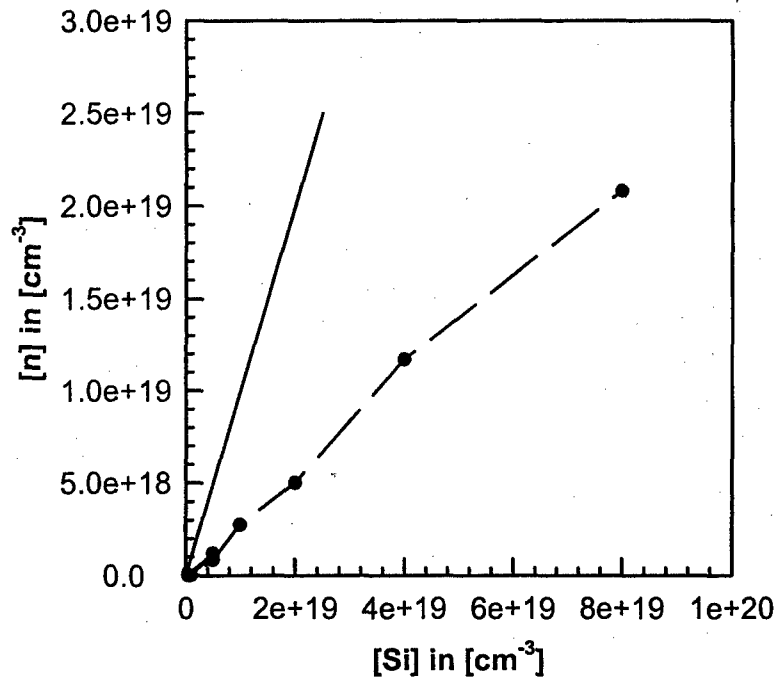


Fig. 2.9a: Free electron concentration in Si-doped LT-GaAs with doping, black line gives the uncompensated reference curve

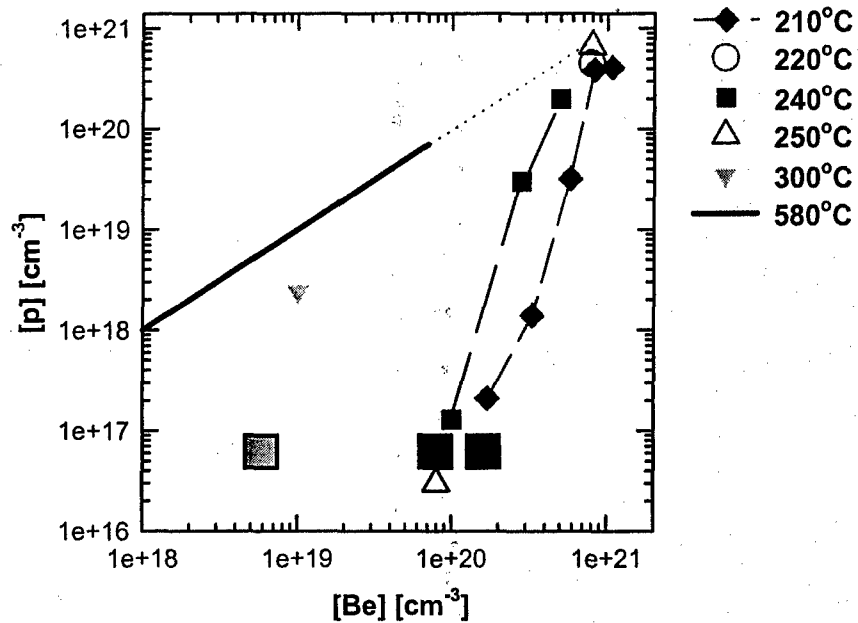


Fig. 2.9b: Free hole concentration in Be-doped LT-GaAs with doping, black framed squares give the calculated [p] using the Fermi Level position: green: 300°C, blue: 240°C, red: 210°C

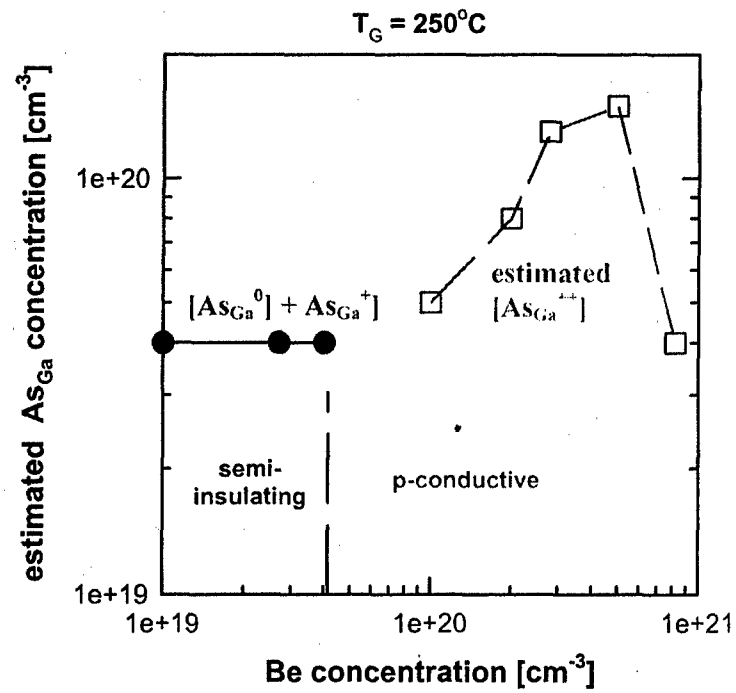


Fig. 2.10: Total arsenic antisite concentration, calculated from three different charge states, $\text{As}_{\text{Ga}}^{++}$ is estimated upper limit, see text for details

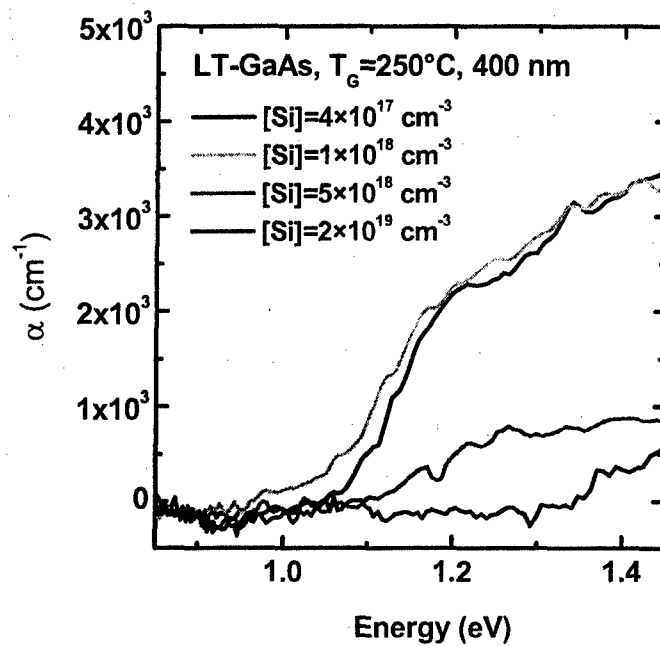


Fig. 2.11a: NIRA spectra of silicon doped LT-GaAs showing the decrease of neutral $[\text{As}_{\text{Ga}}]$

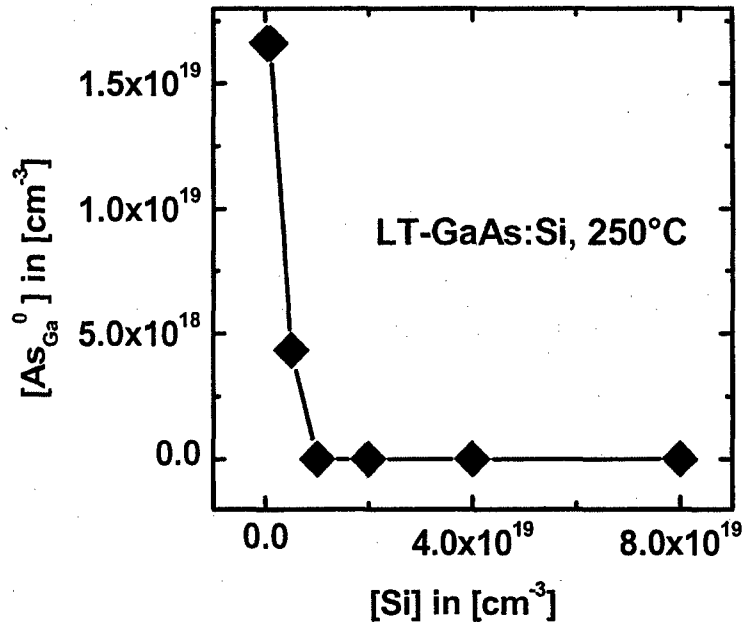


Fig. 2.11b: Calculated neutral arsenic antisite concentration dependent on silicon doping

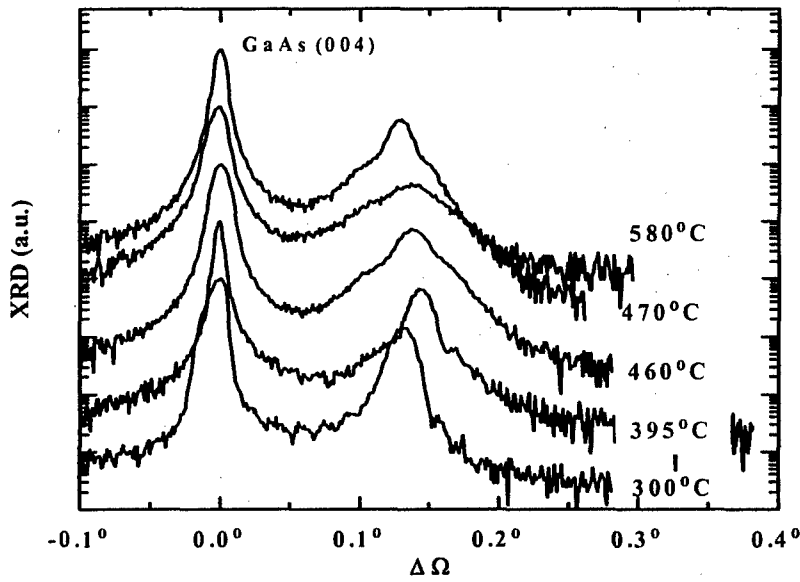


Fig 2.12: XRD rocking curves from GaAsN grown with the same N plasma conditions at different temperatures

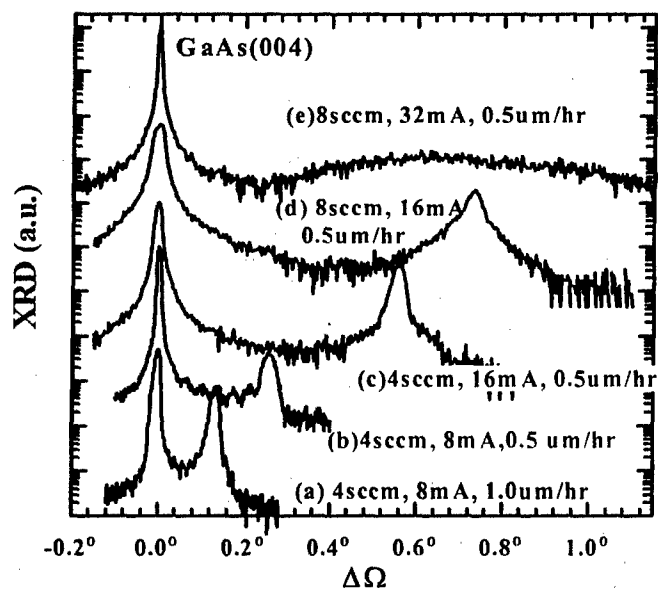


Fig 2.13: XRD for GaAsN samples grown at 300°C with gradual increase (from (a) to (e)) of the nitrogen supply from plasma discharge.

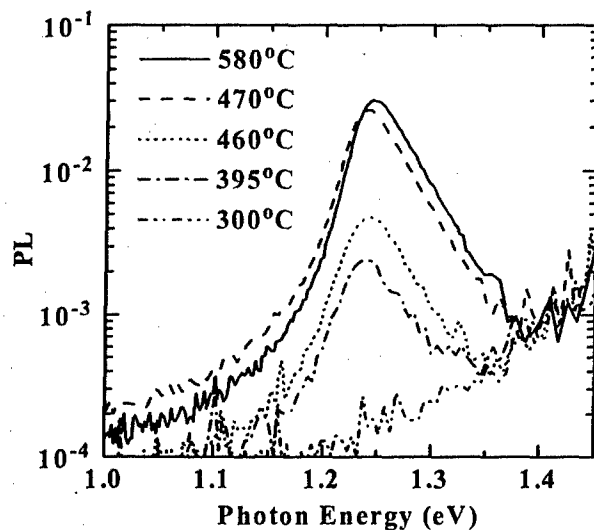


Fig 2.14: Room temperature PL for GaAsN samples grown at different temperatures.

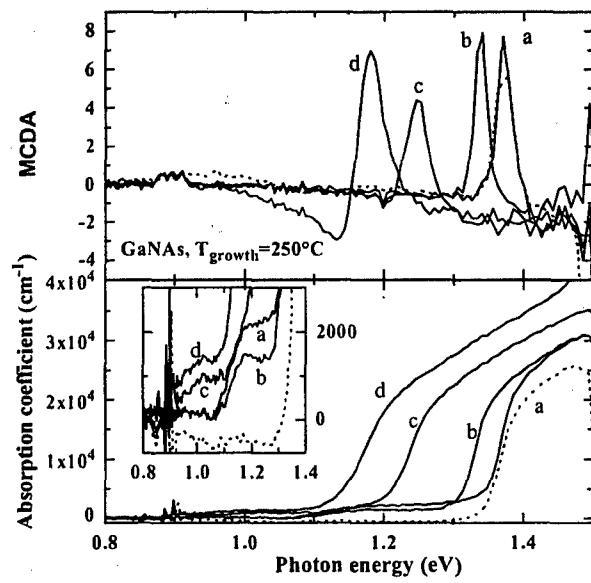


Fig. 2.15: Near infrared absorption and magnetic circular dichroism of absorption at 1.8K for samples grown at 250°C with [N] 0.6% (a), 0.9% (b), 1.5% (c) and 2.1% (d). The dotted lines are spectra measured after white light illumination. The inset shows the characteristic As_{Ga} absorption near 1.2eV.

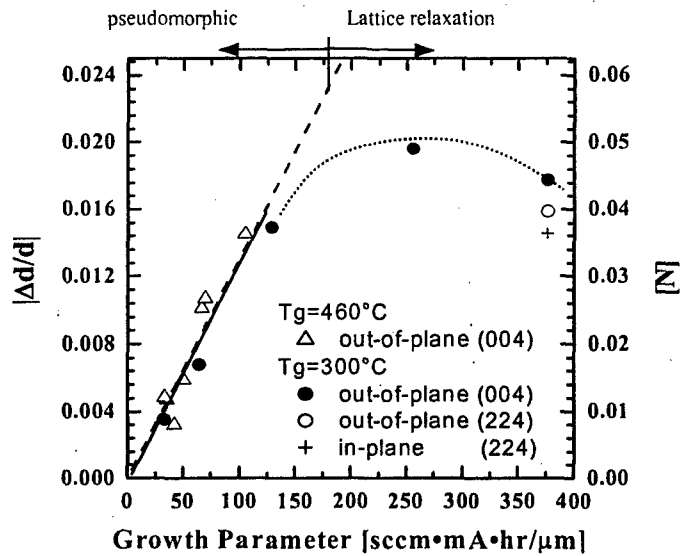


Fig. 2.16: The relationship between lattice mismatch and nitrogen incorporation at 300°C and 460°C.

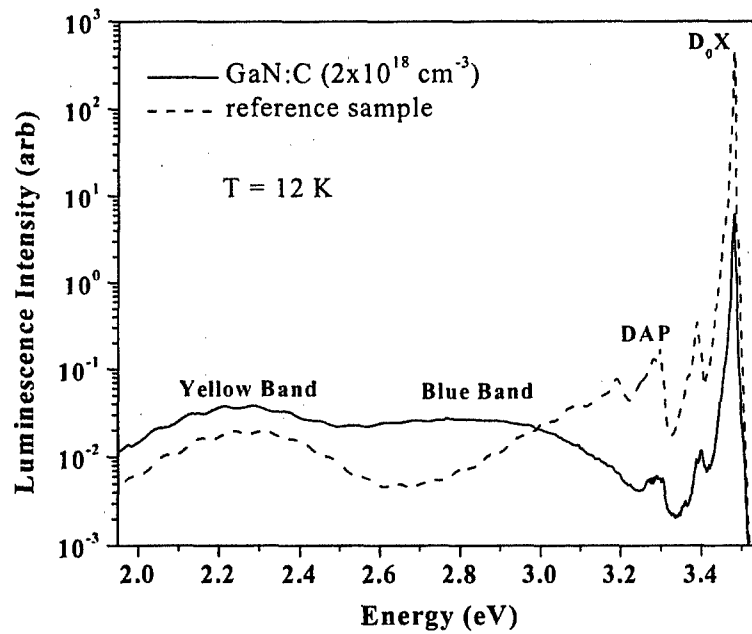


Fig. 3.1: Low-temperature PL spectra of carbon-doped and reference samples. Note that the intensities are not normalized and the same arbitrary units are used for both samples. The spectra were measured under identical conditions to ensure accurate comparison of luminescence intensities.

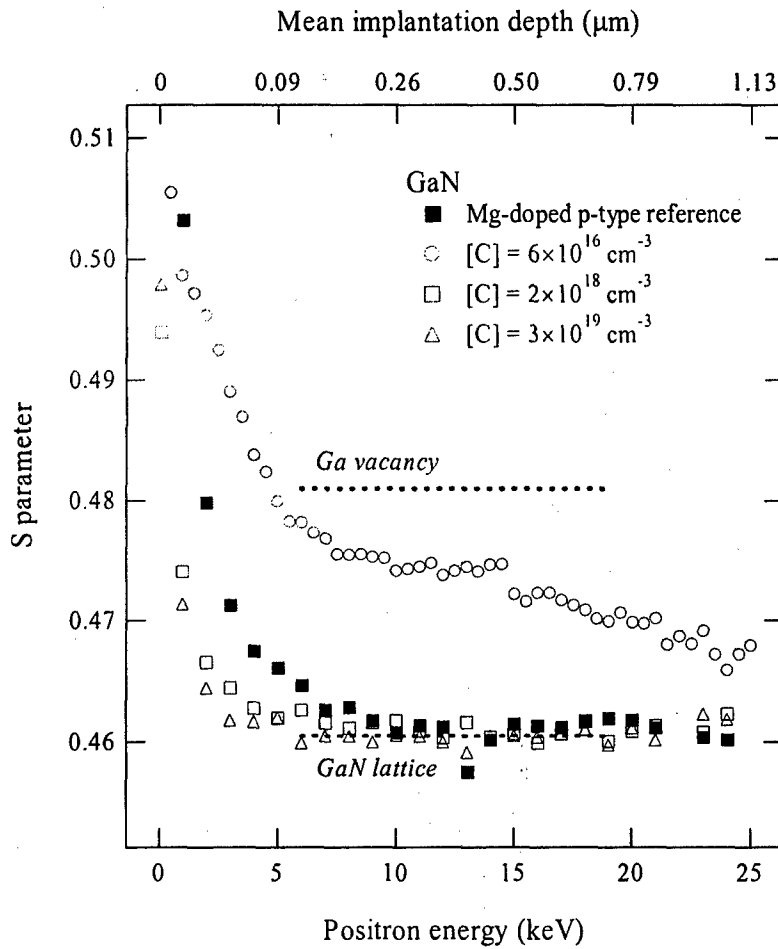


Fig. 3.2: The positron annihilation low electron momentum parameter (S) as a function of implantation energy (depth) for carbon-doped and reference films. The GaN:Mg sample is a standard of negligible vacancy concentration. The dashed lines show the S parameters in the GaN lattice and at the Ga vacancies. The top axis indicates the mean stopping depth corresponding to the positron implantation energy.

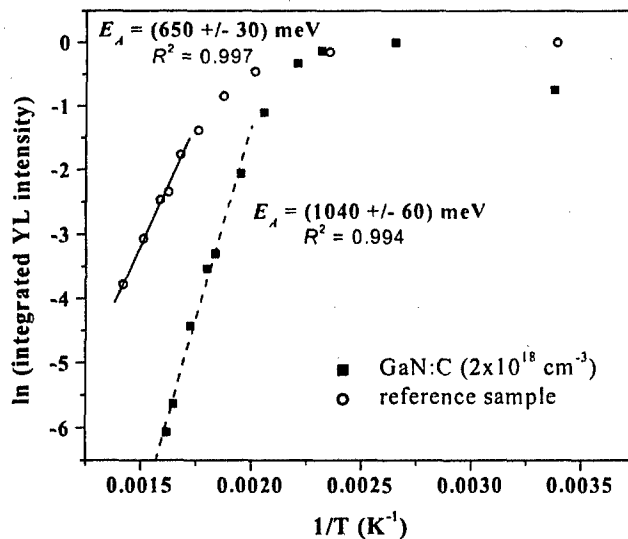


Fig. 3.3 : Arrhenius plot of the integrated intensity of the yellow luminescence band for carbon-doped GaN and a reference film. For clarity, the data here are normalized to the YL intensity at room temperature. The defect ionization energy E_A is extracted from a fit to the linear region with a regression coefficient R^2 close to unity. The modest increase in the yellow luminescence intensity for GaN:C upon initial heating is due to thermal quenching of a competing luminescence channel (the blue band).

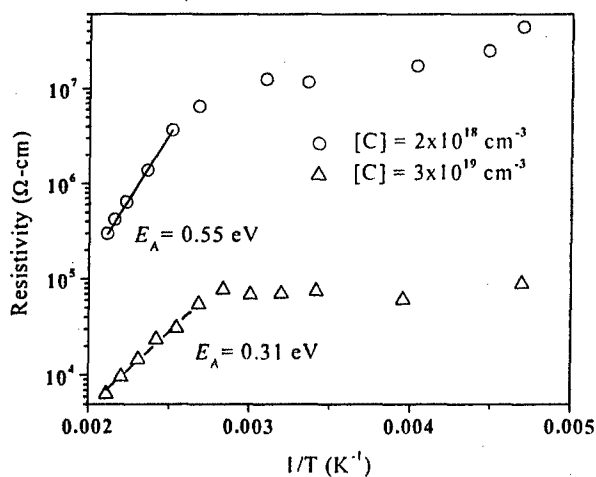


Fig. 3.4: Temperature dependence of the resistivity of GaN:C films

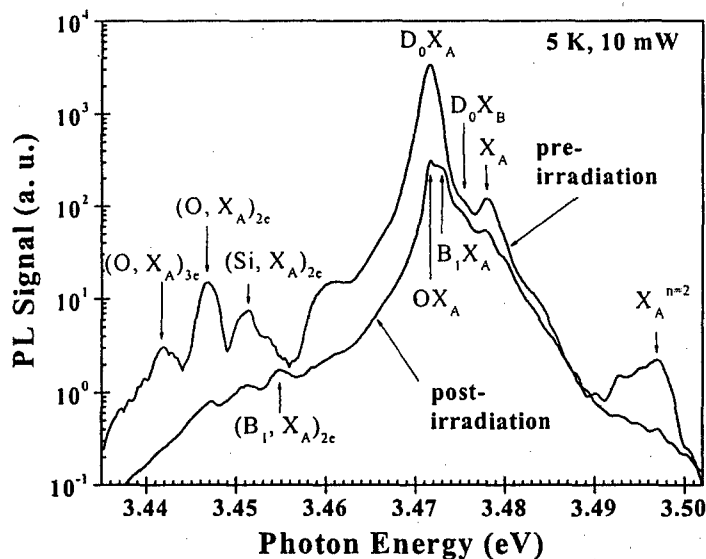


Figure 4.1: Time-integrated excitonic luminescence spectra of the 250-µm free-standing HVPE GaN before and after 0.42-MeV electron irradiation

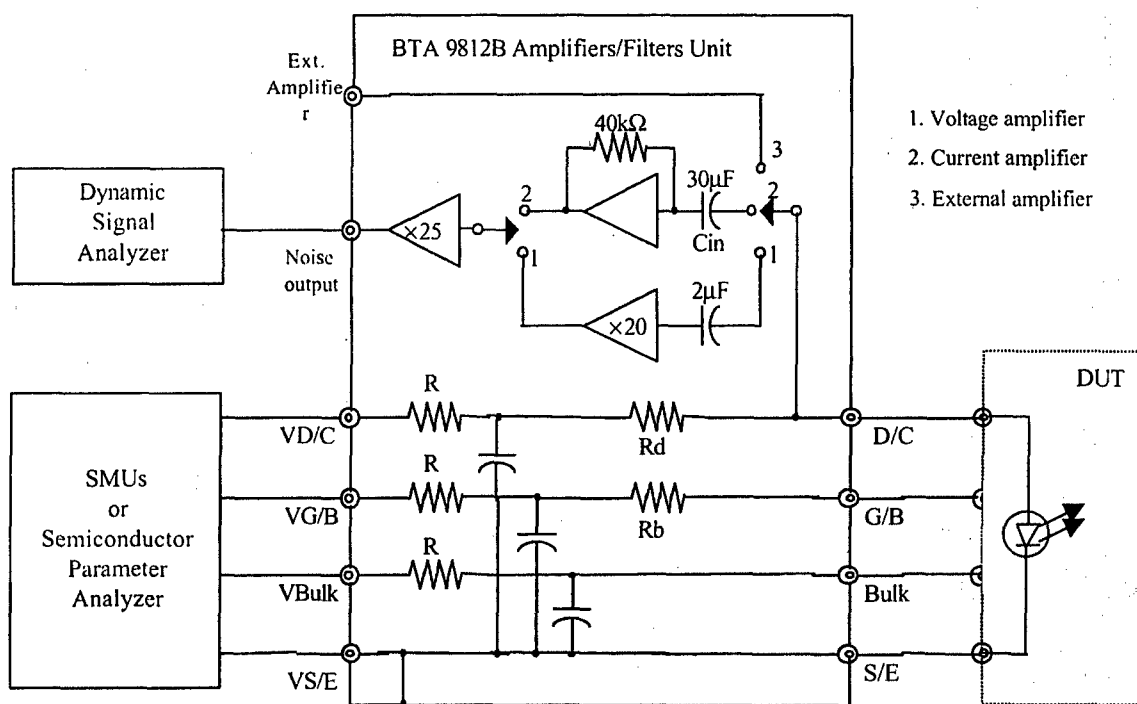


Figure 5.1. Low frequency noise measurement apparatus. The n-side of the device under test (DUT) is connected to the S/E connection, and the p-side is connected to the D/C connection. (Positive bias is applied to the D/C connection to forward bias the device).

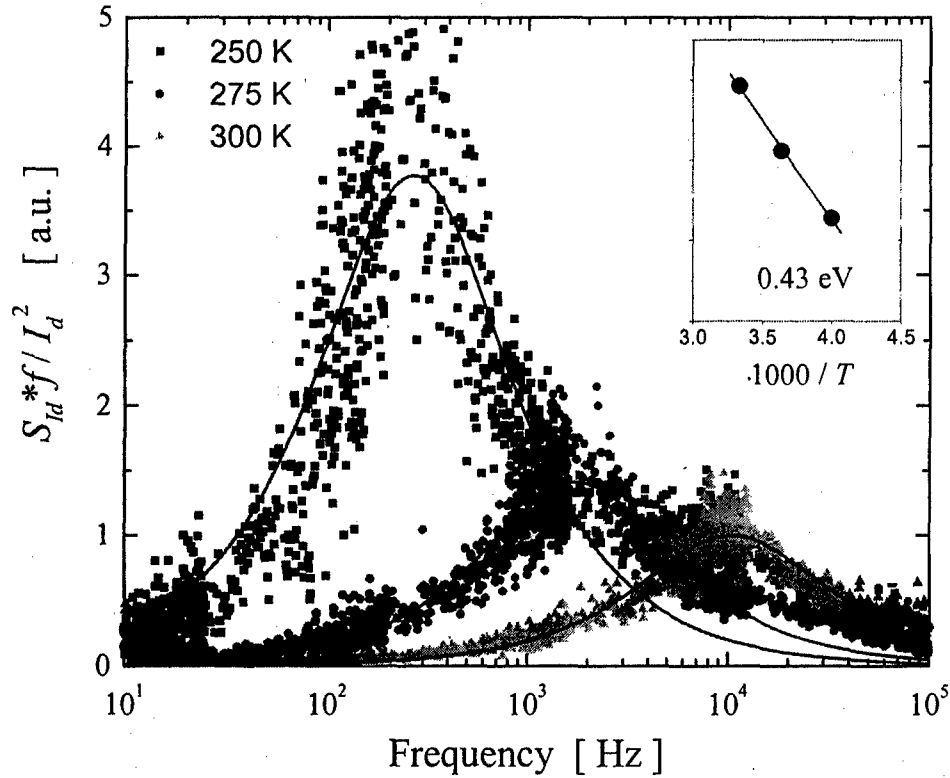


Fig. 5.2: Noise spectra of irradiated silicon diode. The ordinate is the current noise times the frequency, normalized to the dc forward current level. The lines are a Lorentzian fit to the data. Inset: Arrhenius plot of trap emission rate with an activation energy of 0.43 eV

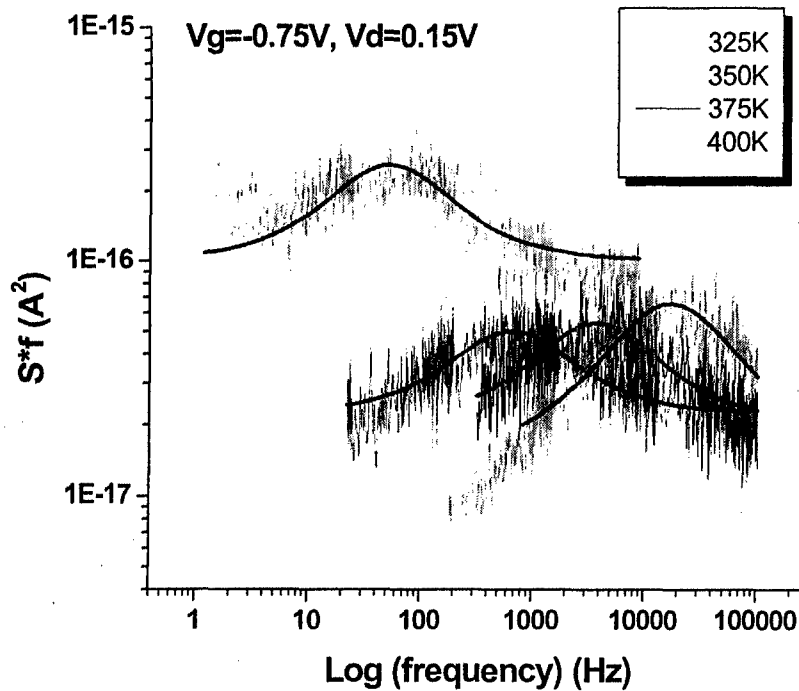


Fig. 5.3: Noise spectrum of irradiated GOI MESFET. A single well defined Lorentzian appears at each measurement temperature as shown by the best fit lines.

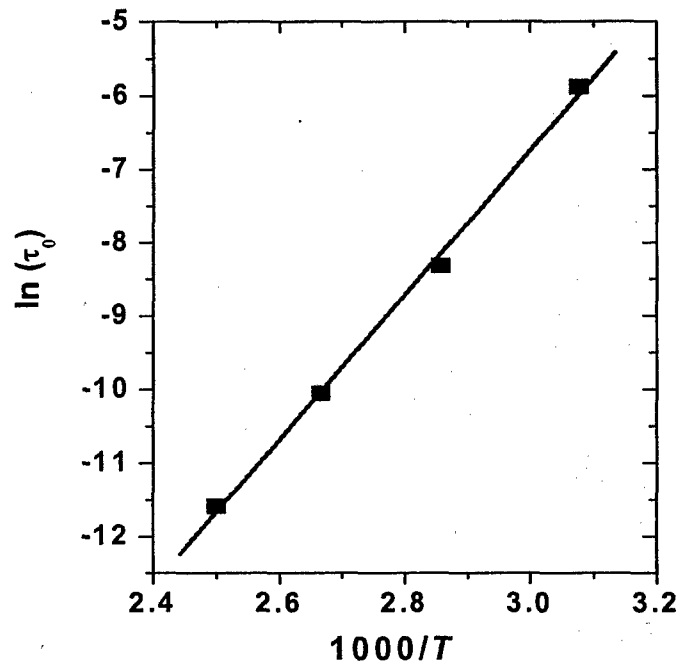


Fig. 5.4: Arrhenius plot of the inverse of the corner frequency extracted from the data in Fig. 1. The activation energy obtained is 0.79 eV.

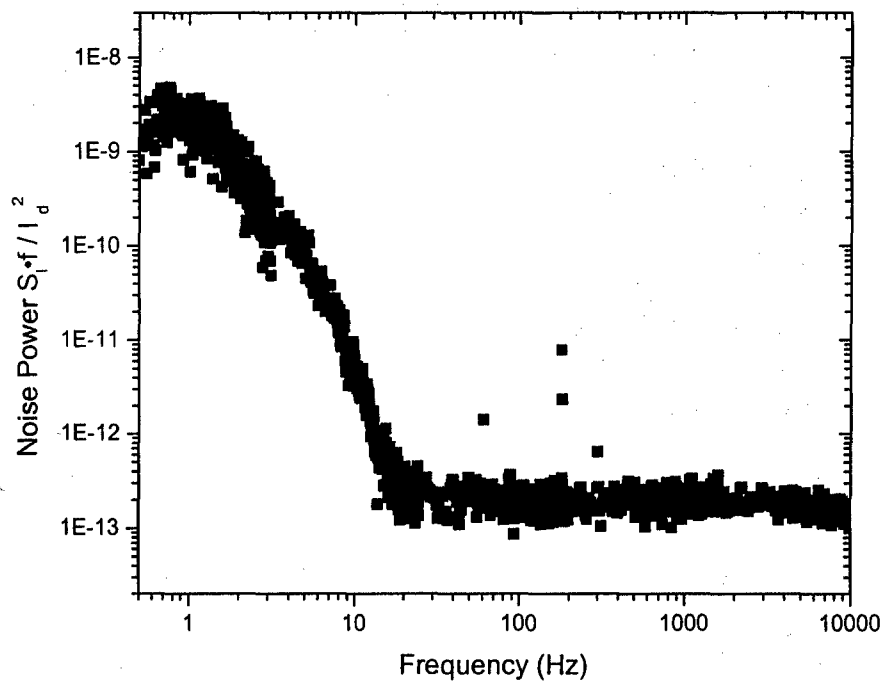


Fig. 5.5: Noise spectrum at 150 °C of LT-GaAs resistor. The bias current was 4.1 mA. The LT-GaAs was 1.5 micron thick, grown at 250 °C, and doped with $5 \cdot 10^{18} \text{ cm}^{-3}$ beryllium.

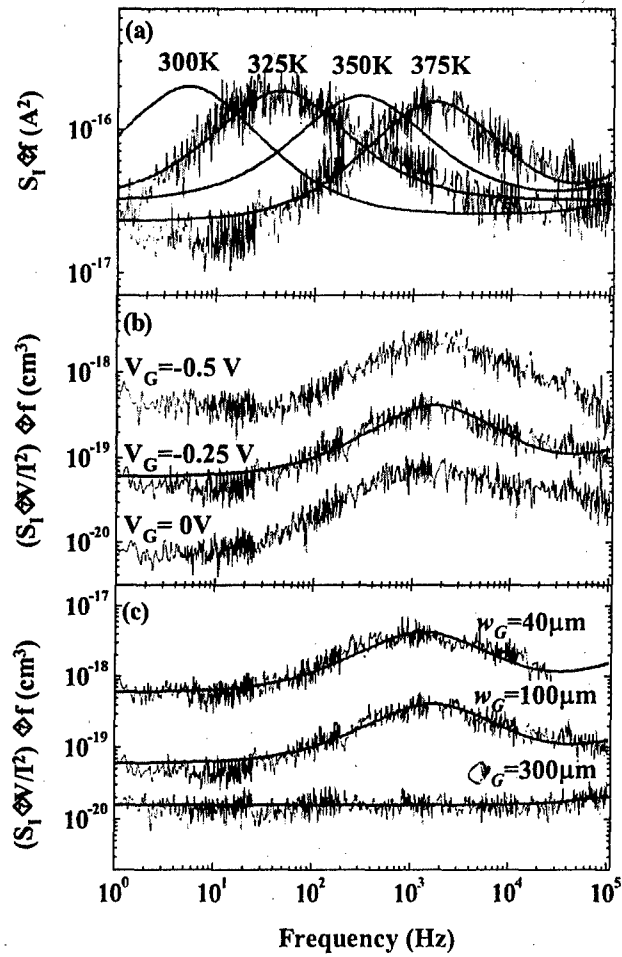


Figure 5.6: (a) Temperature dependent noise power spectra ($w_G=100\mu m$, $V_D=0.2V$, $V_G=-0.25V$); (b) normalized spectra at different gate biases ($w_G=100\mu m$, $V_D=0.2V$, $T=375K$); (c) normalized spectra for different gate widths ($V_G=-0.25V$, $V_D=0.2V$, $T=375K$)

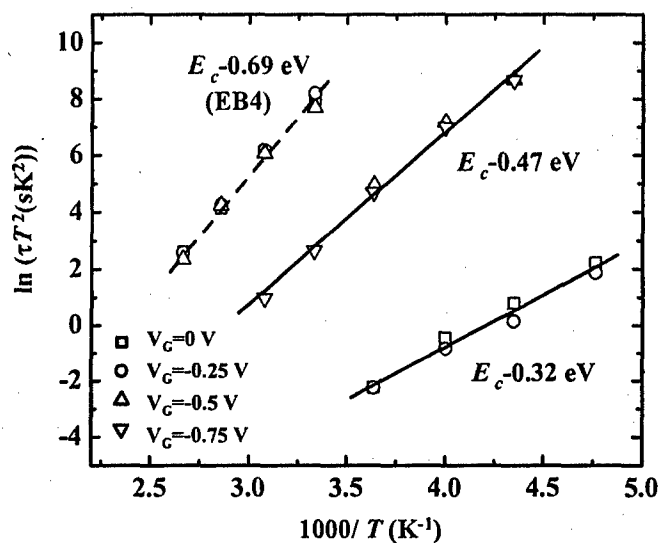


Figure 5.7: Arrhenius plot of traps in 100µm gate width GOI MESFETs at different gate biases and a drain bias of 0.2 V. Solid lines are the straight-line fits to the experimental data. The dotted line shows the published emission rate of the EB4 trap.

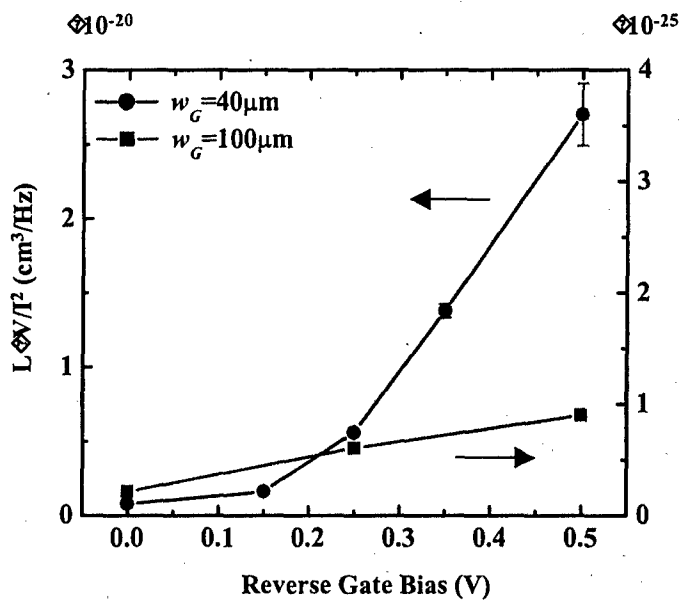


Figure 5.8: Gate bias dependence of the normalized Lorentzian noise amplitude $L\Delta V/I^2$ in GOI MESFETs with different gate widths ($T=375 \text{ K}$, $V_D= 0.2 \text{ V}$).

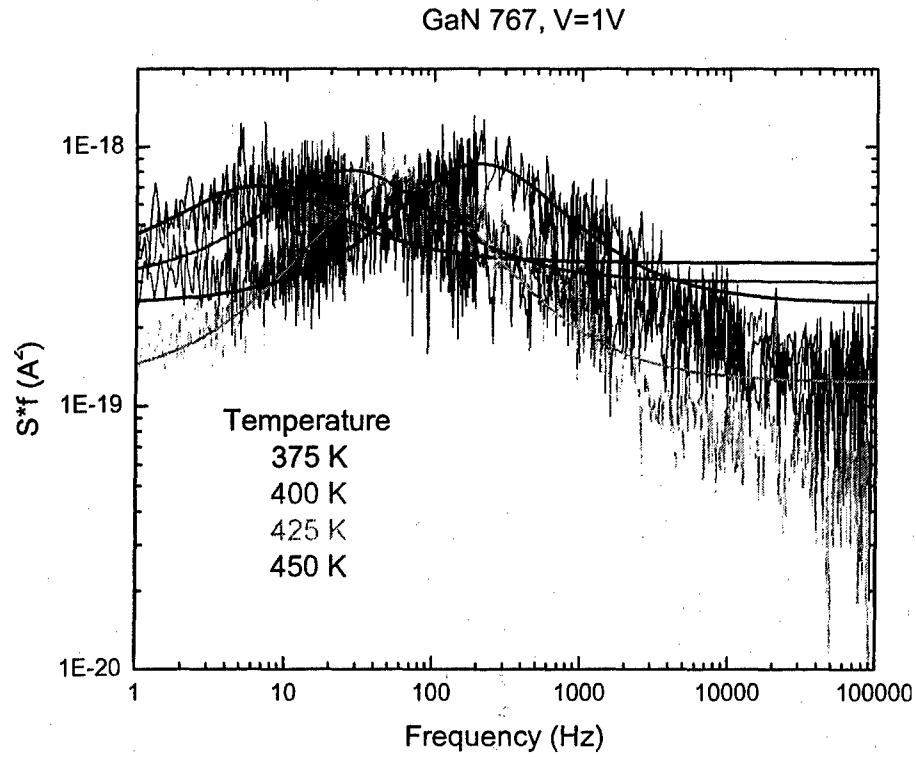


Figure 5.9: Temperature dependent noise spectroscopy of a GaN MBE grown epilayer doped with carbon and silicon

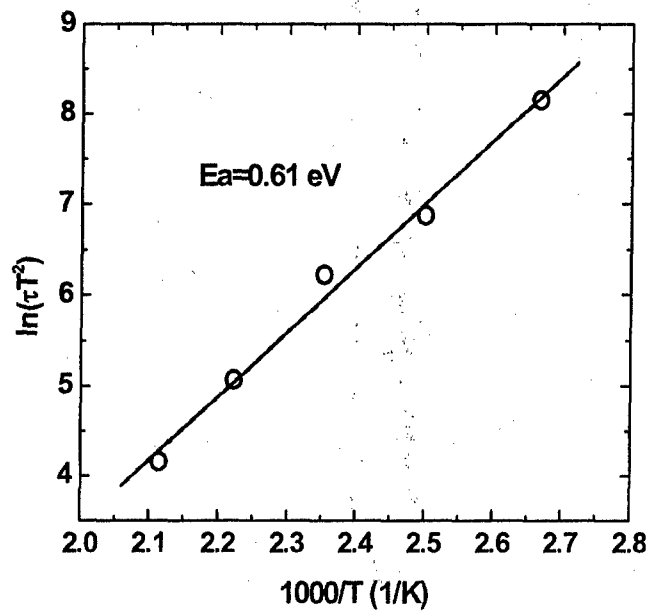


Figure 5.10: Activation energy of a generation recombination trap obtained from the peak positions of the noise spectra in Figure 5.9

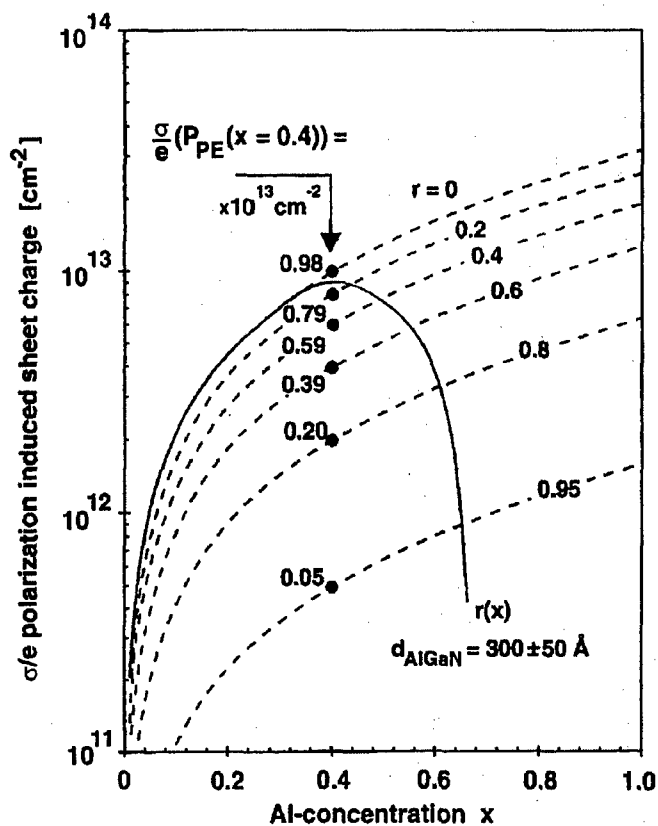


Fig. 5.11: Calculated polarization induced sheet charge for pseudomorphically grown AlGaIn/GaN heterostructures with $r=0$, and barriers with different degrees of relaxation r [2]

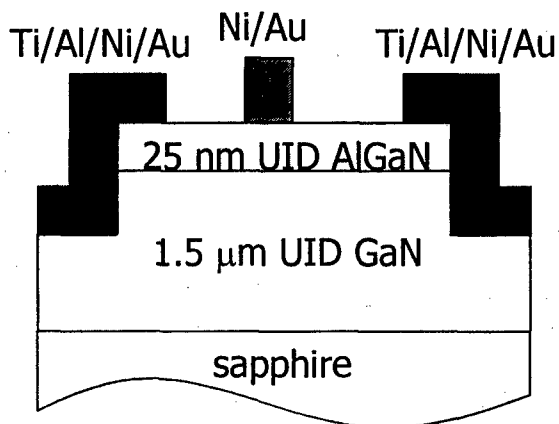


Fig. 5.12: Schematic diagram of AlGaIn/GaN HEMT structure

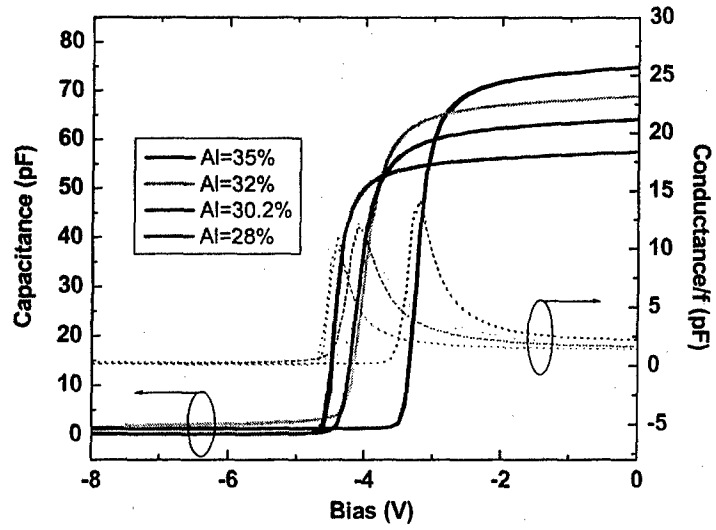


Figure 5.13: The typical C-V and G-V curves of the AlGaN/GaN HEMT structure

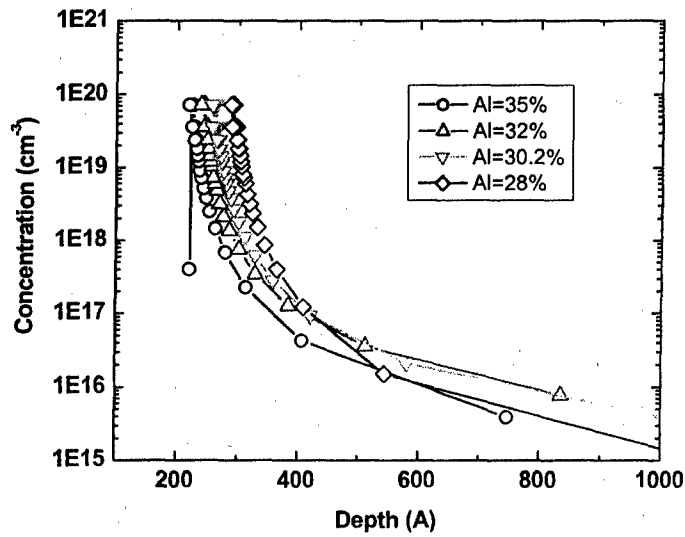


Figure 5.14: C-V profile of AlGaN/GaN HEMT with different Al composition

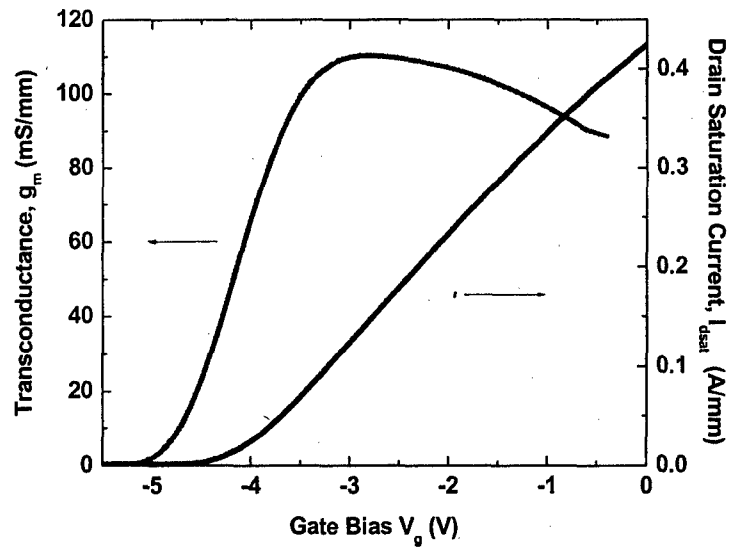


Fig. 5.15: Typical measured transfer and transconductance characteristics of $Al_{0.28}Ga_{0.72}N/GaN$ HEMT with gate length of $2 \mu m$.

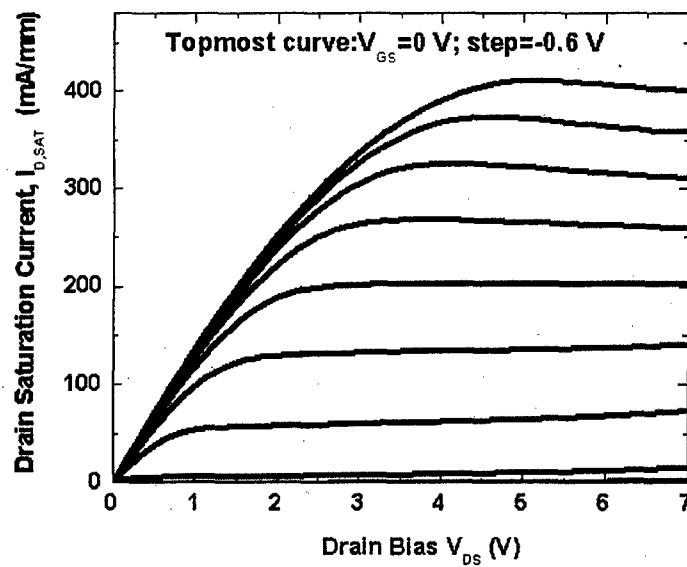


Fig. 5.16: The drain current-voltage measurement of $Al_{0.28}Ga_{0.72}N/GaN$ HEMT with gate length of $2 \mu m$

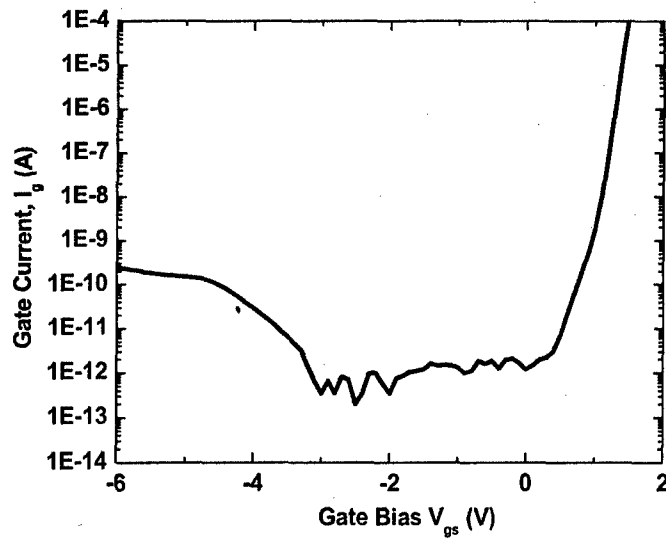


Figure 5.17: Gate leakage current of $Al_{0.28}Ga_{0.72}N/GaN$ HEMT with gate length of $2 \mu m$

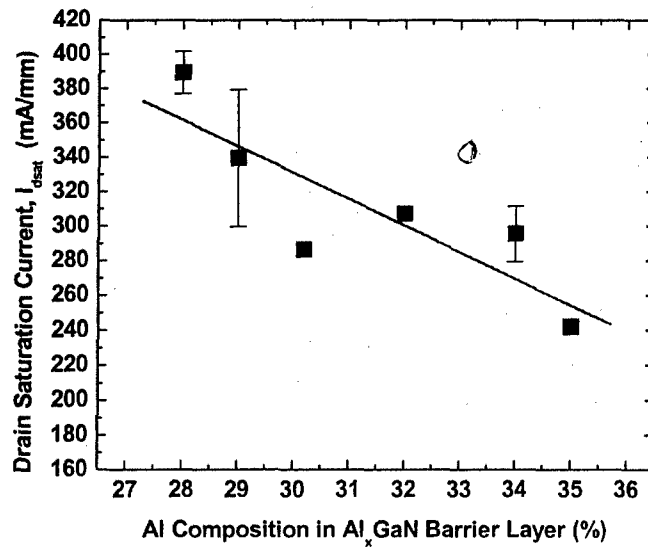


Fig.5.18: Drain saturation current as a function of $AlGaN$ barrier Al composition. All measured devices have gate length of $2 \mu m$, and gate widths of $100 \mu m$. Measurement condition: $V_d=6V$, $V_g=0V$

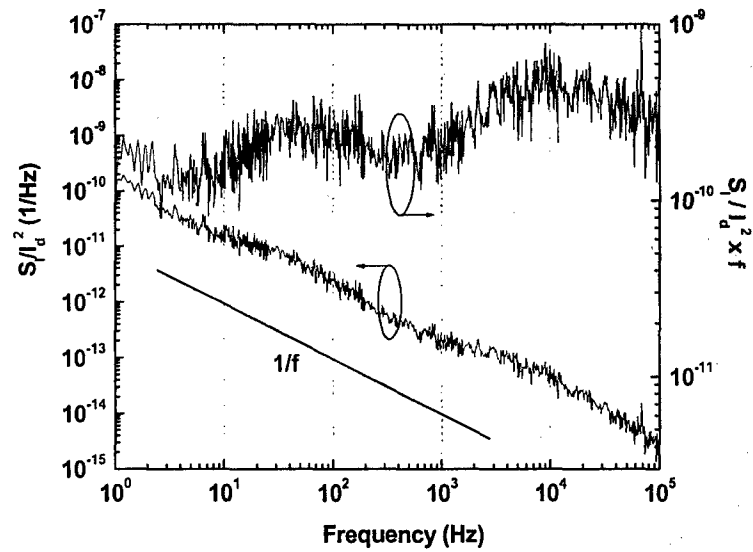


Fig. 5.19: Sample noise spectra for $Al_{0.28}Ga_{0.72}N/GaN$ HEMT with gate length of $2 \mu m$. $I_d = 3 mA$. Top curve is the relative spectral noise density multiplied by frequency and the bottom curve is the relative spectral noise density.

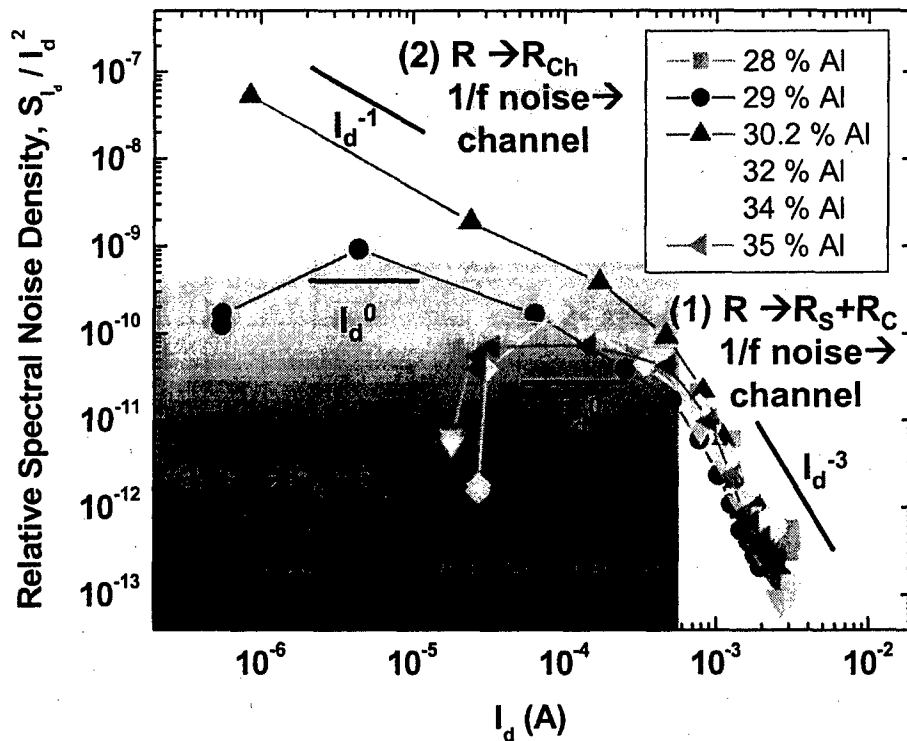


Figure 5.20: Dependencies of the relative spectral noise density of drain current fluctuations at constant low drain bias of $0.5 V$ for $AlGaN/GaN$ HEMT structures with different Al composition

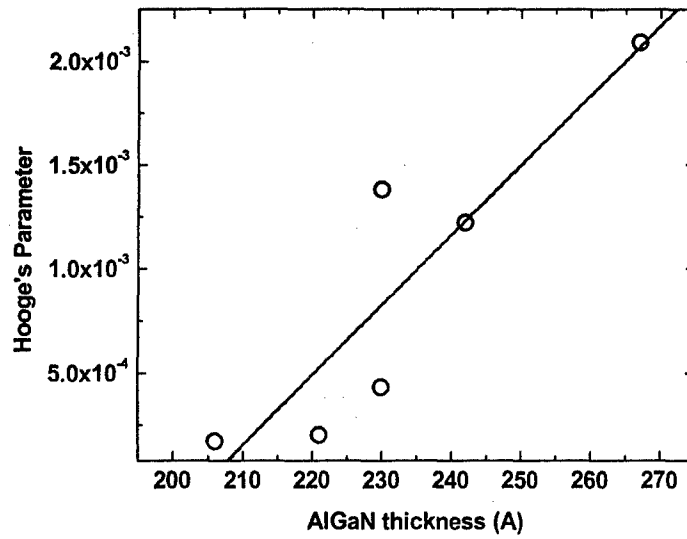


Fig. 5.21: Extracted Hooge's parameter of AlGaN/GaN HEMT structure as a function of AlGaN barrier thickness.

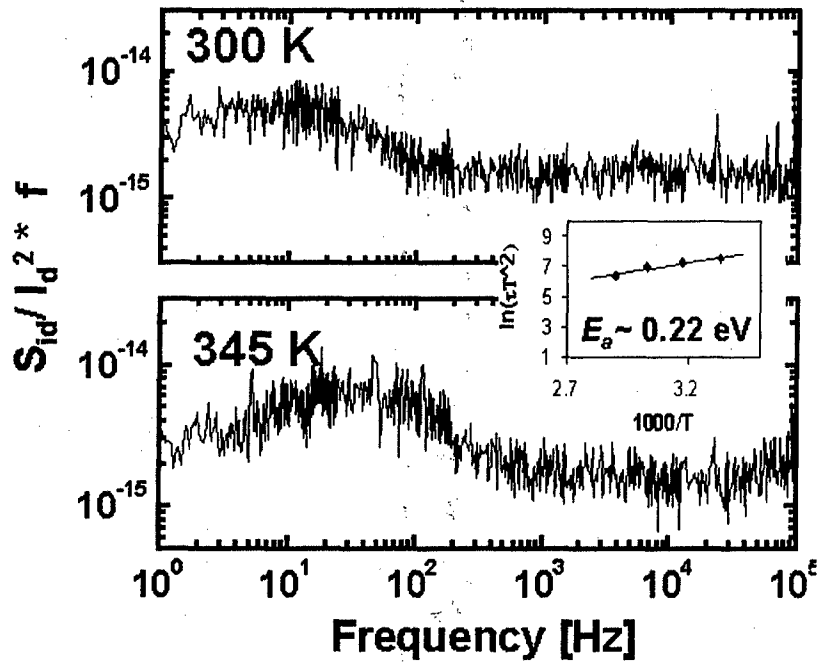


Fig. 5.22: Noise spectral density as a function of temperature and the Arrhenius plot. Shown here as an example is the data for the 29% AlGaN barrier ($V_g=1.5V$, $V_d=0.5V$, $I_d \sim 2mA$)

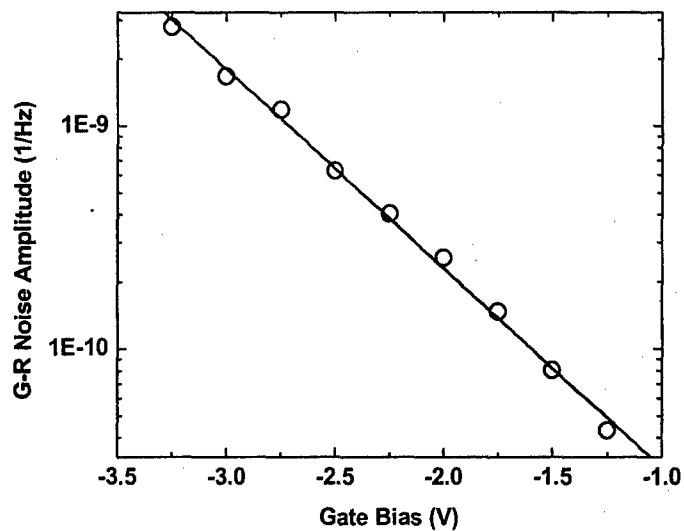


Fig. 5.23: Normalized generation-recombination noise amplitude as a function of applied gate bias, shown here are data from the 20% AlGaIn barrier ($V_d=0.5V$)